Development of a toolbox for high-precision spectroscopy of ultracold molecules

Jakub Dobosz

Thesis submitted for the degree of Doctor of Philosophy

Doctoral School of Exact and Natural Sciences

Faculty of Physics, University of Warsaw

September 2025

Supervisor: Prof. dr hab. Paweł Kowalczyk
Co-supervisor: Dr Mariusz Semczuk

Abstract

This dissertation presents the development of experimental tools enabling precision studies of ultracold atoms and molecules. It builds on the foundations of laser cooling and trapping, laser frequency stabilization, and optical frequency combs, which together define the modern landscape of precision spectroscopy and time metrology.

This work addresses several key components required for stable and scalable measurement environments: advanced laser systems with offset locking and frequency comb referencing, coherent optical frequency transfer with residual noise suppression, and precise control of magnetic fields in ultracold atom experiments.

Beyond atomic systems, the dissertation explores pathways toward ultracold molecules, motivated by their rich internal structure, strong dipolar interactions, and potential applications in many-body physics. Particular attention is given to alkali–silver dimers, such as KAg and CsAg, predicted to possess exceptionally large permanent dipole moments. As a step toward their production, the photoionization cross sections of excited states of cesium and potassium at 328 nm are measured and analyzed, providing crucial input for molecule-formation strategies.

The work integrates these advances into a coherent experimental "toolbox": fast magnetic field switching, autonomous frequency-tunable spectroscopy lasers, fiber-based optical frequency distribution with digital noise cancellation, and photoionization studies. Together, these developments establish a robust platform for next-generation precision measurements on ultracold molecules.

Streszczenie

Niniejsza rozprawa przedstawia rozwój narzędzi eksperymentalnych umożliwiających precyzyjne badania ultrazimnych atomów i cząsteczek. Opiera się ona na fundamentach chłodzenia i pułapkowania laserowego, stabilizacji częstotliwości laserów oraz grzebieni częstotliwości optycznych, które wspólnie wyznaczają współczesny krajobraz precyzyjnej spektroskopii i metrologii czasu.

Praca obejmuje kluczowe elementy potrzebne do wytworzenia stabilnego i skalowalnego środowiska pomiarowego: zaawansowane układy laserowe ze stabilizacją częstotliwości typu offset-locking i odniesieniami do grzebienia częstotliwości, koherentny transfer częstotliwości optycznych z tłumieniem szumów resztkowych oraz precyzyjną kontrolę pól magnetycznych w eksperymentach z ultrazimnymi atomami.

Wykraczając poza układy atomowe, rozprawa bada ścieżki prowadzące do tworzenia ultrazimnych cząsteczek, motywowane ich bogatą strukturą wewnętrzną, silnymi oddziaływaniami dipolowymi oraz potencjalnymi zastosowaniami w fizyce układów wielociałowych. Szczególna uwaga poświęcona jest cząsteczkom dwuatomowym, takim jak KAg i CsAg, które według przewidywań posiadają wyjątkowo duże trwałe momenty dipolowe. Jako krok w kierunku ich wytwarzania, zmierzono i przeanalizowano przekroje czynne fotojonizacji stanów wzbudzonych cezu i potasu przy długości fali 328 nm, dostarczając istotnych danych dla strategii tworzenia cząsteczek.

Praca integruje te osiągnięcia w spójną eksperymentalną „skrzynkę narzędziową": szybkie wyłączanie pól magnetycznych, autonomiczne lasery spektroskopowe o przestrajanej częstotliwości, światłowodową dystrybucję częstotliwości optycznych z cyfrową kompensacją szumów oraz badania fotojonizacji. Razem tworzą one solidną platformę dla precyzyjnych pomiarów nowej generacji w układach ultrazimnych cząsteczek.

Acknowledgments

At the beginning, I would like to express my gratitude to my family, especially my parents, who instilled in me a passion for science and always encouraged me to broaden my horizons. For all the invaluable support over the years and trust placed in me that I chose appropriate, yet my own path.

I also thank my supervisors, Prof. Paweł Kowalczyk and Dr Mariusz Semczuk for all the substantive and administrative support and the possibility to conduct research in the laboratory. In particular, I would like to thank Mariusz for including me in all of the interesting projects over the years.

This dissertation would not come to an end without the support of my friends, especially Agata and Piotrek, who were the backbone during the good and bad times. Thank you for all the moments shared, all the travels we had together, and the friendship that means a world to me.

I would also like to thank all the members of the laboratory, especially Paweł, Mateusz, Natalia and Koray. For the hours we spent in the laboratory and the good atmosphere we had. For all the sparkling conversations related to both work and life, and all the things I could learn from you. I also thank Paulina, "the girl from the lab next door", who was my main supporter of tea. It was always delicious.

I thank the heads of the Division of Optics, Prof. Radzewicz and Prof. Fita, for all of the support both organizational and scientific. Ms. Halina for help with the administrative labyrinth of the university and for all the interesting talks about ancient Egypt. The technical staff, Mr. Marek, Mr. Andrzej, and Mr. Sławek, for every piece of equipment bought, manufactured, and repaired.

I also thank Ms. Gosia for the kind and hearty approach every time I made mistakes in the invoices. I thank the administrative director, Ms. Beata and the dean's office staff, Ms. Gosia and Ms. Iwona for the invaluable support during my whole studies, securing my job position, and their cheerful and humorous attitude.

Finally, I would like to thank Kuba, a relatively new person in my life, no less important. I hope our journey will be a long one.

Contents

Chapter 1

Introduction

New directions in science are launched by new tools much more often than by new concepts.

Freeman Dyson, Imagined Worlds (1997)

The modern era of precision spectroscopy emerged from two intertwined breakthroughs: laser cooling and trapping and robust laser frequency stabilization. Following the theoretical proposals and early demonstrations of sub-Doppler mechanisms, such as polarization-gradient cooling or Sisyphus cooling, neutral atoms could be prepared at temperatures far below the Doppler limit, enabling interrogation times and coherence previously beyond reach [1, 2, 3]. These techniques, refined through the 1980s and 1990s, set the stage for optical clocks and precision tests that define the field today [4].

In parallel, a revolution arrived with femtosecond optical frequency combs [5, 6], which created a coherent bridge between radio and optical frequencies. By making absolute optical frequencies countable and phase-coherently relatable to microwave references, in particular time standards based on cesium fountain clocks, combs transformed spectroscopy, clock technology, and time-frequency distribution. Locking lasers tightly to stable optical references became the workhorse that converted narrow transitions into metrology [7]. The relative accuracy reached in ultracold systems in terms of time metrology is the highest among any observables humankind can measure [8, 9]. For this reason, the only unit in the SI system still defined by a reference to a physical medium, not to a constant, is the second.

The development of fiber technology provided means to transfer phase-coherent optical carriers across the laboratory and beyond. That concept has scaled from intra-building links to metropolitan, national and even international networks span-

ning hundreds of kilometers with stabilities down to the 10^{-19} level [10, 11], allowing comparisons of remote clocks and precision spectroscopy between facilities. The canonical approach employs a double-pass, AOM-based interferometer for active fiber noise cancellation, first shown to yield millihertz-accurate suppression of fiber-induced phase fluctuations [12].

While absolute references are one pillar, many day-to-day experiments require networks of mutually coherent lasers with tunable offsets and agile control. Here, offset-frequency locking and optical phase-locked loops are the techniques that allowed connections between primary references, combs, and many working lasers in a single experiment [13, 14]. Modern engineering now provides sub-Hz residual phase noise systems, with both analog and digital loop realizations. These techniques matter for bridging disparate wavelengths and preserving coherence through complex optical paths.

The development of technologies that enabled spectacular progress in the field of atomic, molecular and optical physics (AMO) inevitably led to a natural extension from atoms to molecules. They are particularly interesting for their richer internal structure (rotation, vibration, multiple electronic states), strong dipolar interactions, and the ability to "stitch together" transitions across the microwave, infrared, and optical domains. In recent years both preparation pathways have matured: association of atom pairs and direct laser cooling with optical cycling (including in more complex species) [15, 16]. For metrology and correlated-phase physics, ground-state samples with a control over transverse motional degrees of freedom and large permanent dipole moments are key; a recent example is a gas of dipolar NaCs molecules prepared in the absolute rovibronic ground state via stimulated Raman adiabatic passage (STIRAP) at temperatures around 300 nK [17]. The determination of molecular constants and dipole moments in heteronuclear dimers such as RbCs has also become routine [18].

Recently, an attractive line for new proposals became silver-containing heteronuclear molecules (alkali–Ag). Ab initio calculations predict exceptionally large permanent dipole moments, of the order of ten Debye for species such as CsAg, and well-bound ground states across the alkali–Ag family, making them candidates for studies of dipolar many-body physics [19]. Realistic production routes include magnetoassociation with Feshbach resonances followed by STIRAP, strategies extensively validated in alkali and mixed systems [20, 21].

All of these threads, stable references, flexible offset-locking, coherent optical carrier distribution, colder, denser samples, and exploration of ultracold molecules converge on a practical quote: precision progress is often launched by better tools. In that spirit, this dissertation concludes a six-year period of development of a coherent

"toolbox" for the exploration of fundamental physics with ultracold molecules.

Structure of the dissertation

- **Chapter 2. Laser cooling and trapping** - this chapter is a general overview of the methods of cooling and trapping of neutral atoms, developed over the years by the scientific community and implemented in our experiment. It follows a pattern of a typical experimental sequence interlaced with historical background. We describe Doppler cooling and its application in magneto-optical trap, then sub-Doppler cooling methods, and finally trapping in an optical dipole trap. Each of these steps is a starting point for other topics discussed later in the dissertation.

- **Chapter 3. K-Cs apparatus at the University of Warsaw** - in this chapter I present selected features of the experimental setup. I especially emphasize the functionalities that I was responsible for implementing. I describe the sub-millisecond off-switch of magnetic fields, offset-locking of lasers with frequency difference of around 9 GHz, and fluorescence detection setup. I also present an extensive study of loading rate enhancement by light-induced atomic desorption and a bi-directional current source for precise control of the magnetic field generated by the compensation coils.

- **Chapter 4. Laser system for precision spectroscopy** - here, I focus on the laser system consisting of a Ti:Sapphire continuous wave laser referenced to an optical frequency comb. I also describe a diffraction grating-based setup which allows for broad tunability of the laser frequency. The system relies on a server-based architecture, which enables autonomous operation and automatic tuning of the laser frequency, which makes it a unique tool for precise spectroscopy.

- **Chapter 5. Noise suppression in long-distance optical frequency transfer** - this chapter discusses long-haul transfer of an optical carrier based on an optical atomic clock reference. I focus mainly on the residual noise suppression in a remote location, which allows the retrieval of carrier quality at the local terminal. I present my contribution to the system which was the design and prototyping of a digital servo that corrects the remote laser frequency based on the beatnote with a transferred optical carrier.

- **Chapter 6. Photoionization of excited states of cesium and potassium** - in this final chapter I present the recent results on the photoionization cross

section measurements of the excited states of cesium and potassium by laser light with wavelength of 328 nm. This research forms the basis of a new project concerning the formation of highly polar KAg and CsAg molecules. I discuss a photoionization phenomenon, together with simulation based on optical Bloch equations and present the experimental values of the cross sections obtained from my measurements.

The topics described above are unified by a common aim: to provide a stable, metrologically coherent, and scalable measurement environment in which the internal structure of molecules can be probed with the highest possible resolution. Each module addresses a different experimental bottleneck, such as magnetic field control, frequency referencing, and coherent optical signal distribution. The photoionization exploration provides valuable information for the strategy of our newest planned experiment that will focus on the creation of the ground state molecules of KAg and CsAg. Together, they form an integrated platform for next-generation measurements on ultracold molecules.

Chapter 2

Laser cooling and trapping

The field of ultracold atomic, molecular, and optical (AMO) physics has been essential for the development of modern concepts in physics, in particular quantum mechanics. Since the first proposals were made in the seventies for cooling atoms using light, the introduced methods, discovered phenomena, and progress in technology led to such great accomplishments as Bose-Einstein condensation [22, 23], quantum simulators [24], construction of optical atomic clocks [25, 26], or the first quantum computers [27, 28]. This would not be possible without the work of many researchers, some of whom were awarded the Nobel Prize in Physics. In this introductory chapter, I pay tribute to those pioneers of the field and discuss the foundations of the ultracold experiments, the cooling methods, and traps.

The chapter is organized in correspondence with the typical stages of an experimental sequence. I will start with a description of Doppler or velocity-selective cooling. Then I will discuss the initial stage of every experiment, the magneto-optical trap. In addition to the basic idea and working principle of the MOT, I will also discuss its dynamics. Then I will move on to sub-Doppler cooling methods and finally describe the principle of operation of the optical dipole trap.

2.1 Doppler cooling in a 2-level system

The idea of cooling neutral atoms by light pressure was proposed in 1975 by Theodor Hänsch and Arthur Shawlow [29], later Nobel Prize laureates (although not for this particular topic). It is based on light scattering, as the authors stated: "Translational kinetic energy can be transferred from the gas to the scattered light, until the atomic velocity is reduced by the ratio of the Doppler width to the natural line width". The realization of a three-dimensional case was achieved by cooling sodium atoms to

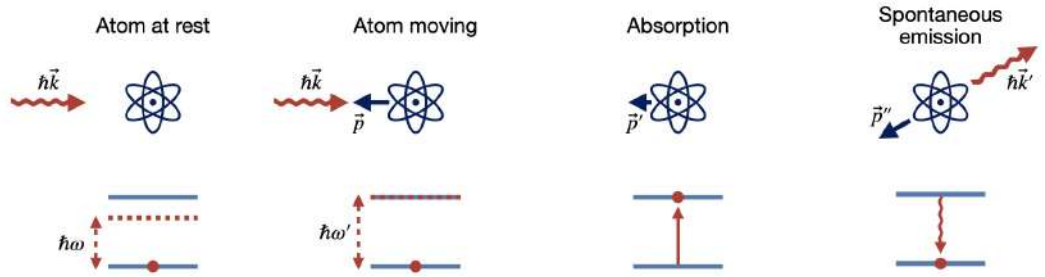

Figure 2.1: Graphical illustrations of the velocity-selective cooling. The top row shows the atom-photon interaction as seen in the laboratory frame of reference. The bottom row shows the internal structure of energy levels of an atom in the atomic frame of reference. Each step is described in detail in the main text.

approximately 240 μK, reported in 1985 in a paper by Steven Chu et al. [30]. The first author was also awarded a Nobel Prize for his extensive contribution to the field of laser cooling [31]. These works laid the foundation for a new branch of atomic, molecular, and optical physics (AMO).

In ultracold atomic physics, temperature is understood rather as a measure of the mean velocity of the atoms than in the thermodynamic sense, since the atomic samples are rarely in thermal equilibrium. In this picture, the cooling process aims to lower the velocity of the atoms. A plethora of methods has been developed over the years, the most standard one being velocity-selective or Doppler cooling.

The velocity-selective cooling is based on three fundamental laws of nature: conservation of momentum, conservation of energy, and the Lorentz transformation. The first two provide the cooling mechanism, while the last one corresponds to the velocity selection. Graphical illustrations of the processes described in this section are shown in Fig. 2.1. The symbols in the figure correspond to the symbols introduced in the discussion below.

Let us assume that we have a system that consists of an atom at rest and a photon. The atom has an internal structure composed of two levels $|g\rangle$ with energy 0 and $|e\rangle$ with energy $\hbar\omega_0$. The photon carries momentum $\hbar\vec{k}$ and has energy $\hbar\omega$, which is lower than $\hbar\omega_0$ - it is red-detuned.

We must introduce the detuning since in a thermal gas at equilibrium atoms are rarely at rest, rather they are moving according to a Maxwellian velocity distribution [32]. When transformed from laboratory to atomic frame of reference, the light frequency changes due to the relativistic Doppler effect arising from the Lorentz transformation. We shall assume that the atom has momentum $\vec{p}$ and is moving toward the incoming photon. In such a scheme, in the atomic frame of reference,

the photon will have a higher energy $\hbar\omega'$. For a certain velocity, the Doppler shift compensates the introduced red detuning, which increases the probability of photon absorption as it fulfills the conservation of energy. This shows how the Doppler effect is responsible for the velocity selection.

When the photon frequency is resonant with the atomic transition, it is absorbed, which changes the internal state of the atom from $|g\rangle$ to $|e\rangle$. At the same time, due to the conservation of momentum, the atom decreases its velocity according to formula $\vec{p}' = \vec{p} - \hbar\vec{k}$.

The excited state of the atom is not stable and, after a short time ($\approx$ 20 ns for alkalis), the atom returns to its ground state by spontaneous emission of a photon. This process is isotropic and also is subject to the conservation of momentum. The emitted photon carries momentum $\hbar\vec{k}'$ and the final momentum of the atom is equal to $\vec{p}'' = \vec{p}' - \hbar\vec{k}'$.

At first sight, there is no cooling involved since the initial and final steps of the described evolution differ only in atom and photon directions of motion. However, this directional behavior is the *spiritus movens* of the cooling process. If such a scheme is repeated many times, the momentum kicks from the red detuned laser accumulate since they are always coming from the same direction. On the other hand, the spontaneous emission is isotropic, thus the net momentum gain is equal to 0. Here, a prediction made at the beginning of this section can be seen - the kinetic energy is transferred to the scattered photons.

Important to note is that if the atom is moving in the opposite direction, away from the incoming photon, the situation is utterly different. Then, in the atomic frame of reference, the light is even further red detuned, and the absorption is less probable. This means that such a group of atoms will not interact with light.

Multiple scattering events that reduce the momentum over time can be described as a force acting on atoms, which is equal to the photon momentum times the scattering rate [33]:

$$F_{scatt}(v) = \frac{\hbar k \Gamma}{2} \frac{s_0}{1 + s_0 + 4(\Delta - kv)^2/\Gamma^2} \tag{2.1}$$

where $s_0 = I/I_0$ is the saturation parameter[1], Γ is the natural linewidth of the transition, $\Delta = \omega - \omega_0$ is the detuning of laser light, and $k = 2\pi/\lambda$ is the corresponding wavenumber. We assumed the atom to move opposite to the laser beam (hence, negative sign next to k).

[1]Saturation intensity I_0 in a two level atom is the intensity of light at which the populations of the ground and excited states are equal. It leads to a significant reduction of the sample ability to absorb light.

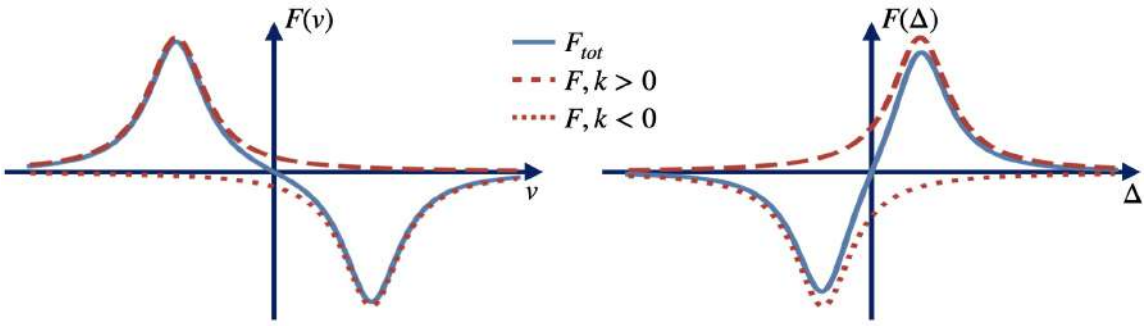

Figure 2.2: Plots of the force acting in optical molasses on an atom moving along z axis. Blue line represents the net force. Red dashed and dotted lines are the contributions coming from the beams propagating along and counter to the z axis, respectively. Left hand side: Force for different velocities of an atom. Note that the force sign is always opposite to the velocity sign, meaning it is decelerating atoms. Also, the negative linear dependence around $v = 0$ is visible. Right hand side: Force for different detunings of the laser beam, when atom moves along z axis ($v > 0$). For red-detuned beams the force is attractive (decelerating), whereas for blue-detuned beams it is repulsive (accelerating).

If we add a second laser beam with the same properties, but the opposite wave vector, which experimentally can be simply done by reflecting the laser beam onto itself, we get an additional term in the force with opposite sign:

$$F_{molasses}(\vec{v}) = \frac{\hbar k \Gamma}{2} \left(\frac{s_0}{1 + s_0 + 4(\Delta - \vec{k}\vec{v})^2/\Gamma^2} - \frac{s_0}{1 + s_0 + 4(\Delta + \vec{k}\vec{v})^2/\Gamma^2} \right) \tag{2.2}$$

which under approximation of low velocities $\vec{k}\vec{v} \ll \Gamma$ can be expressed as [34]:

$$F_{molasses} \approx -2\frac{\partial F}{\partial \omega} k v = -\alpha v \tag{2.3}$$

Similarly as in viscous media, it is proportional to the velocity. Atoms moving in an optical field therefore behave as if moving in honey or syrup and for this reason, this system is often called optical molasses. To gain some insight about this cooling method, we plotted the force calculated for different velocities and detunings and present it in Fig. 2.2

Until now, we have constrained the cooling mechanism to only one dimension. It is clearly visible that, after one iteration of the procedure, the atom may not

satisfy the velocity selection condition because it moves in a random direction, not necessarily along the axis of the laser beams. The situation changes if we introduce three orthogonal and retro-reflected laser beams effectively illuminating the atomic sample from each of six directions. Then the cooling process may be repeated and the atoms are successively decelerated.

An important aspect of Doppler cooling is the temperature limit, which arises from the fact that repetitive spontaneous emission causes the atom to recoil in a random direction. This gives rise to fluctuations of the momentum of the atom and a random walk of its velocity. The mean velocity is indeed equal to zero, however, the mean of the *square* of velocity, proportional to the temperature, is not. Therefore, the reachable temperature can be defined by the equilibrium between the momentum diffusion and the viscosity of the optical molasses [35, 36]. This parameter has a minimum for $\Delta = \Gamma/2$ [37], which is the so-called Doppler limit:

$$T_D = \frac{\hbar\Gamma}{2k_B} \tag{2.4}$$

for cesium and potassium equal to $T_{D,Cs} = 0.13\,\mathrm{mK}$ and $T_{D,K} = 0.14\,\mathrm{mK}$, respectively.

Another, much more fundamental limit comes from the recoil in a single spontaneous emission act. In a cooling scheme involving photon scattering, the atom gains a momentum kick equal to the momentum $p = \hbar k$ of the emitted photon. This corresponds to rise in kinetic energy given as $E_{kin} = p^2/2m$. In terms of temperature, the thermal energy acquired in such a process is given by $E_R = k_B T_R$. Combining these expressions, we get a formula [38]:

$$T_R = \frac{\hbar^2 k^2}{2mk_B} \tag{2.5}$$

where m is the mass of the atom. This limit is equal to $T_{R,Cs} = 0.099\,\mu\mathrm{K}$ for cesium and $T_{R,K} = 0.418\,\mu\mathrm{K}$ for potassium. It is often considered an ultimate limit in terms of cooling techniques based on photon scattering, however, some exotic methods have been developed that can cool atoms even beyond this restriction [38, 39].

2.2 Magneto-Optical Trap

The optical molasses provided a damping force responsible for cooling of the atomic sample, however, there was no mechanism for the trapping of the atoms. Another milestone was reported in 1987 by Raab et al. [40] who utilized a weak magnetic

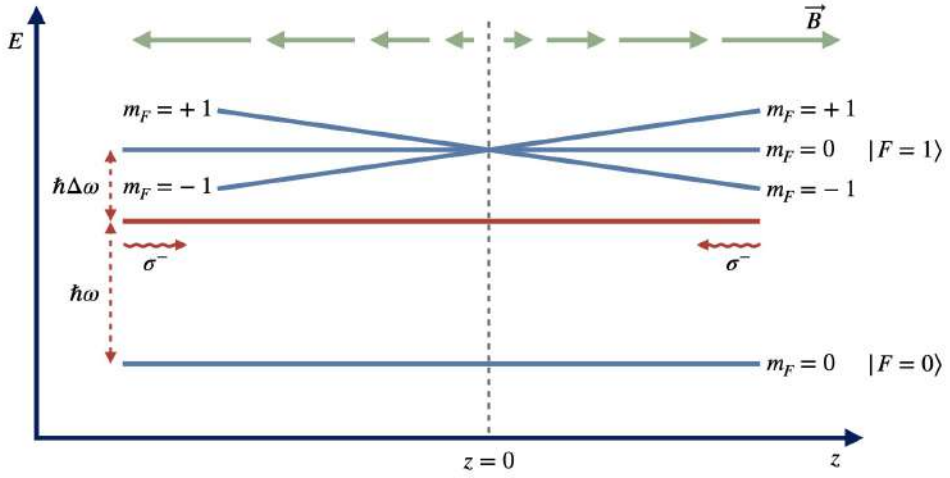

Figure 2.3: The scheme of a cross section of the magneto-optical trap. Blue lines correspond to the energy levels of the atom. Red line corresponds to the energy of the photons gauged at the atomic ground state level. Green arrows correspond to the magnetic field vector.

field gradient, which, as we will show in this section, added a spring-like term to the net force. They managed to trap 10^7 sodium atoms for two minutes, which was a breakthrough at the time. Soon in the 90's other elements were successfully trapped and a so-called magneto-optical trap (MOT) became a workhorse of the ultracold AMO physics. In this section, we will explain the principle of operation of this construction.

The magneto-optical trap can be considered as an extension of optical molasses, where a magnetic field is added. We shall make additional assumptions about the atomic energy structure, keeping it simple for the sake of clarity. That is, we will assume that the involved atomic states display a hyperfine structure with total angular momentum $F = 0$ and $F = 1$ for the ground and excited states, respectively. Then, each of the states has $(2F+1)$ degenerate magnetic sublevels labeled with the magnetic quantum number m_F. The $|g\rangle$ state has only one sublevel with $m_F = 0$, whereas the $|e\rangle$ state has three of them, $m_F \in [-1, 0, 1]$.

When a magnetic field $\vec{B}$ is introduced, the magnetic sublevels split due to the Zeeman effect. In the MOT the low-field regime is typically used, where the Zeeman splitting is linear with the field and given by the formula [34]:

$$\Delta E = \mu_B g_F m_F B \tag{2.6}$$

where μ_B is the Bohr magneton, g_F is the hyperfine Landé g-factor and B is the

value of the magnetic field.

In the MOT the quadrupole magnetic field is prepared, by a pair of coils in an anti-Helmholtz configuration. In the proximity of the zero-field spot, the magnetic induction increases linearly in every direction. A one-dimensional cross section of this geometry is shown in Fig. 2.3. When combined with the laser beams of optical molasses, the field extends the cooling capabilities of the system and introduces the position dependence of the force, which optical molasses lack.

The radiative force exerted on the atoms now also depends on the position in the trap. It can be introduced by modifying the Eq. 2.2 by adding a Zeeman shift $\mu' B(\vec{r})/\hbar$, where $\mu' = \mu_B(g_e m_e - g_g m_g)$ is the effective magnetic moment, which takes into account the energy shifts of both states $|g, m_g\rangle$ and $|e, m_e\rangle$. The formula for the one-dimensional (along z axis) radiative force in MOT is the following [38]:

$$\vec{F}_{MOT}(\vec{v}, \vec{r}) = \frac{\hbar k \Gamma}{2} \left(\frac{s_0}{1 + s_0 + 4\delta_+^2/\Gamma^2} - \frac{s_0}{1 + s_0 + 4\delta_-^2/\Gamma^2} \right) \tag{2.7}$$

where $\delta_\pm = \Delta \mp \vec{k}\vec{v} \pm \mu' B(\vec{r})/\hbar$. Note that the Doppler and Zeeman shifts have opposite signs for opposite beams.

Similarly, when expanding the formula around 0 in both velocity and position, we get:

$$\vec{F}_{MOT} \approx -\alpha \vec{v} - -\frac{\mu' \alpha \nabla B}{\hbar k} = -\alpha \vec{v} - \kappa \vec{r} \tag{2.8}$$

where we introduced the spring constant κ, and the damping coefficient α is the same as in Eq. 2.3. This formula is useful to gain intuition, as it shows that in MOT atoms are cooled due to the damping term and restored in the center of the trap due to the spring term.

The crucial point to note is that in MOT the polarization of light is deliberately chosen as circular left-hand (σ^-) with respect to the quantization axis defined by $\vec{B}$. Due to selection rules, such polarization induces only transitions with $\Delta m_F = -1$, which in our simplistic scheme means $|g, F = 0, m_F = 0\rangle \rightarrow |e, F = 1, m_F = -1\rangle$. This provides an asymmetry in the cooling process, effectively leading to trapping.

From the discussion about Doppler cooling, we see that the laser beam interacts only with atoms moving toward it. In MOT, this is valid for atoms on both sides of the zero-field spot. If an atom crosses this point, due to symmetry of the *value* of the magnetic field, the transition energy can be tuned to the light frequency and the momentum kick gained by absorption would accelerate it away from the trap center. However, because the σ^- polarized beams are used, crossing the zero-field spot flips the sign of the local quantization axis and atoms will actually feel the σ^+ polarization, which couples the $|g\rangle$ state to the state $|e, F = 1, m_F = +1\rangle$. Note

that this state is far detuned because of the Zeeman effect, so the atom will not interact with light. Such an asymmetry ensures that the laser beams push the atoms only toward the zero-field spot while cooling, which is the base mechanism for the trapping of the atoms.

The simplistic picture described above is not perfectly accurate if it comes to real experimental setups with alkali atoms. The mechanism behind cooling and trapping stays true, however, the energy structure is far more complicated. The ground state, for alkalies $S_{1/2}$, has two hyperfine sublevels, whereas the excited state, usually $P_{3/2}$, is split into four F' sublevels, each of which has even more magnetic ones. Therefore, there are many possible transitions that fulfill σ^- rules of choice.

Important to note is that the ground hyperfine splitting in the alkalies is usually much larger than the natural linewidth of the transition. This means that if an atom decays to the ground state that is not coupled by the cooling beam with the excited manifold, it no longer interacts with light. This would effectively pump the population to a dark state[2] and halt the cooling process. For this reason, the cooling transition is usually chosen between the higher ground state F_C and the excited state $F'_C = F_C + 1$, where C denotes the affiliation with the cooling light. This reduces the chance of a decay to the lower ground state because it is forbidden due to the selection rules for the dipole transitions[3].

However, there are two scenarios that can lead to a decay to the dark state. Firstly, an excited atom can undergo a non-radiative transition inside the excited manifold to another hyperfine state due to a collision with another atom. Then, the selection rules allow for a spontaneous emission to the dark state. A second scenario is that the cooling beam induces an off-resonant transition $F_C \to F'_C = F_C$ instead of $F_C \to F'_C = F_C + 1$, and then decay to the dark state is no longer forbidden.

Therefore, to close the cooling transition, a second weak beam is added, which couples the lower ground state F_R to the excited manifold, usually on a transition $F_R \to F'_R = F_R + 1$. It is called a repumper and, as the name suggests, its purpose is to pump the atoms that decayed to the dark state back to the cycling cooling transition.

This also explains the common choice of alkalies as investigated species. With a single valence electron they have a relatively simple energy structure and only two lasers are required to effectively close the cycling transition. More complex elements require more lasers, which poses an experimental challenge and also raises the costs. In addition, single electron on a valence orbit is easier to investigate in terms of theoretical studies.

[2] A dark state is not coupled by light with any other state via an allowed dipole transition

[3] Selection rules for the hyperfine dipole transitions allow for the F number change of -1, 0 or 1

The theory presented in this discussion assumes only a single-atom case, whereas in real experiments we have a statistical atomic probe of the order of tens or hundreds of millions of atoms. These, apart from interaction with light, undergo collisions, which may lead to random excitations or heating, thus ejecting atoms from the trap. Another heating contribution comes from absorption of the photons coming from spontaneous emission of other atoms.

Due to the heating processes involved, the MOT is a non-conservative trap, yet since it can be loaded directly from the background gas, at equilibrium the amount of atoms escaping the trap equals the number of newly caught ones. This, together with the ability to capture large numbers of atoms, makes it a perfect initial stage of every experimental sequence.

2.3 Magneto-Optical Trap dynamics

Single-species MOT dynamics

The dynamics of a single species MOT can be described with a phenomenological model based on predictions of Gallagher-Pritchard theory [41], which encompasses the loading and loss rates of various origins. In this section, we will describe the components of the model, write the loading equation explicitly, and discuss the two most common regimes of the dynamics.

The first parameter, the loading rate R, is derived from the capture theory. Its main assumption is that if an atom enters the trap region, it can be captured only if it has a velocity lower than the capture velocity v_c [42, 43]. This parameter depends on the trapping force and thus on parameters such as the size, detuning, and intensity of the laser beams, and the gradient of the magnetic field. As such, it is characteristic for a particular experimental setup and is not easily derived from the theory. However, it can be estimated by assuming the maximal deceleration $a_{max} = F_{max}/m$ exerted by the trapping force $F_{max} = \hbar k\Gamma/2$ on the travel length of the trap size L. Combining those parameters, we get the rule of thumb formula $v_c \approx \sqrt{2a_{max}L}$.

The loading rate is given by the atom number taken from the Maxwellian velocity distribution up to the capture velocity times the transverse area of the trap [44]:

$$R = \pi w_T^2 n_{BG} \left(\frac{m}{2\pi k_B T}\right)^{3/2} \int_0^{v_c} v^3 \exp\left(-\frac{mv^2}{2k_B T}\right) \mathrm{d}v \tag{2.9}$$

where w_T is the waist of the trapping beam and n_{BG} is the density of the background vapor. The capture velocity is much smaller than the mean thermal velocity of

the background gas, so the exponent in the Maxwell distribution integral can be approximated by unity. Then the formula takes the following form:

$$R \approx \pi w_T^2 n_{BG} \left(\frac{m}{2\pi k_B T} \right)^{3/2} \frac{v_c^4}{4} = n_{BG} \sigma_c \frac{v_c^4}{v_{th}^3} \tag{2.10}$$

where σ_c is the capture cross section and v_{th} is the mean thermal velocity of the background vapor. The dependence of the loading rate as the fourth power of the capture velocity has been verified by multiple groups [45, 42, 46].

With the loading rate described, we will now move on to the loss channels and focus on two possibilities, one and two-body losses. Although higher order collisions do occur, they are usually negligible due to low densities of the MOT.

The first loss channel comes from the collisions of the captured atoms with the background gas and is described by a parameter γ_{BG}. It is always present, but can be minimized by improving the vacuum conditions. However, in single-cell setups, where MOT is loaded directly from the vapor, it gives a non-negligible contribution and is hard to eradicate. This channel is considered as one-body loss, since only one atom from the trap participates in the collision.

The second loss channel, described by Alan Gallagher and David Pritchard [41] and verified by David Sesko et al. [47], induces the two-body losses in the trap. The two most common effects are the fine-structure changing (FSC) and the radiative escape (RE). These processes depend on the density of the MOT and can be expressed as a loss coefficient β times the integral of the atomic density over the trap volume.

The fine-structure changing is an inelastic process, where atoms undergo a non-radiative transition during the collision to a lower fine-structure energy level. The energy surplus coming from the internal energy is converted to the kinetic energy, so that one of the atoms may escape the trap. Light does not participate in the process, however, it is needed to excite the atoms prior to the collision. It can be described explicitly with a scheme [41]:

$$A + A + \hbar\omega \rightarrow A_2^*(S_{1/2} + P_{3/2}) \rightarrow A^*(P_{1/2}) + A(S_{1/2}) + \Delta E_{FS} \tag{2.11}$$

where we also assumed typical atomic terms for alkali elements, $A_2^*(S_{1/2} + P_{3/2})$ denotes a molecule in Hund's case c[4] correlated with the $S_{1/2}+P_{3/2}$ atomic asymptote, asterisks stand for an electronic excitation, and ΔE_{FS} is the energy difference of the

[4]Hund's case c means that the spin-orbit coupling dominates over the electron-nuclei coupling and therefore the good quantum number to describe the molecular state is the total projection of the electronic angular momentum onto the internuclear axis. It is the most common type for alkali molecules with atomic asymptotes $S_{1/2} + P_J$

excited states of the fine structure, which is equal to $\approx 797\,\mathrm{K}$ and $\approx 83\,\mathrm{K}$ for ^{133}Cs and ^{39}K, respectively. Half of this energy is transferred to each atom in nuclear kinetic form which leads to escape of both atoms from the trap.

The radiative escape is a light-assisted process, where the MOT beams photoassociate two atoms that are in a Condon point[5] to a molecular state. If the molecular potential is attractive, the atoms accelerate toward each other, reducing the internuclear distance and gaining kinetic energy. At some point, they spontaneously emit a photon and dissociate, releasing the energy acquired in the molecular state, which can lead to escape from the trap. This process heavily depends on the laser beam detuning and power, but also on the molecular structure of the atoms trapped. It is described by a scheme [41]:

$$A + A + \hbar\omega \rightarrow A_2 \rightarrow A + A + \hbar\omega' \tag{2.12}$$

where $\omega > \omega'$ and the energy transferred to each atom at the end is equal to $\hbar(\omega - \omega')/2$.

MOT rate equation

We discussed the main source and loss channels in the MOT, so now we can combine them in a rate equation for the number of atoms N present in the MOT [48]:

$$\dot{N} = R - \gamma_{BG} N - \beta \int_V n^2(r,t) d^3r \tag{2.13}$$

Due to the presence of two-body losses, the spatial distribution of the atomic density needs to be included and integrated over the volume of the trap. There are two regimes which simplify the integration and give simple solutions to Eq. 2.13.

The first is the low-density approximation, where the density can be expressed as a Gaussian distribution $n(r,t) = n_0(t)e^{-r^2/w^2}$. The integral in Eq. 2.13 can be performed directly and the equation has a complicated, yet analytical solution [49]. In this regime, the peak density increases linearly with the number of captured atoms, while the volume stays constant. The geometry of the trap is mostly governed by the laser beams, and the loading equation reads:

$$\dot{N} = R - \gamma_{BG} N - \frac{\beta N^2}{(2\pi)^{3/2} w^3} \tag{2.14}$$

[5]Condon point is the internuclear distance R_C for which the laser is resonant with a molecular transition.

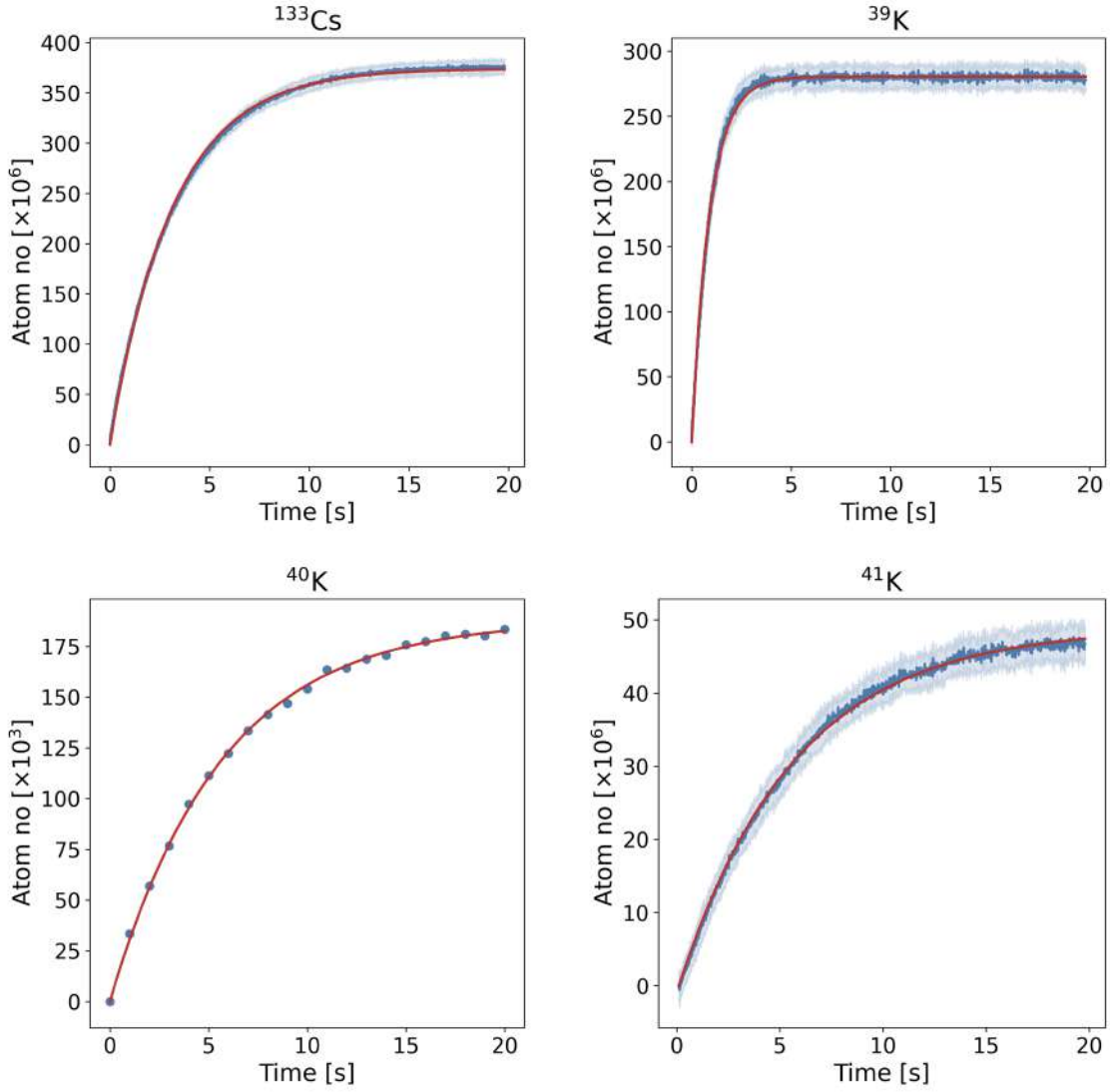

Figure 2.4: Measurements of fluorescence of MOT loading process for various species that we can trap in our apparatus. The cesium, potassium-39 and potassium-41 curves were measured on a photodiode, whereas potassium-40, due to low natural abundance, required higher sensitivity provided by fluorescence imaging with a camera. Shaded areas correspond to standard deviation of 20 iterations. Red curves are fits of Eq. 2.16.

The second regime is the high-density approximation, where the density is constant. Usually MOTs larger than 10^5 of atoms expand linearly in volume as the number of atoms captured increases, while maintaining a constant density at the center. In this regime atoms interact not only with the cooling laser light, but also with photons scattered by other trapped atoms. Such re-scattering exerts a repulsive force on atoms and the center of the trap stabilizes in terms of density. We can define a mean density $\bar{n}$ and rewrite the loading equation as follows:

$$\dot{N} = R - (\gamma_{BG} + \beta\bar{n})N \tag{2.15}$$

and introduce the total loss coefficient $\gamma = \gamma_{BG} + \beta\bar{n}$. This regime has a simple analytical solution:

$$N(t) = N_\infty(1 - e^{-\gamma t}) \tag{2.16}$$

where $N_\infty = R/\gamma$ is the number of atoms captured in the trap in the steady state. If the MOT density is low, then the major contribution to trap losses comes from the background vapor, and we can approximate $\gamma \approx \gamma_{BG}$. Exemplary curves of the MOT loading process, captured for cesium and all three natural isotopes of potassium, are presented in Fig. 2.4.

Most of the experiments treat MOT as a first step of the experimental sequence which sole purpose is to cool and gather the highest number of atoms possible. For this reason, they operate mostly in the high-density regime.

Dual-species MOT dynamics

The Magneto-Optical Trap dynamics can also be discussed in a dual-species case. Then, an additional loss rate factor needs to be included, as the presence of another species opens a new two-body collision channel. Taking this into consideration, the number of captured atoms of species A with a population of species B present in the trap follows the equation [50]:

$$\dot{N}_A = R - \gamma_{BG}N_A - \beta_A \int_{V_A} n_A^2 d^3r - \beta_{AB} \int_{V_A} n_A n_B d^3r \tag{2.17}$$

This equation has a conjugate counterpart, where the A and B indexes are interchanged, forming a set of differential equations. The solution in general is complicated, though some analytical approximations can be derived. One is assuming that the MOT for one species is much smaller than the other. In such a scenario, the larger MOT, with constant density, acts similarly to the background gas.

2.4 Sub-Doppler cooling

In this section, we will briefly describe the mechanism behind the sub-Doppler cooling, which is usually a succeeding stage of the experimental sequence, after MOT. It is a useful tool for decreasing the temperature of the atomic probe beyond the Doppler limit reachable in MOT.

Polarization gradient cooling

In 1988, in experiments with optical molasses of sodium, it was surprisingly discovered that the obtained temperature was equal to $T = 43\,\mu$K, which was much lower than the Doppler temperature $T_{D,Na} = 240\,\mu$K [2]. This violation of the commonly acknowledged limit was soon confirmed by other groups for sodium [51] and cesium [52], and later for rubidium [53] and finally potassium [54]. As a side note, the latter was considered a problematic member of the alkali family due to excited state splitting of the order of the natural linewidth, which leads to heating of a cold sample by photon reabsorption [36].

The mechanism of the observed sub-Doppler cooling was explained by Jean Dalibard and Claude Cohen-Tannoudji in 1989 [1]. This work and other substantial contributions to the field of laser cooling and trapping have won Cohen-Tannoudji the Nobel Prize [39].

The sub-Doppler cooling takes advantage of the hyperfine splitting of the ground level and its magnetic sub-states, which was not yet introduced in our discussion. However, in realistic systems with alkali atoms the fine structure ground level with $S_{1/2}$ term has two hyperfine states. It is possible, by clever coupling with light, to introduce a new cooling mechanism which can break the Doppler limit.

The most common variant of sub-Doppler cooling, widely discussed in the literature, is the so-called polarization gradient cooling (PGC), which is naturally present in optical molasses. It has two variants based on the configuration of the polarizations of the laser beams forming the optical molasses, the lin$\perp$lin and the σ^+-σ^-. As Dalibart and Cohen-Tannoudji showed [1], when such beams are counterpropagating, they form a standing wave which polarization changes in space.

In the lin$\perp$lin case, it forms an alternating sequence of circular and linear polarization with a period equal to $\lambda/2$. Because of the AC Stark effect, the polarization gradient creates a ridged landscape of energy shifts of the ground state. This is of course valid only for the transitions between magnetic sublevels, which have different coupling strengths for different polarizations, given by the Clebsch-Gordan coefficients [38]. An atom moving in such a landscape has to climb a potential hill,

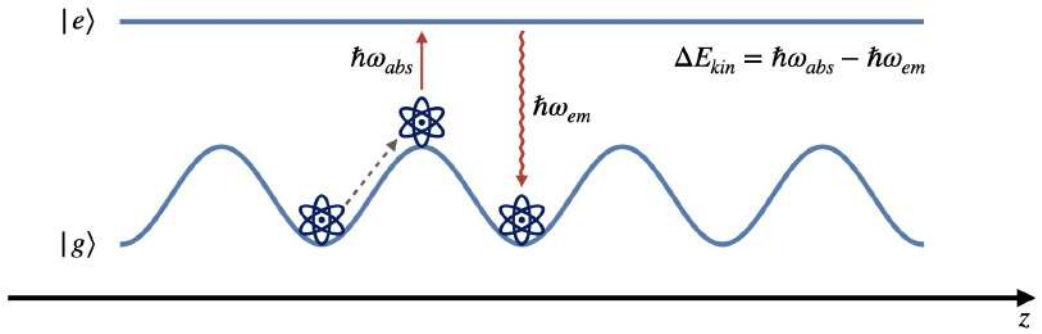

Figure 2.5: Graphical illustration of the Sisyphus cooling. The energy of the ground state $|g\rangle$ is modulated spatially due to polarization gradient of the laser beams. Upon reaching the hill of the potential the atom is excited and decays back to the valley of the ground state.

and upon reaching the top it is optically pumped to the excited state. Then, a spontaneous emission follows, bringing the atom back to the ground state at the bottom of the potential hill, which is the most probable due to the values of the Clebsch-Gordan coefficients [34]. Therefore, the kinetic energy that is converted into the potential energy by climbing up the hill is lost in the process, leading to cooling of the atom. The graphical illustration of this phenomenon is shown in Fig. 2.5.

A repetitive climb-and-fall scheme is strikingly parallel to the fate of Sisyphus, the mythical ruler of Corinth. According to the Greek tale, he was sentenced to eternal torment for capturing the god of death Tanatos. His punishment was to roll a giant boulder up a hill, yet just before the top, the rock was always slipping out of his hands. Due to the similarity, and maybe a bit of dramaturgy, the cooling mechanism described above is also called Sisyphus cooling.

In the σ^+-σ^- case, the net polarization is always linear and rotates along the z axis, forming a corkscrew pattern. As shown in [1], this polarization pattern does not provide the landscape of hills and valleys required by Sisyphus cooling. There is, however, another mechanism of cooling. Considering resting atoms, we find that in the presence of an optical field, the distribution of the population of the magnetic sublevels is defined by the local polarization of the light. In case of atoms moving through a rotating polarization region, this distribution lags behind the steady state defined by the local polarization axis. This delay causes an imbalance in the population, and due to the values of Clebsch-Gordan coefficients scattering of atoms is stronger for the beam propagating opposite to their velocity [38]. This effect results in a damping force that lies behind the cooling.

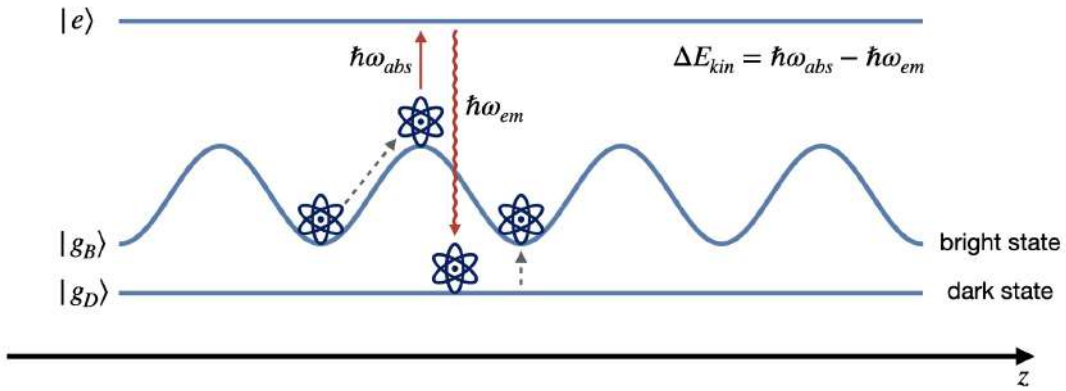

Figure 2.6: Graphical illustration of the gray molasses cooling. The energy of the bright state $|g_B\rangle$ is modulated spatially due to polarization gradient of the laser beams. Upon reaching the hill of the potential the atom is excited and decays to the dark state $|g_D\rangle$. If the atom is still hot enough, it can be transferred back to the valley of the bright state

Gray molasses cooling

Further enhancement of the PGC, called gray molasses cooling (GMC), utilizes both of the hyperfine ground states, which are common in alkalies. In such a scheme, the higher ground level is considered a bright state $|g_B\rangle$ that is coupled by the light with the excited state and the lower ground level is a dark state $|g_D\rangle$ which, in turn, does not interact with the optical field, yet can be reached via spontaneous emission from the excited state. The method takes its name from the two states, which are crucial for its operation, gray as a mixture of bright and dark.

The bright state experiences a spatially varying energy shift, suitable for the Sisyphus mechanism. Upon reaching the top of the hill, the atoms are excited and decay to the dark state. There, they can be transferred back to the bright state at the point where the bright state energy is minimal. However, this effect is velocity-selective, so only hot enough atoms reenter the cooling cycle in the valley of the bright state [55]. The coldest atoms are trapped in the dark state, which shields them from additional scattering and preserves their temperature below the Doppler limit. The graphical illustration of this process is shown in Fig. 2.6.

This method differs from the standard optical molasses, not only in terms of the utilization of both ground states, but also that it works when the laser light is blue-detuned, instead of red-detuned. It was first introduced in the case of cesium cooling by Boiron et al. [56] in the 4-beam configuration and later in the 6-beam

configuration [57].

Although the mechanism of the method seems general, some variations needed to be developed to successfully implement it with other alkalies. For example, in the case of potassium, the small splitting of the excited state makes the standard approach inefficient [54], so it is usually implemented on the D_1 line. Another variation is to use two laser beams, a cooler and a repumper in the Λ configuration, that drive Raman transitions. Both beams are blue-detuned, and their frequencies must differ by the hyperfine splitting of the ground state to satisfy the two-photon Raman condition [58]. Because of the light coupling scheme, this method is called Λ-enhanced GMC.

The temperature reached in gray molasses cooling strongly depends on the detuning of the cooling beam or the Raman condition, so these parameters must be carefully adjusted [59, 60].

Another important factor is the presence of magnetic field. Even fields of the order of 1 mG have been reported to strongly influence the temperature reached in PGC [61, 62] and GMC [63, 59]. To our knowledge, the explicit dependence has not yet been studied theoretically, however, phenomenologically a quadratic relation has been shown $\Delta T = \alpha B^2$, where $\Delta T = T - T_{min}$ is the increase of the temperature in reference to the minimal obtainable in the GMC. The proportionality constant α is usually of the order of a few hundred microkelvins per Gauss square ($532\,\mu\mathrm{K/G^2}$ for cesium [63] and $300(100)\,\mu\mathrm{K/G^2}$ for potassium 39 [59]). Therefore, a proper compensation of the stray magnetic fields needs to be considered, since, for example, the omnipresent magnetic field of the Earth is of the order of 0.5 G (for example 0.505 G for Warsaw [64]).

The last feature, which we would like to discuss, is the time duration of the cooling. As no magnetic fields can be present during the process, there are no trapping mechanisms, so an extended cooling period would cause the atomic cloud to vanish. However, the GMC requires as short times as a few milliseconds to cool the atoms to the microKelvin range, so it can be an intermediate step between two trapping stages of an experimental sequence providing an additional cooling stage.

2.5 Optical dipole trap

In the last section of the chapter, we will introduce the concept of an optical dipole trap (ODT), sometimes also called far-off-resonance trap (FORT). It has the advantage of being a conservative type of trap, which means that there are no dissipation mechanisms involved, and thus there is no limit of achievable temperature. In ad-

dition, it does not require a magnetic field for operation, so no position-dependent energy shifts are present. The main disadvantage is that it cannot be loaded directly from the background vapor and requires sufficiently low entrance temperatures to capture a meaningful number of atoms. For this reason, it is the last and ultimate trap in the experimental sequence, and hence the discussion is also placed at the end of this chapter.

The idea of using focused light to trap entities comes from the work of Arthur Ashkin. In 1970 he demonstrated trapping of micrometric diameter latex spheres freely suspended in water by radiation pressure of two counterpropagating laser beams [65]. In this very work, he also envisioned "In general, atoms and molecules are quite transparent. However, if one uses light tuned to a particular transition, the interaction cross section can be much larger than geometric". In the following years, the method was developed and the trapping of liquid droplets [66] and Mie and Rayleigh particles [67] was demonstrated. For his contribution to the field of trapping with optical tweezers, Ashkin was awarded the Nobel Prize [68] in 2018 (two years before his death). Although the prize motivation focuses on biological applications, his work substantially contributed also to the field of ultracold physics.

The first observation of optically trapped sodium atoms [69] is associated with Steven Chu, another Nobel Prize laureate [31]. Although a milestone, this experiment trapped only 500 atoms, which is incomparable with modern traps capable of capturing millions of them. The development of the method and also of the laser technology ultimately provided means to reach the quantum degeneracy regime by formation of the Bose-Einstein condensate [70], often regarded as the pinnacle of the ultracold experiments.

The dipole force

The principle of operation of the optical dipole trap bases on the interaction between the gradient of the optical field and the induced polarization of the atomic dipole moment. We will follow the derivation presented by Grimm et al. [71]. An atom placed in an electric field $\vec{E}$ responds with reorientation of its dipole moment $\vec{p}$, which oscillates with the field driving frequency ω. The two are related through a complex parameter α called polarizability:

$$\vec{p} = \alpha \vec{E} \tag{2.18}$$

The interaction potential comes from the averaging of the product of electric field and dipole moment over many oscillations. The included one-half factor comes from averaging of the square of the sine, which is due to the fact that the dipole is induced

and co-oscillating with the field.

$$U_{dip} = -\frac{1}{2}\langle \vec{p}\vec{E} \rangle = -\frac{1}{2\varepsilon_0 c}\mathfrak{Re}(\alpha) I \tag{2.19}$$

where we introduced the light intensity $I = 2\varepsilon_0 c|\vec{E}|^2$.

This potential depends solely on the position, so the force acting on an atom is given by the negative gradient of the potential:

$$\vec{F}_{dip}(\vec{r}) = -\nabla U_{dip}(\vec{r}) = \frac{1}{2\varepsilon_0 c}\mathfrak{Re}(\alpha)\nabla I(\vec{r}) \tag{2.20}$$

This formula shows that the dipole force is conservative and depends on the *gradient* of the intensity of the laser beam. The real part of the polarizability corresponds to the dispersive properties of the interaction, in-phase with the driving field.

The polarizability has also an imaginary part responsible for the absorption, or in other words the out-of-phase interaction. This component describes the power absorbed from the driving field and is given by:

$$P_{abs} = \langle \dot{\vec{p}}\vec{E} \rangle = \frac{\omega}{\varepsilon_0 c}\mathfrak{Im}(\alpha) I \tag{2.21}$$

which is usually considered in terms of scattering rate, as the photons absorbed from the beam are further spontaneously emitted:

$$\Gamma_{scat}(\vec{r}) = \frac{1}{\hbar\varepsilon_0 c}\mathfrak{Im}(\alpha) I(\vec{r}) \tag{2.22}$$

This derivation is general for any particle. We will now discuss an atomic case, where polarizability has a specific form, which determines the interaction with the laser beam.

Dipole potential in atomic case

The polarizability of an atom can be derived in a semi-classical model, considering a quantum two-level atom in the presence of a classical laser field. This consideration was an important element of my master thesis, where the full derivation is presented [72]. Assuming an interaction Hamiltonian $\hat{H}_I = -\hat{p}E$ and a rotating wave approximation (RWA) we can derive the optical Bloch equations (OBE) of the system. There, we add a decay factor, corresponding to the finite lifetime of the

excited state. In the end, we get that the complex polarizability for a low-saturation case is given by [73]:

$$\alpha = -\frac{|d|^2}{\hbar}\frac{1}{\omega - \omega_0 + i\Gamma/2} \tag{2.23}$$

where d is the dipole moment, ω_0 is the transition frequency, and Γ is the natural linewidth of the excited state. In spite of high optical power in ODT, the low-saturation assumption is not violated because, at the same time, the laser is far-detuned.

With such a form of the polarizability, the potential and scattering rate can be expressed in terms of laser detuning Δ [71]. A plot of these quantities calculated for different wavelengths is shown in Fig. 2.7, where we assumed an intensity profile of a Gaussian beam focus with waist at focus $w_0 = 240\,\mu$m and power $P = 40\,$W.

$$U_{dip}(\vec{r}) = \frac{3\pi c^2}{2\omega_0^3}\frac{\Gamma}{\Delta}I(\vec{r}) \tag{2.24}$$

$$\Gamma_{sc}(\vec{r}) = \frac{3\pi c^2}{2\hbar\omega_0^3}\left(\frac{\Gamma}{\Delta}\right)^2 I(\vec{r}) \tag{2.25}$$

The polarizability given by Eq. 2.23 above can be decomposed into real and imaginary parts. Let us now discuss how they complement the description of atomic motion in the dipole trap.

Considering a focused Gaussian beam and a typical dispersion curve of an atom, we find that the force given by Eq. 2.20 is always directed towards the waist of the beam for the red-detuned light, thus attractive. For the blue-detuned light the situation is opposite, and the force is repelling atoms from the focus towards the low-intensity regions of the beam.

It is usually more convenient to describe the trapping in the language of the potential, which depth U_0 can be expressed in Kelvins. Then it is easy to estimate the power or detuning required for a given application based on the initial temperature of the atoms. Worth mentioning is the fact that the gravitational potential should also be included as it decreases the trap depth. This consideration is important for shallow traps or the final stages of evaporation cooling.

Another important parameter is the trap frequency ω_{trap}, which is defined by approximating the trapping potential with the potential of a harmonic oscillator. This approximation is valid because the trapping potential can be considered harmonic around the center of the trap. There are actually two trap frequencies, the longitudinal and the radial, due to the Gaussian beam symmetry.

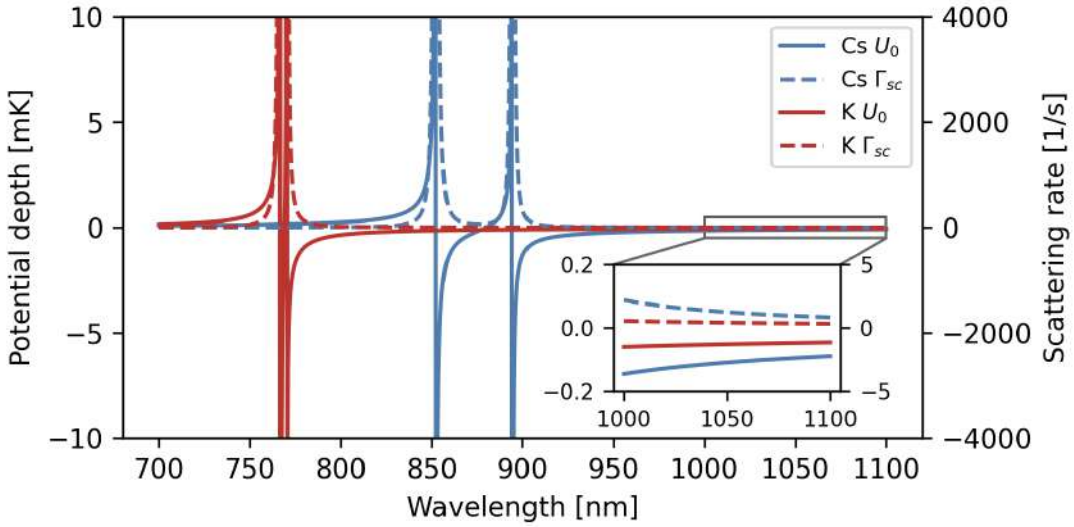

Figure 2.7: Potential depth U_0 (solid lines) and scattering rate Γ_{sc} (dashed lines) for cesium (blue) and potassium (red). Repulsive-attractive crossings correspond to D_2 and D_1 lines wavelengths. Laser parameters used for calculations were: power $P = 40\,\mathrm{W}$ and waist $w_0 = 240\,\mu\mathrm{m}$. Inset shows magnification of a region with 1064 nm wavelength, which is commonly chosen for dipole traps. Inset axes and units correspond to the ones in the main plot.

The above approach also gives insight into the mechanism of trapping. In such a scheme, the atoms moving in the beam region experience shifts of energy levels as a result of the AC Stark effect. A comment from the author, I always like to think about it as an example of the least action principle, where the atoms tend to localize in the lowest energy state.

As for the imaginary part of the polarizability, it is described by a Lorentzian curve, thus always positive, which means that the scattering is inevitable. As it is the fundamental heating mechanism in ODT, it also limits the achievable trap lifetime.

In the far-detuned case, scattering is completely elastic, and the increase in thermal energy per scattering event is equal to the recoil energy E_R. If we assume a thermal equilibrium and a scheme of a 3D red-detuned harmonic trap, we get the equation for the heating rate [71]:

$$\dot{T} = \frac{1}{3} T_R \bar{\Gamma}_{sc} \tag{2.26}$$

where T_R is the recoil temperature defined in Eq. 2.5 and $\bar{\Gamma}_{sc}$ is the mean scattering

rate. If the potential well is much deeper than the thermal energy of the atoms $U_0 \gg k_B T$ we can rewrite it in terms of detuning:

$$\dot{T} = \frac{1}{3} T_R \frac{\Gamma}{\hbar|\Delta|} U_0 \tag{2.27}$$

where the linear dependence on intensity is hidden in the potential depth U_0.

Experimental application

The ODT has many advantages like ability to coherently conserve the atomic quantum state or possibility to implement evaporation cooling. However, as the discussion has already shown, it has a limited lifetime, which we would usually like to be as long as possible. We will now investigate what tools we have, to optimize the balance between the scattering and the potential depth.

Equations 2.24 and 2.25 show that the dependence on the laser intensity in both cases is linear, however, the scaling with the detuning is different. As we decrease the frequency of the trapping laser, the scattering, thus heating, falls as Δ^2, whereas the potential depth decreases as Δ. It is clearly visible in the relation between the two:

$$\hbar \Gamma_{sc} = \frac{\Gamma}{\Delta} U_{dip} \tag{2.28}$$

This indicates that there exists a trade-off point, where the scattering is reduced to a few events per second, which gives a lifetime of the order of seconds, yet the potential depth is of the order of hundreds of microkelvins, see the inset in Fig. 2.7. We must also consider the technological aspect, as high-power lasers are not always available for any given wavelength. The first experiments with optical dipole trap used light detuned by hundreds of gigahertz from the transition, which caused a substantial scattering rate.

The last thing which we would like to discuss are the requirements regarding the laser in terms of the heating induced by its instability. There are two main mechanisms, parametric heating and driven heating [74, 75].

The first one is caused by fluctuations in the intensity of the laser beam, which modulate the trap frequency and the atomic motion. If the noise spectrum of the laser spans to the second harmonic of ω_{trap}, a parametric resonance occurs, which heats the atoms exponentially.

The driven heating occurs if the laser beam is fluctuating in terms of position in space, which moves the trap minimum accordingly. Atoms that try to keep up with the fluctuation can fall into resonance with the trap, which causes heating that is linear with time.

Both mechanisms do not depend on the scattering rate of the trap, so they can dominate even if the detuning is large. For this reason, the ODT laser must have low relative intensity noise (RIN) in the $1 - 100\,\mathrm{kHz}$ band, which is a typical range for ω_{trap}. In addition, the beam-pointing stability is crucial, especially for tight potentials. Considering the high power used for the trapping, effects such as thermal lensing also need to be taken into account.

Fortunately, the development of laser technologies provided researchers with high-power and high-stability devices, with wavelengths suitable for the construction of ODT, such as solid-state Nd:YAG lasers or ytterbium-doped fiber lasers operating at 1064 nm. In conjunction with optical amplifiers, they can reach tens of watts of available power. This made them a frequent choice in many laboratories.

Chapter 3

K-Cs apparatus at the University of Warsaw

In this chapter, I will present the K-Cs apparatus, which is the main experimental platform at the Ultracold Quantum Gases Laboratory at the Faculty of Physics, University of Warsaw. I was involved in construction of the vacuum chamber during my Master studies and contributed to development of essential features enhancing operation of the apparatus during my PhD studies.

The layout of this chapter is as follows. I will begin with a general description of the apparatus and highlight its capabilities. I will also discuss some lesser improvements that I made regarding the control of the magnetic field, laser locking, and fluorescence imaging. Then I will proceed with the characterization of the magneto-optical trap and study on a method for altering its loading rate by light-induced atomic desorption (LIAD). I will finalize this chapter with a description of a bi-directional current driver for the compensation coils and the measurements performed to optimize the stray field cancellation in our system.

3.1 The K-Cs apparatus

The construction of the apparatus began around 2017 and was finished in a minimal operating state in 2019, when we observed for the first time cold samples of cesium and potassium-39 in magneto-optical trap. In the following years, the setup was expanded to incorporate, among others, fluorescence and absorption imaging, sub-Doppler cooling, Zeeman spin pumping, and an optical dipole trap. We also obtained MOTs of other potassium isotopes, namely ^{40}K and ^{41}K, of which the former is a fermionic species.

The setups for ultracold experiments consist of many complex subsystems, like the vacuum chamber, laser systems for cooling, imaging and dipole trapping, and systems for generation of magnetic fields, just to name a few. All of these need to be combined to form an operational hardware layer of the setup. In addition, a software layer needs to be developed for the control over various devices and for data acquisition, so that the experimental sequences run smoothly. Given such a level of complexity, building an ultracold apparatus is rarely a solitary job.

Regarding this project, several researchers have contributed over the past few years:

- **Paweł Arciszewski** - principal constructor of the vacuum chamber, the cesium laser system, and the dipole trap [76]. Also responsible for the design and implementation of the data acquisition architecture and a web-based data analysis tool [77].
- **Mateusz Bocheński** - expert in the field of potassium. Designer and constructor of the laser system capable of preparing light for all three natural isotopes of potassium [78]. Also contributed to many optical setups in the system.
- **Koray Dinçer** - responsible for the construction of objectives in the imaging system and improvements in the experiment control hardware. Constructor of the first laser setup with Ti:Sapphire lasers [79].
- **dr Mariusz Semczuk** - principal designer and investigator of the project. Responsible for the idea, direction of the research, and funding in our laboratory.
- **Jakub Dobosz** - I was responsible for the winding and assembly of the MOT, Feshbach, and compensation coils and helped with the assembly of the vacuum chamber. I also made various improvements to the electronic hardware of the control of the experiment.

The vacuum chamber

The vacuum chamber of the apparatus, presented in Fig. 3.1, is designed as a single-cell setup, with central part being an ultra-high vacuum (UHV) quartz cell. Other components of the chamber include an ion pump, which is responsible for maintaining the UHV conditions, a titanium sublimation pump, which we sometimes utilize to "clean" the vacuum, an electric feedthrough, which delivers electric current

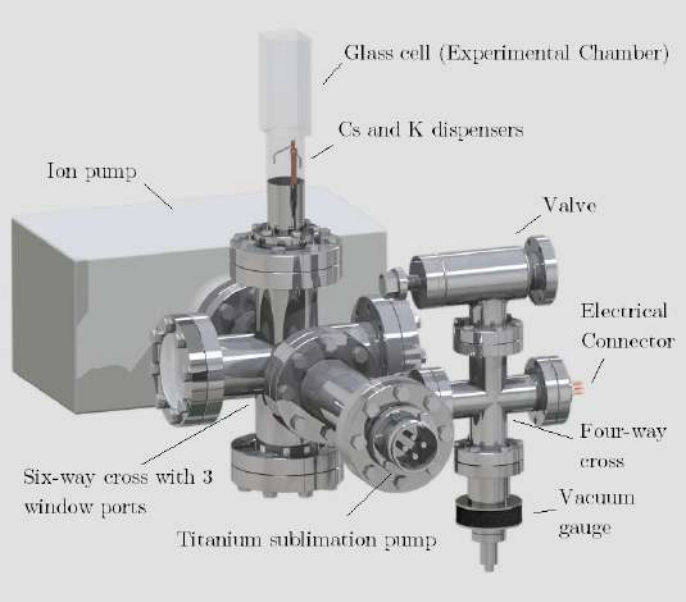

Figure 3.1: The design of the vacuum chamber. Image by courtesy of P. Arciszewski.

to the atomic source, and an inverted magnetron vacuum gauge, which is our vacuum sensor.

In our setup, the atoms come from the natural abundance dispensers placed in the neck of the experimental cell. By adjusting the current running through the dispensers, we can control the amount of atoms emitted, and thus the background vapor pressure in the cell. Therefore, they are the main source of vacuum contamination.

The vacuum chamber is placed and secured in an aluminum frame, filled with lead pellets for greater stability, and attached aluminum optical breadboards. They are placed both horizontally and vertically around the experimental cell to maximize the amount of available space for the optical setups. All metal components are made of aluminum and are connected with non-magnetic A4 steel screws to decrease the induced magnetization of the frame.

More details about the assembly, bake-out procedures and obtaining the UHV in the vacuum chamber can be found in the master thesis of P. Arciszewski [76].

Magnetic fields

The magnetic fields in the setup are generated by three sets of coils, the offset (also called Feshbach or FSH), the gradient (also called MOT) and the compensation coils.

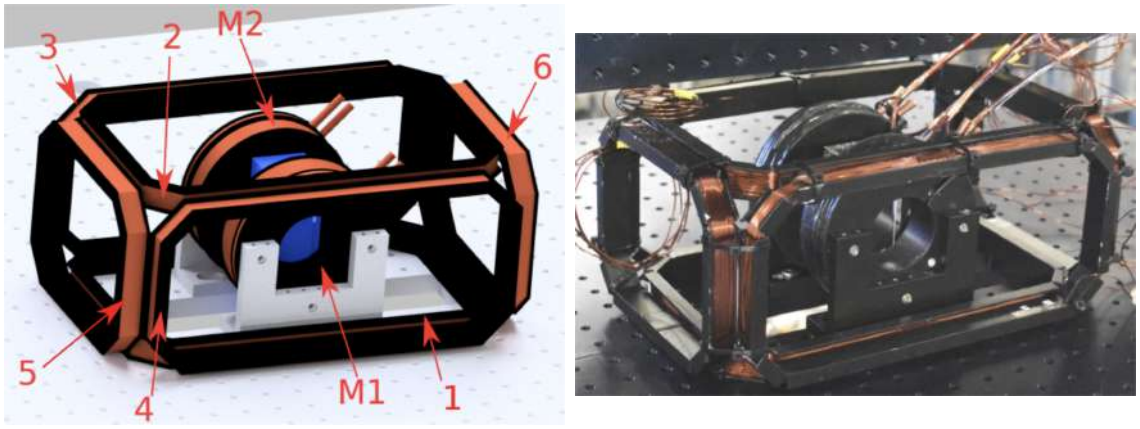

Figure 3.2: The design and photograph of the assembled coils. The outer cage are the compensation coils and the ring-shaped casing in the middle holds the FSH and the MOT coils. Images by courtesy of P. Arciszewski.

The design and a photograph of the assembled coils are presented in Fig. 3.2.

The first two sets consist of pairs of coils in Helmholtz and anti-Helmholtz configuration[1], the main purpose of which is to generate a uniform field for Feshbach spectroscopy and a gradient field for trapping in MOT and magnetic trap, respectively. The resistance and inductance of each coil are presented in Tab. 3.1. The data was measured by P. Arciszewski, details of the procedure can be found in [76].

Coil	**MOT 1**	**MOT 2**	**FSH 1**	**FSH 2**
$R\,[\mathrm{m}\Omega]$	43.9(6)	42.4(6)	72(1)	72(1)
$L\,[\mu\mathrm{H}]$	97.8(16)	97.8(16)	175(16)	175(16)

Table 3.1: Resistance and inductance of MOT and FSH coils. Data was measured by P. Arciszewski [76].

The coils are wound on two mirror-imaged aluminum casings, with the FSH coils being the inner, and the MOT coils being the outer. The casing is cut radially in one place to eliminate the formation of eddy currents. It was also painted black to absorb any unwanted reflections of the laser beams from the cell surface.

As the current source for the MOT and FSH coils we use two high-power programmable DC power supplies from Delta Elektronika[2]. We utilize the external

[1] In here Helmholtz (anti-Helmholtz) means that the current is flowing in the same (opposite) direction. The distance between the coils is not necessarily equal to their radius.

[2] SM70-45 for MOT coils and SM45-70 for FSH coils

current mode, where the output current is adjusted based on analog voltage on the control input of the supply.

The compensation coils set consists of 3 pairs of coils, which are wound on aluminum casings designed with such shapes that they form a cuboid cage. Each pair operates in Helmholtz configuration to produce a uniform field in the center of the glass cell and by superposition provide an arbitrary magnetic field vector in any direction in space. Their main purpose is to compensate for the stray magnetic field in the glass cell, which is mostly coming from the Earth's magnetic field. We also utilize them to define the quantization axis for the Zeeman spin pumping.

The current source of the compensation coils is our custom-made bi-directional current supply, which will be described in detail in Sect. 3.3. It is capable of delivering $\pm 4\,\mathrm{A}$ of DC current based on analog control voltage. Usually, we use currents of the order of tens of milliamperes, which is sufficient to cancel the stray magnetic field or create a quantization axis.

Coil	**1**	**2**	**3**	**4**	**5**	**6**
$R\,[\Omega]$	1.023(20)	1.027(18)	1.155(20)	1.144(20)	0.966(17)	0.981(17)
$L\,[\mathrm{mH}]$	1.39(52)	1.48(14)	2.13(16)	2.04(15)	1.67(46)	1.97(12)
$\eta\,[\mathrm{G/A}]$	4.424(17)		3.277(13)		1.407(14)	

Table 3.2: Resistance, inductance and gain coefficient η of the compensation coils. The latter was measured for each pair in Helmholtz configuration. Data was measured by P. Arciszewski [76].

Sub-millisecond field off-switch

The Delta power supply used as a current source in MOT and FSH coils has an internal control circuit that is responsible for maintaining a constant current output set by the input voltage signal. We have observed that after changing the control signal between 0 and a constant value, it takes the power supply around 5 ms to reach the desired setpoint.

Although it may not seem a long period, it is in fact problematic considering the sensitivity of some experimental stages on the magnetic field. For example, as stated in Sect. 2.4, the gray-molasses cooling, directly succeeding the MOT stage, exhibits an efficiency dependence on the magnitude of magnetic induction. The decaying inhomogeneous field of MOT can *a priori* influence this stage if not extinguished sufficiently fast. Also, the leftover offset field after Feshbach spectroscopy measure-

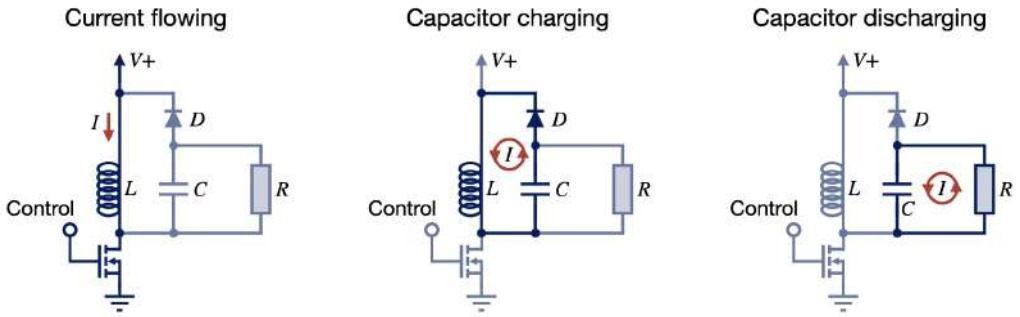

Figure 3.3: Schematic of the fast off-switch circuit in various stages of operation. Shaded elements are disabled at given stage. At first current flows freely through the coil L and the snubber is inactive. When MOSFET is closed energy flows from the coil to the capacitor C. After quarter of a cycle of the LC circuit, the diode closes current flow and energy is dissipated on the resistor R.

ment or gradient field after magnetic trapping may influence the imaging stage, as the Zeeman effect shifts the energy levels of atoms illuminated with resonant light.

For these reasons, we decided to implement a fast switching off of the magnetic field on both MOT and FSH coils. We utilized an already reported design [80], which is simple in implementation, yet quite effective, and provides switching off times of the order of tens of microseconds.

It is based on a polarized snubber circuit [81] that is shunting the coil and a high-power MOSFET[3], which acts as a fast controllable switch. The circuit schematic is shown in Fig. 3.3, where three operation stages are presented.

In standard operation, the current flows undisturbed through the coils, as a diode in the circuit acts as a polarizing element, and prevents the flow through the snubber. When we close the MOSFET, the coil reacts with the increase of the electromotive force, opposite to the supply, which in turn polarized the diode forward and effectively forms an LC circuit. The path through the resistor is less favorable due to the high resistance, in our case around 1 kΩ. The current at this stage follows the equation:

$$L\frac{\mathrm{d}^2}{\mathrm{d}t^2}I(t) = \frac{I(t)}{C} \tag{3.1}$$

which has a harmonic solution. This means that current oscillates and the energy stored in the magnetic field is transferred to the electric field of the charging capac-

[3]IXFN200N10P N-channel MOSFET by IXYS

itor. Assuming $I(0) = I_0$ and $\mathrm{d}I/\mathrm{d}t|_{t=0} = 0$ we get a solution:

$$I(t) = I_0 \cos\left(\frac{t}{\sqrt{LC}}\right) \tag{3.2}$$

which shows that after a quarter of the cycle the current changes direction as the energy is transferred from the capacitance back to the inductance. However, this is halted by the diode, which in this case is polarized reversely. We have observed that the current tends to overshoot a little, which is due to the finite diode response time. Then, in the last stage, the energy stored in the capacitor is therefore dissipated on the resistor, which is the only possible path, on the timescale given by:

$$\tau = RC \tag{3.3}$$

The current of the coils is therefore effectively redirected into the snubber in the quarter of the cycle of the LC circuit, or in other words, it stops on the first zero crossing of the oscillation. It is given by:

$$t_0 = \frac{\pi}{2}\sqrt{LC} \tag{3.4}$$

which does not depend on the initial current of the coil.

In our circuit, we used the $C = 4.540(58)\,\mu\mathrm{F}$ capacitor (nominally $C = 4.7\,\mu\mathrm{F}$), the $R = 0.9960(58)\,\mathrm{k}\Omega$ resistor (nominally $1\,\mathrm{k}\Omega$) and a fast-recovery rectifier diode[4].

We have measured the current flowing through the coils with a high accuracy current transducer IT-400 Ultrastab[5] and present the results in Fig. 3.4 for both coils and various initial currents. From the fit of the function given in Eq. 3.2 we obtained average switch off times weighted by the uncertainty, which are presented in Tab. 3.3. We also calculated the theoretical prediction with the equivalent inductance of coils connected in series with parameters as in Tab. 3.1. The resistance of the coils can be neglected in this case, we verified that including this in calculations does not change the outcome considerably.

We interpret the discrepancy between the theoretical and the measured values as coming from the mutual inductance of the coils which was not included in the previous discussion. For the Helmholtz (anti-Helmholtz) configuration, it would result in a greater (lower) equivalent inductance [82], and hence the switching time, as indicated by the relative error shown in Tab. 3.3.

[4]D42-70 rectifier diode

[5]High accuracy current transducer IT-400 Ultrastab by LEM

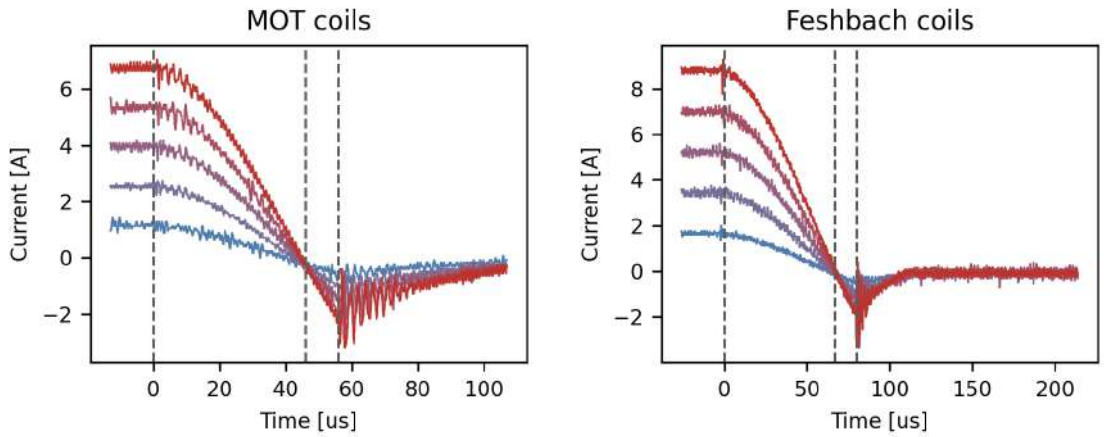

Figure 3.4: The current in MOT (left hand side) and FSH (right hand side) coils during the switching off procedure, measured with current transducer for various initial currents. The gray dashed lines mark the beginning of the switching, the zero crossing and the current overshoot due to finite diode response time. The plots show independence of the switching time on the initial current value.

Coils	t_0 **theory**	t_0 **measured**	**Relative error**
MOT	46.81(40) μs	43.93(54) μs	-6.2%
FSH	62.6(21) μs	64.37(53) μs	2.9%

Table 3.3: Theoretical and measured switch off times of the MOT and FSH coils. Uncertainties in theory come from the uncertainties of measured component values. The measured value is a weighted average of fit results for various initial currents (see Fig. 3.4).

The last aspect to be discussed is the damage threshold of the components used in the circuit. Let us focus on the electromotive force of the coils during the LC stage of the switching. It is given by:

$$\mathcal{E} = L\frac{\mathrm{d}I}{\mathrm{d}t} = I_0\sqrt{\frac{L}{C}}\sin\left(\frac{t}{\sqrt{LC}}\right) \tag{3.5}$$

which shows that the maximal value depends on both the initial current I_0 and the capacitance C (we assume that L is constant). The value $\mathcal{E}_{max} = I_0\sqrt{L/C}$ is reached at the quarter of the LC oscillation and corresponds to the voltage at the capacitor nodes at this moment. For high currents $\approx 70\,\mathrm{A}$, which we sometimes use to generate

fields of the order of 500 G for observation of Feshbach resonances, the voltage can reach ≈ 600 V.

Another parameter to take care of is the power rating of the resistor as it needs to dissipate the energy transferred to the capacitor. The peak power of the RC circuit in the last stage of the switching is given as:

$$P_{max} = \frac{I_0^2 L}{RC} \tag{3.6}$$

which for the values above reaches around ≈ 360 W. The resistor we put in the circuit has a rating of 50 W average power, yet it works flawlessly in the circuit for years now.

These restrictions should be taken into account when choosing components with appropriate voltage and power ratings. As is usually the case, *quid pro quo*, the reduction in the switch-off time comes at the cost of increasing other parameters of the circuit.

Laser systems

The light in our apparatus is provided by two laser systems, dedicated for cesium and potassium separately. Their purpose is to prepare light for MOT, fluorescence and absorption imaging, gray molasses cooling (GMC), hyperfine optical pumping, and Zeeman spin pumping. The optical setups are described in detail in the works of other group members - the cesium setup in K. Dinçer's PhD thesis [79] and the potassium setup in M. Bocheński's PhD thesis [83] and our publication [78]. In this section I will give a brief description of the system, regarding the subjects touched in this dissertation.

As a light source, we utilize external cavity diode lasers (ECDL) in the master oscillator power amplifier (MOPA) configuration from Toptica[6]. In the cesium system, there are two lasers operating at 852 nm (D_2 line of cesium) that couple two ground hyperfine states with the excited state. In the potassium setup we utilize two ECDLs as master lasers operating at 770 nm (D_1 line) and 767 nm (D_2 line).

Each of the ECDLs is locked to a specific atomic transition. For this, we utilize compact saturation spectroscopy modules[7] (CoSy), which provide the signal of the hyperfine transitions. The laser controller has an embedded lock-in module, which modulates the laser diode current, and demodulates the signal from CoSy, which results in obtaining an error signal for the lock. The lock frequencies of our lasers are shown in Fig. 3.5 together with the energy structure of ^{133}Cs and ^{39}K.

[6] TA Pro by Toptica

[7] Compact Saturation Spectroscopy (CoSy) module by Toptica

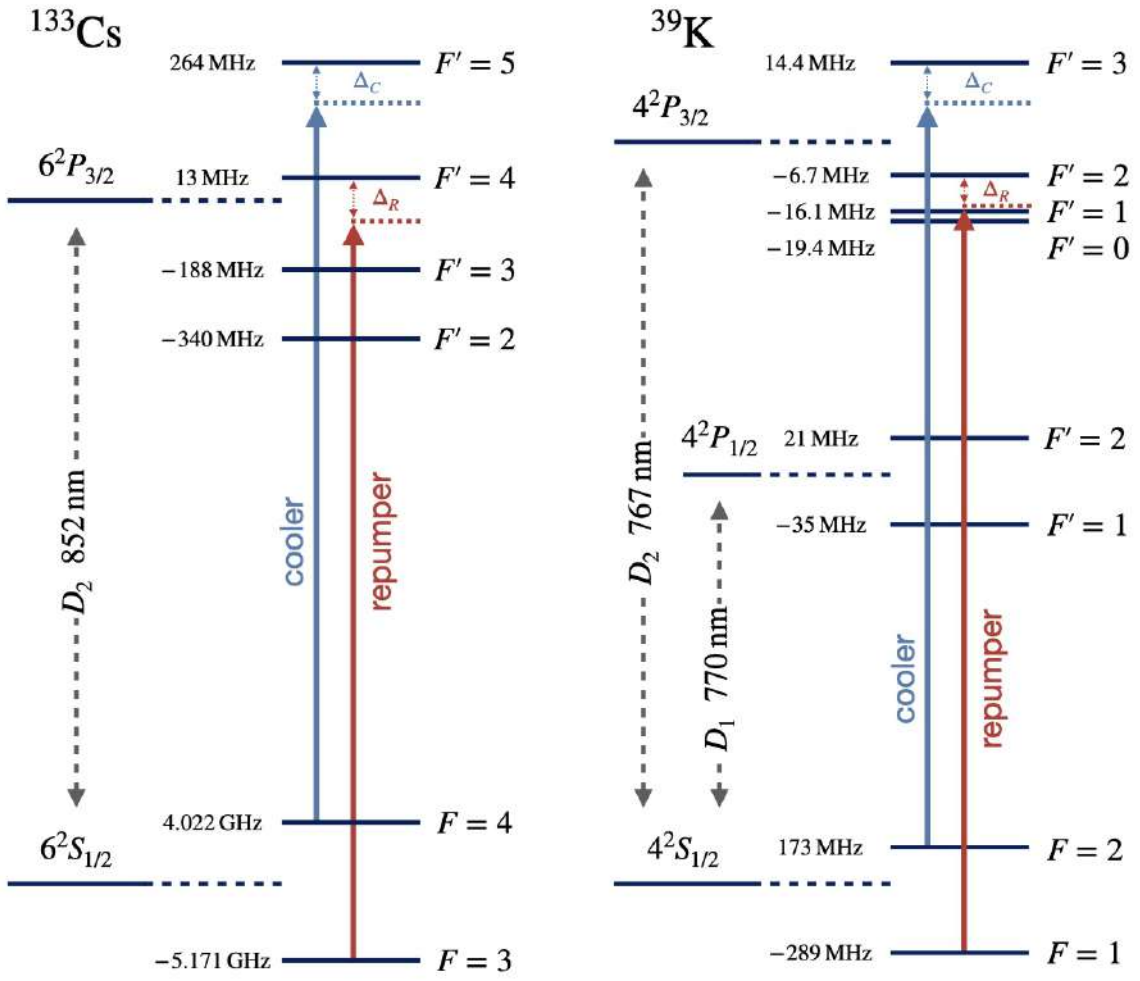

Figure 3.5: Diagrams of hyperfine structure of the ground and excited levels of ^{133}Cs [84] and ^{39}K [85] relevant to the present work. Cooler and repumper beams are marked together with detunings with respect to the transitions they drive.

Various stages of the experimental sequence require light with certain properties such as intensity, frequency, or polarization. For this reason, the beams from the lasers go through dedicated light distribution systems.

As it is often the case, we use acousto-optic modulators (AOM) in double-pass configuration to tune the light frequency and provide scanning capability. They are also used in single-pass configuration as fast switches because of their response time of the order of tens of nanoseconds. We drive AOMs using direct digital synthesizers

(DDS) and RF amplifiers and we observed that even when hypothetically turned off (amplitude setting equal to 0%), they still leak a little light. This causes unwanted optical pumping of the ultracold sample, so we use brute force and shut the power supply of the RF amplifiers with a MOSFET switch. To ensure that there is no leakage, we also added mechanical shutters, which are slower than AOMs, yet provide total blockage of the light.

In case of potassium light preparation, we utilize a versatile system built by M. Bocheński, which is capable of providing the required light of the D_1 and D_2 lines of all naturally abundant potassium isotopes (^{39}K, ^{40}K and ^{41}K). Its detailed description can be found in our publication [78].

The cesium light preparation setup is divided into two parts, one for the cooler light ($^2S_{1/2}\,F = 4 \rightarrow {}^2P_{3/2}\,F'$ transitions) and one for the repumper light ($^2S_{1/2}\,F = 3 \rightarrow {}^2P_{3/2}\,F'$ transitions). It is quite complex in a sense that to direct light onto certain paths and to obtain the desired light frequency we must choose proper settings of couple of AOMs. A single modulator frequency shift is not always sufficient due to large hyperfine splittings of the Cs excited state. The extensive description of the optical setup can be found in PhD thesis of K. Dinçer [79].

Offset locking of Cs lasers

Due to the large hyperfine splitting of the ground state of cesium (around 9.193 GHz which serves which serves for definition of the second in the SI sytem of units), we are forced to utilize separate lasers for generation of the cooling and repumping light. Although solutions based on single laser and EOM have been reported [86, 87, 88, 89], our apparatus is a general-purpose machine, where we would like to have spectrally pure light for various purposes. The utilization of EOM imprints the sidebands which are useful for the MOT stage, as they provide the repumping light, however, the leftover light is not always beneficial in other experimental sequence stages.

On the other hand, separate lasers operating independently do not provide phase coherence which is needed in some experimental techniques (see Sec. 2.4 and the Λ-enhanced GMC description). For this reason, we decided to upgrade our lock system and built an offset lock setup. This technique is based on the beatnote measurement between the lasers, which provides an RF signal with frequency equal to the frequency difference of the laser beams. We can lock one laser in reference to the other using a phase-locked loop (PLL)[90], however, in the case of cesium, this would require electronics operating at around 9 GHz. In our approach, we downgrade the beatnote frequency to a comfortable range of tens of megahertz using a frequency divider.

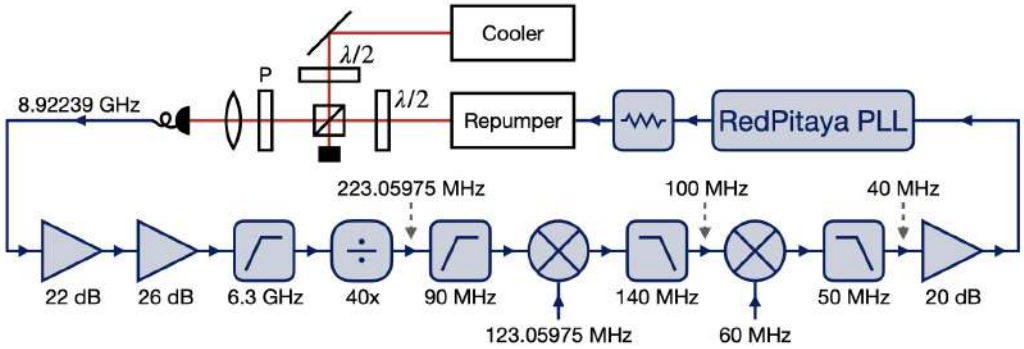

Figure 3.6: The scheme of optical PLL offset lock of our Cs lasers. The beatnote between the lasers is processed with a frequency divider and mixers to provide RF signal suitable for RedPitaya controller. This in turn, modulates the current of the repumper laser closing the OPLL loop. Gray dashed arrows indicate frequencies at the nodes of the loop. P stands for linear polarizer. The last mixer in the setup is utilized for introducing the offset frequency.

The scheme of the lock system is presented in Fig. 3.6. We measure the beatnote between the lasers on a high-bandwidth photodiode[8], and obtain $-64\,\mathrm{dBm}$ of RF signal. This is amplified[9] to $-15\,\mathrm{dBm}$, filtered, and divided[10] 40 times, so we obtain a signal around 220 MHz. This range is manageable with standard RF components and for further processing we use two mixers[11], filters, and an amplifier and finally arrive at 40MHz signal with $-1.5\,\mathrm{dBm}$ power and around 30 dB SNR, which are ideal parameters for acquiring the lock.

As the controller on the circuit we utilize RedPitaya[12], which is an embedded FPGA device with many available applications. We use an open-source PLL[13], which we also successfully implemented in other projects regarding the frequency stabilization.

Since the output of RedPitaya has ranges of $\pm 1\,\mathrm{V}$, and the laser diode current modulation input has ranges of $\pm 0.8\,\mathrm{V}$, we inserted a custom-made potentiometer voltage divider in between, which we use as a variable loop gain controller. This altogether closes the optical PLL, as the laser frequency is modulated accordingly to

[8] 818-BB-45 High Speed Photodetector by Newport
[9] We use two low-noise RF amplifiers from MiniCircuits: ZX60-05113LN+ and ZX60-183A-S+
[10] FPS-40-12 RF frequency divider by RFBay
[11] ZP-2+ double balanced mixer by MiniCircuits
[12] STEMLab 125-14, standard version
[13] Open source PLL firmware and software for RedPitaya by J. D. Deschênes

the current modulation input.

The incorporation of RF mixers in the loop provides a capability to change the laser frequency, by adjusting the frequency at the mixer input, which we call offset frequency. The lock frequency of the RedPitaya stays constant, however, the controller compensates for the change introduced in the offset. This technique is called offset lock, which, in a way, "deceives" the controller about the actual frequency of the laser, as the frequency change does not come from the laser drift, but it is modified arbitrarily by alteration of the offset frequency.

Due to the high division ratio present in the loop, the changes introduced by the offset are transferred to the optical domain with a magnification of 40 times. This means that to cover the entire hyperfine structure of the excited state of cesium (around 600 MHz span), we only need ± 7.5 MHz offset deviation. As long as the desired setpoint is reachable by the dynamic range of RedPitaya, we can easily adjust the laser frequency, controlling a single parameter, that is the offset frequency. This simplifies the laser setup so that we no longer need a complex system of AOMs.

We measured the beatnote spectra of the raw photodiode signal and the processed one at the input of the RedPitaya. The results for both locking scenarios, based on saturation spectroscopy and offset lock, are presented in Fig. 3.7. In case of OPLL, the offset frequency was chosen so that the laser frequency was the same in both cases, and we used a 50:50 power splitter to pick up the signal without interfering with the lock loop. Data was acquired on a spectrum analyzer with resolution bandwidth (RBW) set to 300 Hz. The plots allow us to compare the two cases.

The sidebands visible in the plots are coming from the saturation spectroscopy technique, as the laser diode current is modulated to obtain the error signal. It is still visible in the OPLL case, and what is more, the modulation of the reference laser (the cooler) is imprinted onto the locked one (the repumper). The spectrum at 40 MHz shows an acquired phase lock of the frequency with respect to the local oscillator (LO) provided by the internal RedPitaya clock.

On the other hand, on the spectrum at 9 GHz we do not observe spectrum narrowing as we would expect with phase lock. This is due to the large value of the division factor we use in the loop, which effectively reduces the bandwidth of the loop filter in the PLL [91, 92]. We have found that with our controller we are not able to compensate for this by increasing the loop gain, as doing so we also decrease the phase margin[14] and sacrifice loop stability.

Although in the end the lock did not allow us to have a phase-coherent cesium

[14]Phase margin is the difference between the phase shift induced by the control system and 180° at 0 dB gain. It is a measure of the stability of a feedback control system, as if it is lower than zero, the loop filter amplifies the control signal exponentially, which destabilizes the system.

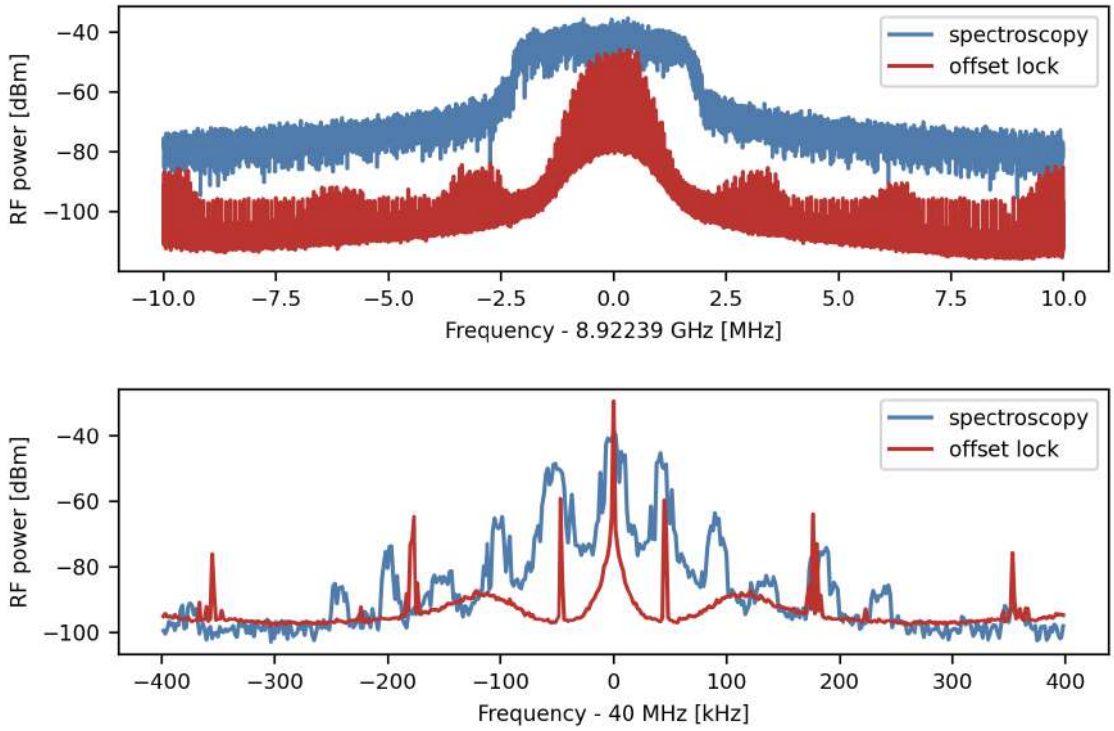

Figure 3.7: Beatnote spectra of the cesium lasers locked with the saturation spectroscopy technique (blue) and our implementation of OPLL (red). Upper panel shows the raw signal from the photodiode at around 9 GHz and the lower panel shows the signal processed in loop at 40 MHz.

laser system and to introduce the Λ-enhanced GMC, it is still a useful technique that will let us simplify the cesium part of the laser system. We have verified that the laser locked with this technique is also operational. Namely, we measured the cesium MOT loading curves for both cases, and the result with OPLL gave us a similar loading time with a little extra atoms in the steady state, as shown in Fig. 3.8.

Imaging setup

In this section, I will describe the methods for detection of the atomic sample that we implemented in the apparatus. The optical setups and light preparation are extensively described in the PhD thesis of K. Dinçer [79], so here I will focus only

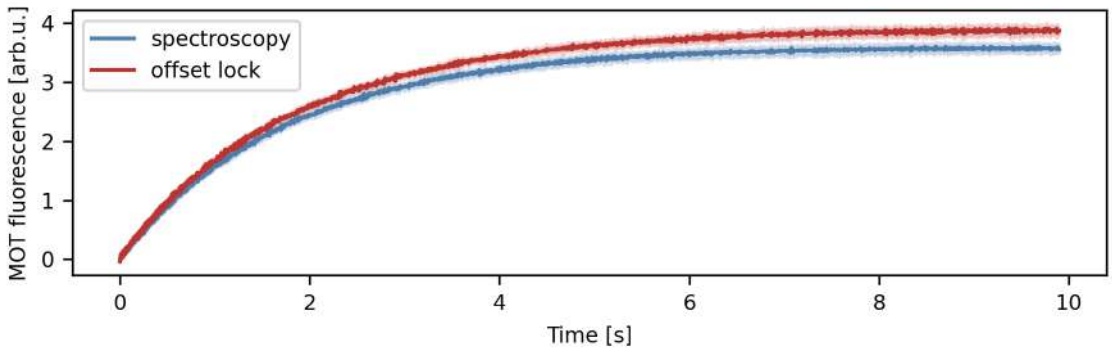

Figure 3.8: Fluorescence of the cesium MOT during loading time for two laser lock scenarios. Both cases yield similar results, with the OPLL slightly exceeding in terms of steady state atom number. Shaded area around the curves is the standard deviation calculated for 20 repetitions.

on aspects relevant to this dissertation.

In the apparatus, we have two imaging paths equipped with diffraction-limited optics, which provide us with the ability to observe the atomic sample in two directions, horizontal and vertical. They can also operate in two modes, fluorescence and absorption.

The horizontal path, shown in Fig. 3.9, consists of a self-made objective with $NA = 0.29$ and $1.8\,\mu$m resolution, a focusing lens, and a CMOS camera[15]. The field of view of this path contains the vertical direction, along the gravity, so that we can observe the atomic cloud *in situ* or after release from a trap. With our imaging setup, the atoms are visible for up to 20 ms of free fall, so that we can easily track the expansion of the atomic cloud and measure its temperature using the time-of-flight (TOF) technique.

We also placed a mirror on a flippable mount between the lens and camera, to redirect the gathered fluorescence light upon need. Then, it is split on a dichroic mirror with high reflectance at 767 nm and high transmission at 852 nm to distinguish between potassium and cesium samples, respectively. Each of the split paths has an additional focusing lens and a photodiode[16] with a large active area of $75.4\,\text{mm}^2$, which encompasses the field of view of the objective.

The vertical path consists of another self-made objective with $NA = 0.175$ and resolution $3\,\mu$m, followed by a dichroic mirror (the same as above) and two CMOS

[15]Grasshopper GS3-U3-41C6NIR-C by FLIR
[16]DET100A2 photodiode by Thorlabs

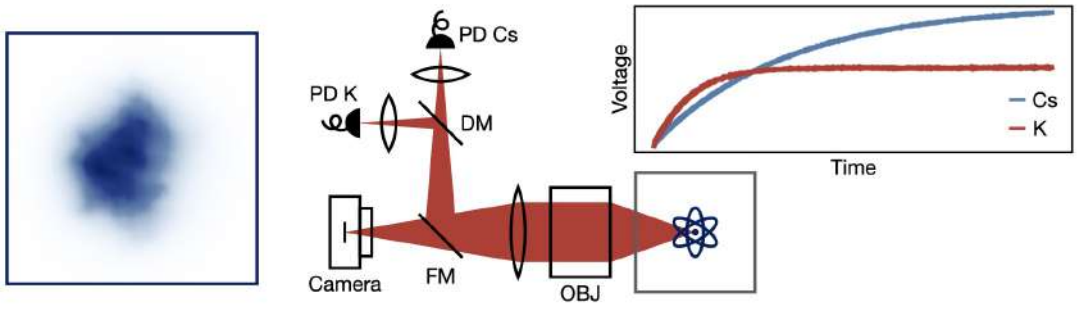

Figure 3.9: The horizontal path of the imaging setup. FM stands for a flippable mirror, and DM stands for a dichroic mirror. Insets show the *in situ* fluorescence photograph of the cesium MOT and simultaneous transient measurement of MOT loading of cesium and potassium 39.

cameras, to provide a distinctive 2D measurement of the cesium and potassium clouds.

Absorption imaging

The absorption imaging procedure starts with optical pumping of the atomic cloud to the higher hyperfine ground state, $F = 4$ for cesium and $F = 2$ for potassium. It is then illuminated with a short pulse of resonant light for around $20\,\mu$s. The absorption imaging beam has around 1 inch diameter, so it encompasses the entire atomic sample. This stage is performed without magnetic field, so that there are no Zeeman shifts present.

The imaging light comes from our light distribution setups, where in case of cesium, we prepare a beam resonant with the transition ${}^2S_{1/2}F = 4 \rightarrow {}^2P_{3/2}F' = 5$. In case of potassium, we theoretically use the transition ${}^2S_{1/2}F = 2 \rightarrow {}^2P_{3/2}F' = 3$, however, due to small hyperfine splitting of the excited state, compared to the natural linewidth, we should actually say ${}^2S_{1/2}F = 2 \rightarrow {}^2P_{3/2}F'$. More extensive discussion regarding this topic can be found in the PhD thesis of M. Bocheński [83], who built the potassium light distribution setup.

The atoms illuminated with resonant light absorb it, so on the camera we detect the imaging beam with an imprinted shadow. To extract the cloud image, we make an additional photograph of the solitary imaging beam, around 100 ms after the first. This lets all of the atoms to leave the field of view of the imaging setup. In addition, we also make a third photograph, when all of the light in the steup is turned off, to obtain the background image, which we subtract from the first two before further

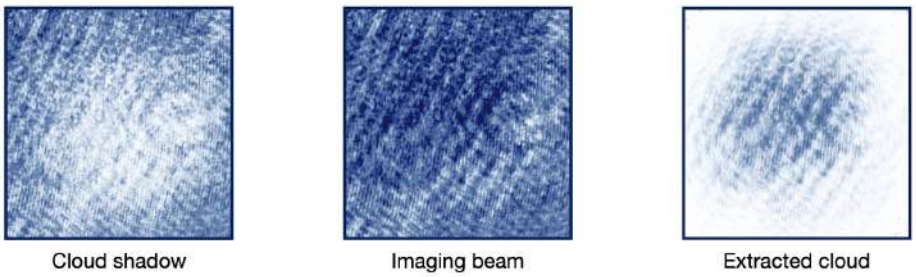

Figure 3.10: Consecutive steps of extracting the optical density of the atomic cloud from absorption imaging photographs. The visible interference patterns are due to multiple reflections of the optical surfaces such as walls of the glass cell or the protective window of the camera. They are not canceled fully in the last image due to mechanical instability of the apparatus.

calculation.

The optical density along the path of the imaging beam can be calculated from the Lambert-Beer law, which describes the intensity loss due to passage through an absorptive medium:

$$I(x,y) = I_0(x,y)e^{-OD(x,y)} \tag{3.7}$$

As the cameras detect the intensity of light, in our case I and I_0 correspond to the photographs with the atoms present and absent, respectively. The extraction of the image of the atomic cloud, shown in Fig. 3.10, is done in the data post-processing by calculating [38]:

$$OD(x,y) = -\log\left(\frac{I(x,y)}{I_0(x,y)}\right) \tag{3.8}$$

The advantage of absorption imaging is the ability to calculate the number of atoms in the sample. To do so, we use the formula $OD(x,y) = n(x,y)\sigma$, where n is the density of the atomic cloud and σ is the absorption cross-section. The latter depends on the atomic species and is given by the formula [84]:

$$\sigma = \frac{\sigma_0}{1 + 4(\Delta/\Gamma)^2 + I_0/I_{sat}} \tag{3.9}$$

where Δ is the detuning from the resonance, Γ is the natural decay rate of the excited state, I_{sat} is the saturation intensity, and σ_0 is the cross-section absorption in resonance $\sigma_0 = \hbar\omega\Gamma/(2I_{sat})$. As we use resonant light and have optimized the experimental sequence, these parameters are constant in our case. The number of

atoms can therefore be calculated by integrating the extracted optical density:

$$N = \frac{1}{\sigma} \int_{\mathbb{R}^2} OD(x, y) \mathrm{d}x \mathrm{d}y \tag{3.10}$$

The photographs taken by CMOS cameras are, of course, digitized, so in reality we calculate the sum of pixels instead of the integral. Also, to reduce the computational cost of the summing, we perform it in a chosen region of interest (ROI), as the atomic sample image rarely occupies the entire area of the camera matrix.

Absorption imaging has yet another advantage of being state-selective. As already mentioned, we optically pump the atoms prior to imaging to a proper state, which is coupled by the imaging light. However, the lower component of the ground state does not interact due to high hyperfine splitting of the ground state, much larger than the natural linewidth. By enabling and disabling the optical pumping stage, we can deduce whether the atomic sample is in the lower or higher component of the ground state.

The main disadvantage of this technique is due to the saturation threshold of the camera. For dense samples, we would need to increase the intensity of the imaging beam so that all of the atoms are detected. In a sense, in the cloud shadow area, some residual imaging light intensity should always be visible. However, it cannot be risen arbitrarily, as at some point we saturate the camera, even on the lowest exposure setting. To avoid this obstacle, we allow the atoms to fall freely for around 8 ms, so that the cloud expands and decreases its density. Then, the measurement of the number of atoms yields a valid result, at the cost of not being taken *in situ*.

Fluorescence imaging

The second mode in which we detect the atomic sample is based on the fluorescence phenomenon. In this case, we gather the light emitted by the atomic sample, which is illuminated with an almost resonant light. This technique is based on a cycling or, in case of alkalies, a quasi-cycling transition, which provides a continuous emission of photons. In our case, we utilize the same laser beams scheme as in MOT. Exemplary fluorescence images, coming from Cs MOT optimization sequence for various cooler detunings, are shown in Fig. 3.11.

The main advantage of fluorescence imaging is the increased SNR in comparison to the absorption imaging, as we only observe a few percent of the scattered photons (we estimated it to be around 3% in our setup). We can also adjust the exposure time to maximize the total count number. This allows us to detect even dense samples and determine the cloud size *in situ*.

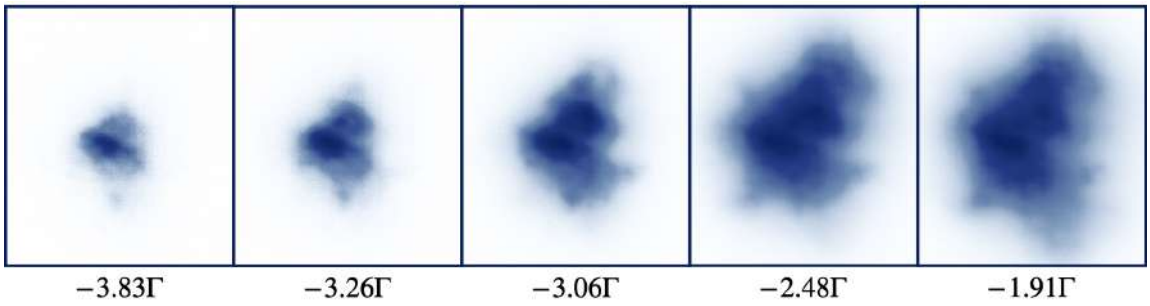

Figure 3.11: Fluorescence images of cesium MOT for various cooler detunings.

In addition, the interference pattern, as shown in Fig. 3.10 does not occur since the gathered photons come from spontaneous emission and thus are polarized randomly.

The fluorescence imaging can also be used to determine the number of atoms, this however requires knowledge of the scattering rate, quantum efficiency of the camera, exposure time, and the solid angle at which the fluorescence is gathered by the imaging system. As we already have implemented absorption imaging, which also provides this information, we instead calibrate the fluorescence imaging at given parameters.

Concerning disadvantages of this technique, it requires longer exposure timescales, around $1-2\,\mathrm{ms}$. In case of TOF measurement, this means that the photons detected come from various moments of the free fall, so the size of the cloud cannot be determined correctly. In addition, the imaging beams, similarly to optical molasses, exert a velocity-dependent force on the atoms, which can also distort the cloud shape.

Fluorescence-based detection is also used in the photodiode path of the horizontal imaging setup (see Fig. 3.9. We use it to track the fluorescence level of the MOT, which naturally emits light as a result of the cooling process. The photodiodes do not provide information about the spatial distribution of the cloud, however, they can detect the transient characteristics of the MOT, which is particularly useful when measuring the loading curve of the MOT. Another example is the photoassociation loss spectroscopy, where by correlating the scanned variable with the photodiode output we can obtain a photoassociative spectrum in a single scan of a laser, instead of multiple iterations for every laser frequency.

Photodiode detection can also be used to determine the number of atoms in the sample. For this purpose, we calibrated our setup based on a comparison with the absorption imaging outcome. We varied the gradient of the magnetic field in MOT to obtain clouds with different steady state atom numbers and detected them with

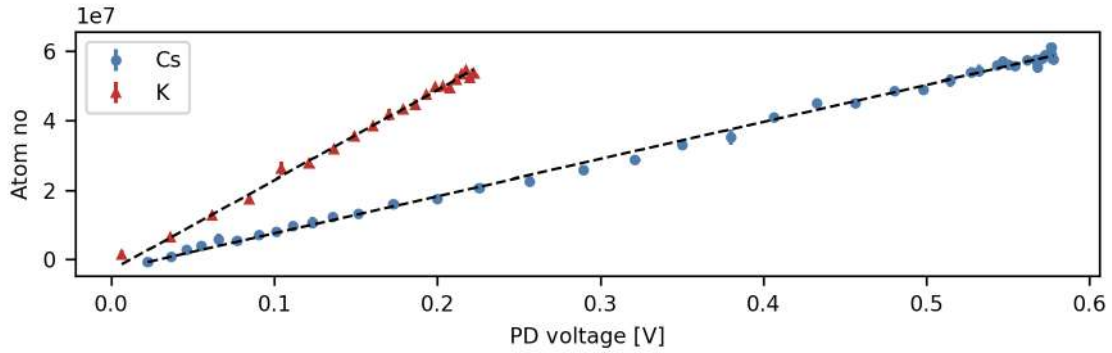

Figure 3.12: Calibration of the photodiodes for measurement of MOT fluorescence, based on atom number derived from absorption imaging. Data was obtained by varying the magnetic field gradient of the MOT.

both methods. The obtained calibration curve is shown in Fig. 3.12.

3.2 Light induced atomic desorption

In a single-cell setup, like ours, the vapor pressure must be high enough so that there is a decent population of atoms with a velocity below the capture velocity v_c, which can be trapped in the MOT. On the other hand, as stated in Sect. 2.3, higher background pressure decreases the lifetime of the dipole trap, by increasing the one-body losses.

As the stages of the MOT and dipole trap are separated, we could in principle introduce temporal variation of the background gas, for example, by switching off the atomic source after the MOT stage. We tested this solution, however in our setup the atoms come from heated dispensers which are placed in the vacuum. This means that after the current flow is disabled, they are still hot enough to emit atoms, and their cooling is limited mostly to the radiative heat transfer.

For this reason, we implemented a method for rapid alteration of the loading rate, called light induced atomic desorption (LIAD) [93]. It is based on the observation that some of the atoms emitted from the atomic source stick to the walls of the glass cell. They can be "recycled" back to the cell volume, if illuminated with high-energy UV light coming, for example, from an LED. In this section, we will briefly describe a model that lies behind this phenomenon and present our implementation of the method.

Adsorption and desorption model

The equilibrium between the atoms in the background vapor and the ones adsorbed on the walls of the glass cell can be modeled with the rate equation [94]:

$$\dot{N}_v = k_d N_s - k_a N_v \tag{3.11}$$

where N_s is the number of atoms adsorbed on the glass cell surface, N_v is the number of atoms in the background vapor, and k_a and k_d are the adsorption and desorption coefficients, respectively. The coefficient k_d is proportional to the Boltzmann probability given by the adsorption energy and thus depends on the temperature of the cell surface. The coefficient k_a is given by the probability of adsorption, the flux of thermal atoms, and the cell surface. Therefore, k_d and k_a are characteristic for a certain experimental setup. In particular, atoms can bond not only to the surface of the cell but also to defects in the glass that come from the manufacturing process. In the literature, it has been suggested that the major LIAD contribution comes from the desorption from the defect sites because they bond the atoms more strongly than the plane surface [95].

Solving the Eq. 3.11 in the steady state and expressing it by the total number of atoms present in the cell, both in vapor and on the walls, yields:

$$N_v = N_t \frac{1}{1 + \frac{k_a}{k_d}} \tag{3.12}$$

where $N_t = N_v + N_s$. Based on the assumption of equilibrium between the emission of new atoms by the dispensers and the depletion of the background gas by the vacuum system pumps, we claim that N_t is constant.

After the cell surfaces are enlightened with UV light, a new equilibrium is established as an additional desorption phenomenon occurs. Eq. 3.11 needs to be modified with an additional term kIN_s, where k is a constant proportional to the LIAD cross section and I is the current of the UV LEDs proportional to the consumed power and thus the intensity of the emitted light. As stated in Sect. 2.3, since the loading rate of the MOT is proportional to the vapor pressure and, therefore, the number of atoms in the vacuum cell, we can directly write a proportion for the MOT loading rate R:

$$R(I) \propto \frac{1 + \frac{k}{k_d} I}{1 + \frac{k_a}{k_d} + \frac{k}{k_d} I} \tag{3.13}$$

This relation does not include the transient characteristic of the LIAD, because the model is based on the assumption of constant N_t. If we assume constant pressure

in the pumps section of the experimental apparatus, then, when the desorbed atoms increase the vapor pressure in the experimental cell, they are pumped out because of a higher pressure difference between the sections. For this reason, when UV light is turned on, after an increased burst, the number of captured atoms slowly returns to the LIAD-off value due to N_t depletion. However, this effect is slow enough to successfully utilize LIAD as an enhancement of the MOT loading rate.

In the experiment, we use the LIAD for a few seconds during the MOT loading stage, taken into consideration two factors. Firstly, increased vapor pressure leads to a higher collision rate with the background gas, thus decreasing the lifetime of other traps used further in the experiment. Secondly, out of foresight we did not want to illuminate our experimental cell with UV light for extended periods of time because it is made of rectangular glass pieces glued together. As we do not have information about the glue used, we decided to avoid possible deterioration due to UV illumination.

LIAD implementation

We implemented the LIAD in our setup with a power UV LED[17] with nominal wavelength of 370 nm and maximal optical power 930 mW. They dissipate a significant amount of heat, so we decided to solder them onto a dedicated printed circuit board (PCB) radiator made of aluminum. As we turn them on for only a few seconds, this solution provided enough heat dissipation so that the diodes do not overheat.

We placed the diodes in a 3D printed casing with a hole in the front wall, which acts as an aperture for the emitted UV light. This in turn was positioned on an adjustable post and directed onto the experimental glass cell, through the hole in the MOT and FSH coils mount. In this way, we illuminate the volume of the trap and also reach the neck of the glass cell, where the dispensers are installed, and the atomic flux is the highest.

To validate the operation of the LIAD we measured the Cs MOT loading curves, with our photodiode setup, for various LED currents provided by a programmable power supply. The MOT loading procedure was as follows, for 10 s we loaded the trap without LIAD, then the UV light was turned on and the loading continued for another 10 s. We fitted the MOT loading equation in the high-density regime (see Eq. 2.15) to the obtained data, separately for the two stages, with and without LIAD.

The fitting of the direct solution (see Eq. 2.16) returns correlated parameters N_∞ and γ, so we decided to follow a different approach and propagate the equation

[17] PB2D-3JLA-GS UV power LED by PROLIGHT OPTO

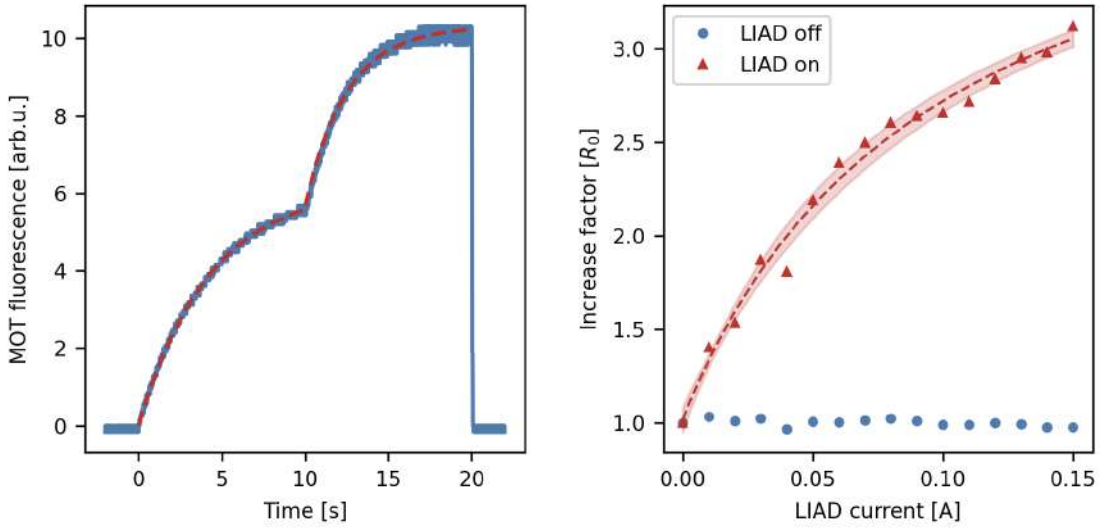

Figure 3.13: Left hand side: an exemplary measurement of the MOT loading curve with LIAD turned off (first 10 s) and on (following 10 s) with fitted loading curves. Right hand side: relative increase factor of the loading rate for various UV LED currents. The dashed red line is the fit of the adsorption-desorption model. Shaded area shows the uncertainty of the fit.

numerically. For this purpose, we utilize a self-written implementation of Dormand-Prince algorithm, coming from the family of Runge-Kutta algorithms (often denoted as RK45). Its detailed description can be found in App. A.

The numerical propagation of the equation has the advantage of using the physically significant parameter, which appears in the derived theory, namely the loading rate R. In case of analytical solution, it is implicitly given by N_∞ and γ. In addition, since the RK45 algorithm has the advantage of setting the error tolerances, we chose them to be much smaller than the systematic error, so that the numerical uncertainty does not dominate.

An exemplary curve and measurement results for various LED currents are shown in Fig. 3.13. To the extracted loading rates, we fitted the relation 3.13, which returned the adsorption and desorption ratios $k_a/k_d = 44.4(84)$ and $k/k_d = 3.29(27)$. Given the fitted parameters, the relative factor of the increase in the loading rate, defined as $\eta(I) = R(I)/R(I = 0)$ saturates for high currents with around 4.36 value.

We can drive the diodes with a nominal maximum current of 700 mA, which would result in an increase factor of 3.96. We decided to lower the current to 300 mA

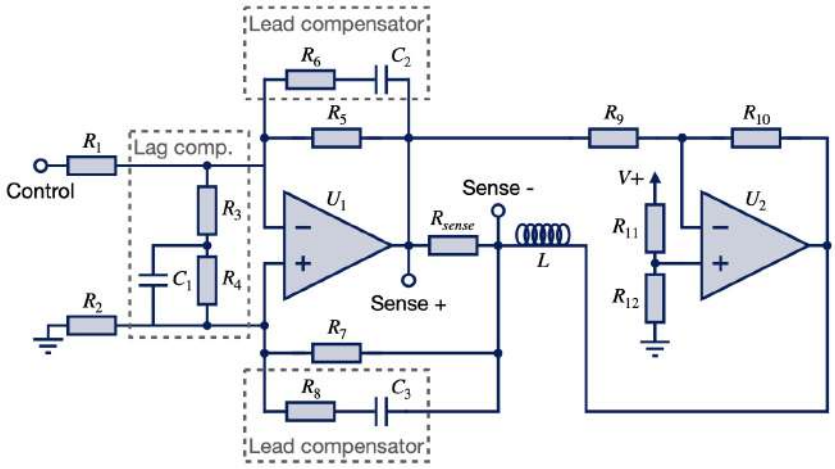

Figure 3.14: Electronic scheme of the current source subcircuit consisting of two high power operational amplifiers in a push-pull configuration. Lead and lag compensator sections are highlighted. The values and models of the components are presented in Tab. 3.4.

to avoid excessive heating and extend the lifetime of the LEDs. At such conditions, the loading rate for the MOT is enhanced by a factor of 3.55.

3.3 Compensation coils current driver

The magnetic field, as already stated in several sections, is a backbone of the ultracold experiments that enables trapping of the atoms [38], defining a quantization axis for the spin states, or control of the interatomic interaction via the Feshbach resonances [20]. In each of these examples, the crucial aspect is the ability to create a stable magnetic field, since its fluctuations can influence the phenomenon under investigation. It directly translates to the stability of a current source, as the magnetic fields are almost exclusively generated with pairs of properly arranged coils.

In this section, I will describe the design and validation of a bidirectional current source that I developed to control the magnetic field generated by the compensation coils in our apparatus. I will discuss the electronic circuit and follow with the noise spectrum tests. In the end, I will present our optimization for canceling of the stray magnetic field inferred from the temperature measurements in GMC of potassium 39. This discussion can also be found in our publication [96].

Component	Model/value	Symbol
Operational amplifier	OPA549T	U_1, U_2
Resistor	100 kΩ	R_1, R_2
	22 kΩ	R_3
	2 MΩ	R_4
	20 kΩ	R_5, R_7
	2 kΩ	R_6, R_8, R_9, R_{10}
	10 kΩ	R_{11}, R_{12}
	0.1 Ω	R_{sense}
Capacitor	220 pF	C_1
	100 pF	C_2, C_3
Inductor	L_x, L_y, L_z	L

Table 3.4: Values and models of the electronic components used in the current source subcircuit. Symbols are corresponding to the ones in Fig. 3.14.

Current driver circuit

Out of several commonly used circuits for bipolar current sources, we chose a setup of two high-current operational amplifiers connected in a push-pull configuration. Other circuit schemes, such as Howland pump, current-in/current-out amplifiers, or push-pull setup but based on transistors, either do not provide the high-current requirement or exhibit a nonlinear zero crossing when changing the sign of the current [97, 98, 99, 100]. Our approach is a modified version of a design developed by Nicolas Arango and Irene Kuang [101].

The current driver consists of two major subcircuits, the current source and the PID controller. We will begin with the description of the first. The electronic schematic is presented in Fig. 3.14, with Tab. 3.4 supplying the values and models of the components.

The current in the circuit flows between the outputs of the two operational amplifiers[18], through a high-power current sense resistor $R_{sense} = 0.1\,\Omega$ and a pair of compensation coils, connected in series (see Tab. 3.2). One of the amplifiers acts as a current source and pushes the current through the load, whereas the other acts as a current sink and pulls it, hence the name push-pull configuration. An advantage of this circuit is that both amplifiers have a single-sided supply, so only one power supply channel is needed. The DC transconductance of the circuit, under ideal amplifier assumption and balanced resistances in the inverting and non-inverting branches, is

[18]OPA549 high-current operational amplifier by Texas Instruments

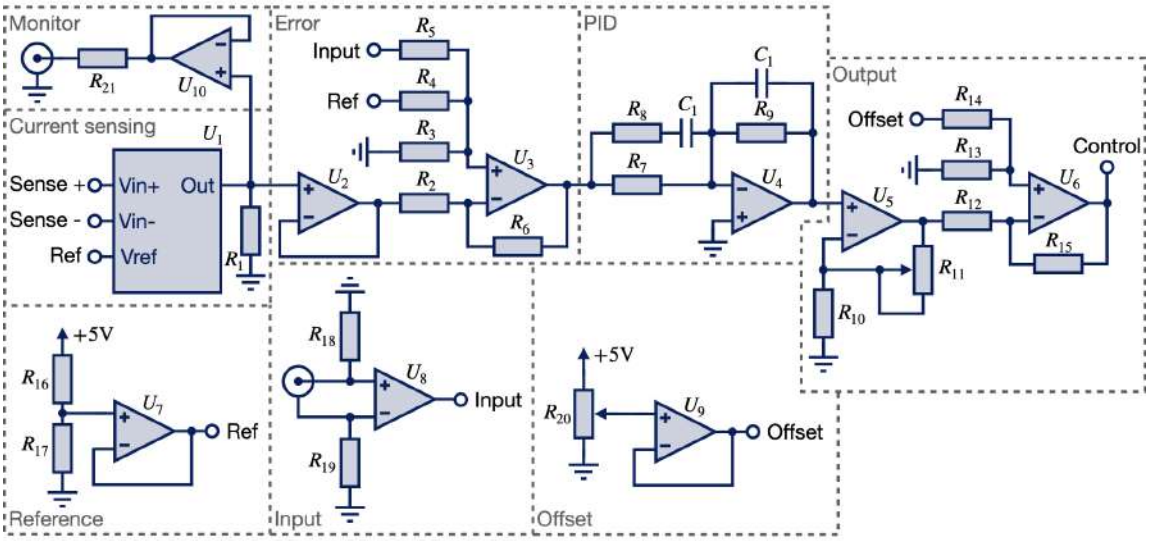

Figure 3.15: Electronic scheme of the PID controller subcircuit with highlighted sections. The values and models of the components are presented in Tab. 3.5.

given by:

$$I_{sense} = \frac{R_5}{R_1}\frac{U_{control}}{R_{sense}} \tag{3.14}$$

where we the notation is the same as in Fig. 3.14. In our circuit, the gain is equal to 2 A/V.

The coil in the load introduces an inductance in the loop, which results in a delay in the system response and a decrease of the phase margin due to a phase shift. To enhance the timing characteristic, we introduced lead and lag compensators [102], marked in Fig. 3.14. They do not change the DC gain of the circuit but introduce poles and zeros that shape the open-loop transmittance. That is, the lead compensator adds a zero below and a pole above the crossover frequency, which increases the phase margin of the loop. This in turn reduces overshoot and ringing of the system. The lag compensator decreases the high-frequency gain, which results in reduction of the noise in the steady state.

The PID controller subcircuit, shown in Fig. 3.15, consists of several parts, each of which is marked in the figure. The feedback loop begins with current measurement

Component	**Model/value**	**Symbol**
Current sense amplifier	INA170	U_1
Operational amplifier	OP07	U_2, U_5, U_6, U_7, U_8, U_9, U_{10}
	OPA2227	U_3, U_4
Instrumentation amplifier	AD8421	U_{10}
Resistor	2.5 kΩ	R_1
	10 kΩ	R_2, R_3, R_6, R_{10}, R_{12}, R_{13}, R_{14}, R_{15}, R_{16}, R_{17}
	20 kΩ	R_4, R_5
	100 kΩ	R_{18}, R_{19}
	R_{P1}	R_7
	R_{P2}	R_9
	R_D	R_8
Potentiometer	20 kΩ	R_{11}, R_{21}
Capacitor	C_D	C_1
	C_I	C_2

Table 3.5: Values and models of the electronic components used in the PID controller subcircuit. Symbols are corresponding to the ones in Fig. 3.15. Values of R_{P1}, R_{P2}, C_I, R_D, and C_D are not given explicitly because they are used to shape the transmittance of the circuit and are chosen for a specific application.

performed by a bidirectional current shunt monitor[19], which measures the current flowing through the resistor R_{sense}. We chose this particular model because of the high common-mode rejection, high input voltages, and a low output noise density of $20\,\mathrm{pA}/\sqrt{\mathrm{Hz}}$. Its voltage output is split into two paths, the monitor output for diagnostics and the error section.

The error signal is calculated by comparing the current-related signal obtained with an analog setpoint voltage, fed into the circuit with an instrumentation amplifier[20], to ensure isolation between the board and the environment. The error signal is processed by a PID section, where we designed the three-term controller on a single operational amplifier to reduce the space that it takes on the PCB board. The transmittance of the PID section can be shaped with components labeled in Tab. 3.5 as R_{P1} and R_{P2}, which shape the proportional gain, C_I which corresponds to the integral crossover frequency, and R_D and C_D which shape the differential part

[19]INA170 bidirectional current sense amplifier by Texas Instruments
[20]AD8421 low noise instrumentation amplifier by Analog Devices

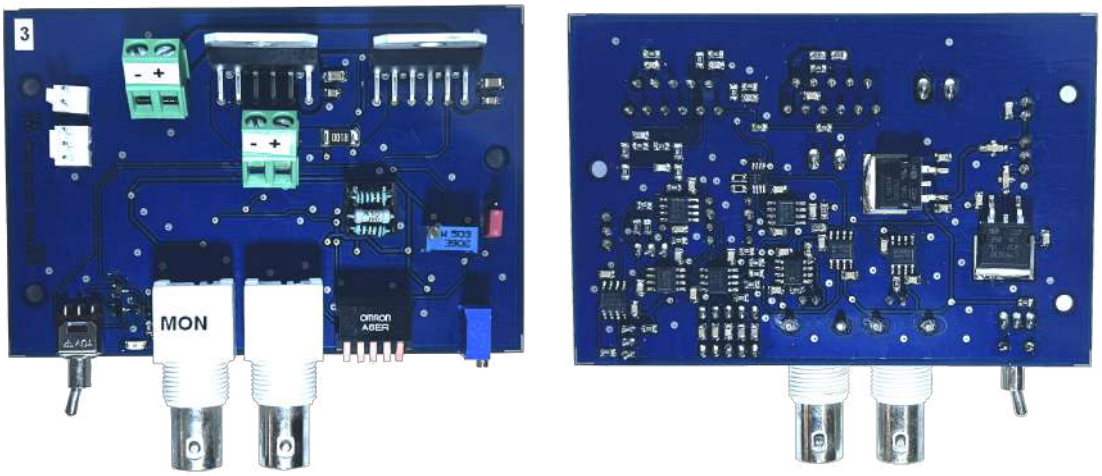

Figure 3.16: Photographs of an assembled current driver. Left hand side: top side. The DIP socket visible is used to insert the R_{P1}, R_{P2}, R_D, and C_D components for the P and D transmittance shaping. The piano switch at the bottom edge is used to set the C_I. Note that the power amplifiers are placed near the top edge to account for the space needed by a radiator. Right hand side: bottom side.

of the controller. We also added an additional stage for the total gain adjustment and an offset section, which lets the operator compensate for the output offset due to parasitic impedance and dark currents present in the circuit. The output of the controller is then fed to the push-pull section described previously, which closes the feedback loop.

Circuit characterization

To characterize the performance of the driver we measured the linear spectral density (LSD) which is derived from a fast Fourier transform (FFT) of a long-run signal. The driver was connected to the pair of our compensation coils with the highest equivalent inductance (coils no. 3 & 4) and the current was measured from the monitor output of the driver.

For sufficient resolution we used a 12-bit oscilloscope[21] with 2.5 MHz sampling rate. We acquired 10 s long, continuous traces for the noise floor and currents 152 mA and 4 A. From the data we derived the LSD which yielded the noise level of the order of $\mu\mathrm{A}/\sqrt{\mathrm{Hz}}$ and 45 ppm of integrated noise over 1 MHz bandwidth for 4 A driver

[21] HDO 4054 by Teledyne LeCroy

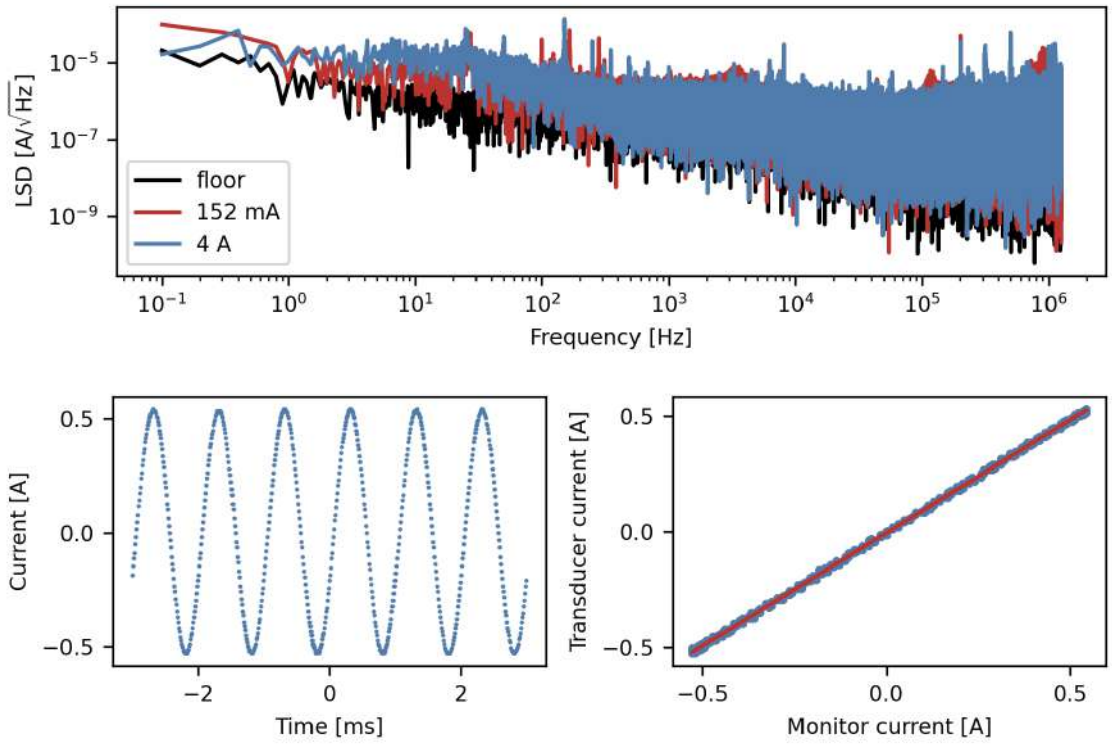

Figure 3.17: Top panel: linear spectral density of the noise for different driver currents. Integrated noise for the 4 A is 45 ppm. Bottom panel: Validation of the monitor output of the driver. The setpoint was fed with a 1 kHz sinusoidal function corresponding to ±0.5 A deviation. Left hand side: monitor signal translated to current units. Right hand side: correlation plot between transducer and monitor outputs, translated to current units. Linear fit yields 97.5% of correlation factor.

current. The results are shown in Fig. 3.17.

We also measured the current independently, using a high-accuracy current transducer[22], which let us verify the consistency of the monitor output reading. For this purpose we compared two traces when the driver setpoint was fed with a 1 kHz sinusoidal input which corresponded to ±0.5 A deviation. The results are presented in Fig. 3.17.

[22]High accuracy current transducer IT-400 Ultrastab by LEM

Stray field cancellation with sub-Doppler cooling

After electronic validation of the driver we implemented three boards in our apparatus to control all three pairs of the compensation coils. We decided to perform yet another validation with the cold sample. As already discussed, the presence of an uncompensated magnetic field can influence certain cooling methods, such as gray molasses cooling [63, 59]. We decided to exploit this fact and compensate for the stray magnetic field present in the experimental chamber using our newly installed current drivers.

Measurements presented herein were performed using the GMC cooling on D_1 line in potassium 39, which was prepared by M. Bocheński. Detailed description of the cooling method can be found in his PhD thesis [83].

In several papers it was reported that the temperature of the atomic sample cooled with the GMC method depends on the magnetic field quadratically and has minimum when the net field is 0. Including the stray field vector $\vec{B}_{stray}$ we get a phenomenological formula:

$$T(B) = T_{min} + \alpha|\vec{B}_{stray} - \vec{B}|^2 \tag{3.15}$$

With our drivers, running at maximum current 4 A, we are able to generate uniform field in any arbitrary direction, with magnitude up to around 5.5 G along z axis, and around 13 G in x and y axes (see Tab. 3.2). It is perfectly sufficient to cancel the Earth's magnetic field of around 0.5 G, which is the main contribution to the stray field.

The temperature measurement in our apparatus is performed using the time-of-flight (TOF) method, in which the atomic cloud is released from the trap and measured on a camera after a certain fall interval t_{TOF}. As the cloud falls freely, it expands ballistically with a rate dependent on its temperature, according to the formula:

$$\sigma(t_{TOF}) = \sqrt{\sigma_0^2 + \frac{k_B T}{m} t_{TOF}^2} \tag{3.16}$$

where σ is the width of the cloud and m is the mass on the atom. The temperature can be extracted by a fit to the cloud widths measured for several fall times. Such measurements, combined with scanning of yet another parameter, extend the time required to perform the full experiment. For this reason, we used the width of the cloud around 8 ms after release from the trap as a proxy for the cloud temperature, which significantly reduced the duration of the measurement.

We divided the experimental procedure into two parts. Firstly, we set the compensation field magnitude to constant 0.42 G and varied the ϑ and φ angles of the

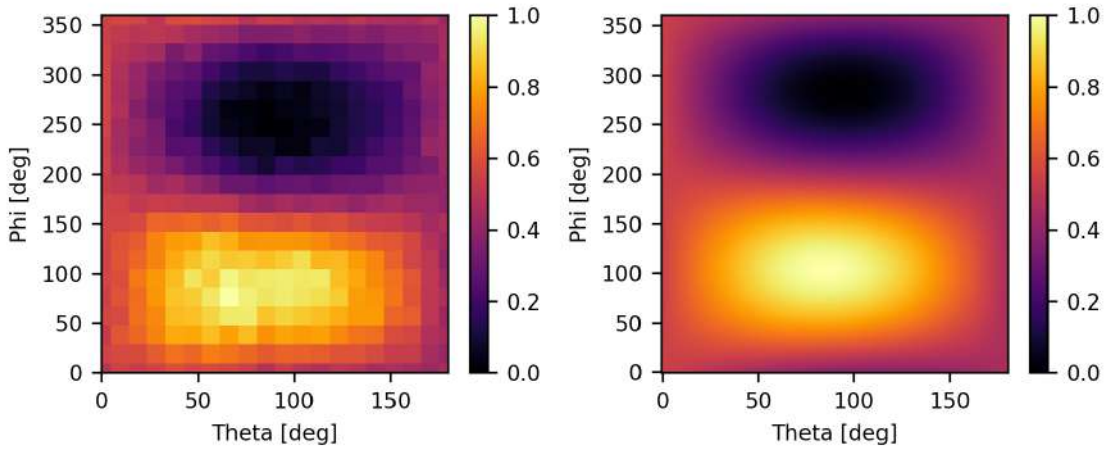

Figure 3.18: Normalized cloud width after 8 ms free fall for various tilt angles of the applied magnetic field. Darker (brighter) regions correspond to lower (higher) temperature of the atomic sample. Left hand side: results of the measurement. Right hand side: simulation based on Eq. 3.15 for the same conditions as obtained in the measurement.

field vector, defined in a spherical set of coordinates centered on the atomic sample. We measured the width of the cloud after 8 ms free fall, following the GMC stage, for each combination (ϑ, φ), which provided us with an angular map of the temperature estimation. This let us to identify the direction of the stray magnetic field. Note that for each fixed pair of angles, the atoms are influenced by a different magnetic field, given by a vector sum of the stray field, and the one generated by compensation coils. In case of angles, for which the cloud size is the smallest, and its temperature is therefore the lowest, the applied field is anti-aligned with the stray field, effectively compensating for it. The results obtained, together with a simulation based on Eq. 3.15 are presented in Fig. 3.18.

Then, we proceeded with a scan of the magnitude of the field, along the approximated stray field direction, but with opposite sign, and similarly relied on the cloud with measurement after 8 ms expansion interval. The proposed quadratic model is in accordance with the data obtained, presented in Fig. 3.19. We also measured the temperature using the TOF method for 5 values of the net magnetic field, to verify that our estimation by long fall time is valid.

To estimate the stray field even better, we followed with a second iteration of similar measurements, this time with angles distributed in the range of $\pm 20^\circ$ around

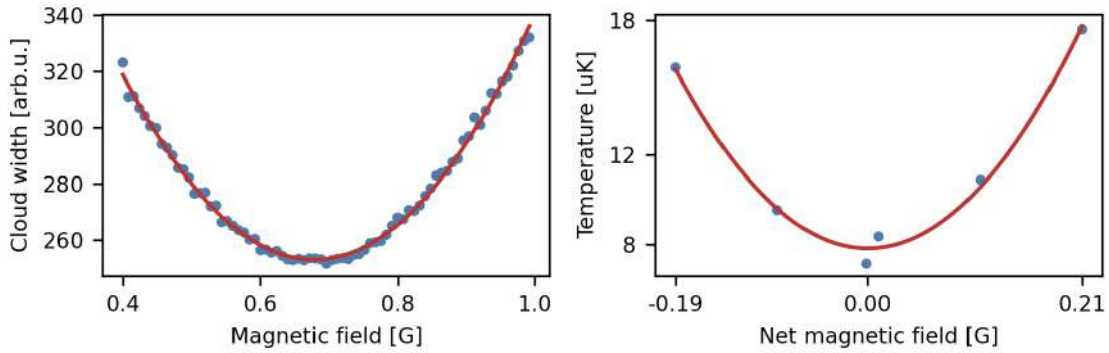

Figure 3.19: Left hand side: cloud width after 8 ms free fall for various magnitudes of the *applied* magnetic field directed opposite to the estimated stray field vector. The fit is the quadratic function with minimum at around 0.7 G. Right hand side: Temperature of the atomic cloud after GMC for various *net* magnetic field.

the ones already obtained. This denser measurement gave us an estimate of the direction of the compensation field to be $\vartheta_{min} = 92(2)^\circ$ and $\varphi_{min} = 256(2)^\circ$ defined in the set of coordinates that we adopted in the apparatus.

We again scanned the magnitude and observed that around 0 G of the net magnetic field the sample becomes less sensitive due to the flat derivative. We extended the duration of GMC cooling to 1 s to increase the interaction time and improve the quality of measurement. With such long times we still observe the influence of the uncompensated magnetic field, however, the atomic dynamics over such long period of time is non-trivial and the cloud becomes distorted. This makes the width of the cloud a non-reliable estimate of the temperature and limits our method of determining the stray field direction and magnitude.

We estimated, based on the fits in Fig. 3.19, that the parameter that describes the dependence of the temperature on the magnetic field in our case is equal to $\alpha = 225(10)\,\mu\mathrm{K/G}^2$, the result comparable with the observations of Salomon et al. [59], who obtained $\alpha = 300(100)\,\mu\mathrm{K/G}^2$. In addition, the minimal temperature reached with the stray field compensated is a state-of-the-art result. Without compensation, we obtained a temperature around 70 μK, which, after optimization, we reduced almost ten times to 8 μK. This result is also comparable with other groups: 6 μK by Salomon et al. [59] and 12 μK by Nath et al. [103].

With the stray field compensated, we optimized the two-photon resonance condition in the GMC procedure, and compared it with results without compensation. According to the theory, the Raman condition is fulfilled when the frequency differ-

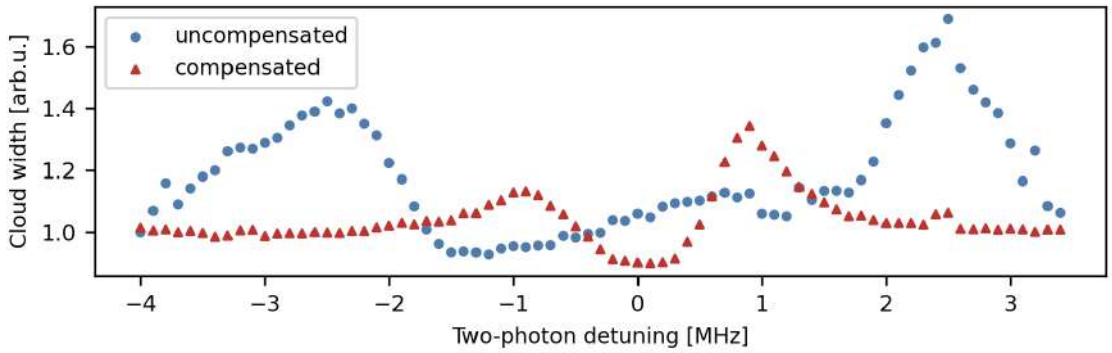

Figure 3.20: Cloud width normalized to the off-resonance value (at −4 MHz) for various cooler detunings from the Raman condition in the gray molasses cooling. Blue circles (red triangles) correspond to the uncompensated (compensated) case.

ence between the cooling and repumping beams is equal to the hyperfine splitting of the ground state. The cooling process is therefore sensitive to the cooler detuning from the two-photon condition and can be used to optimize the GMC. In addition, the resonance strongly depends on the magnetic field present at the position of the atomic sample. At this stage, the atomic population is a mixture of all spin-states with various m_F quantum numbers. Each of these gets a different Zeeman shift induced by the stray field, which creates more possibilities for the Raman scheme between various states. This effectively broadens the resonance observed when scanning the cooler beam frequency around the Raman condition.

We measured the cloud width after 8 ms of fall time for various detunings of the cooler and observed that in the uncompensated case the minimum is shifted by around −1.6 MHz with respect to the theoretical value. In addition, it was quite broad as expected, which we interpret as coming from the Zeeman shifts owing to the stray magnetic field present.

We repeated the measurement with the stray magnetic field compensated, and observed that the minimum got narrower and its position became well-defined exactly on the detuning where Raman condition is fulfilled. This is another method for validation that indeed, we compensated the stray field successfully. The results of both measurements are presented in Fig. 3.20

Summary

In this chapter, we presented an overview of the K-Cs apparatus built in our laboratory. We focused mainly on topics where the author had a significant contribution, which complement the description depicted in the theses of other members of our group [76, 79, 83].

We discussed the construction and testing of the sub-millisecond off-switch of our main coils, which allows us to proceed with the stages of experimental sequences without the fear that the leftover magnetic field would influence the atomic sample. It was particularly useful for research done by M. Bocheński, who measured Feshbach resonances in K-Cs mixtures. Without our circuit the required high magnetic fields reaching hundreds of Gauss would distort the imaging procedure and hence the obtained data.

We presented an implementation of offset-locking of cesium lasers, based on a frequency divider, which allowed us to reference one laser with respect to the other with a frequency difference of around 9 GHz. Although it did not provide the phase-coherence we were hoping for, it is still a useful tool which allows us to simplify the laser system for cesium.

We also depicted a study on light-induced atomic desorption, which is a useful effect in single-chamber apparatuses, such as ours, which allows for temporary enhancement of the vapor pressure in the experimental cell. It reduces the required loading time of MOT and increases the obtainable number of atoms without affecting the proceeding cooling and trapping methods. We presented an adsorption-desorption model and experimental results that confirm its validity.

Finally, we presented the design and implementation of a bi-directional current source for our compensation coils along with control tests and noise measurements. We also discussed the influence of magnetic field on the cooling process in GMC and utilized it to optimize the cancellation of the stray field. It resulted in reaching state-of-the-art temperatures for potassium-39 and confirmed other research groups observations.

Chapter 4

Laser system for precision spectroscopy

In this chapter, I will describe the continuous wave (CW) laser system built with an idea of an autonomous, fully automated operation, which delivers light of desired frequency, referenced in real-time to a frequency comb.

The layout of this chapter is as follows. Firstly, I will discuss the motivation behind the system design and construction. Secondly, I will briefly introduce the concept of two-sample variance, which we used as an estimate of frequency stability. Then we will move on to the description of the hardware layer of the system, starting with the laser and the frequency comb. I will also describe the subsystem used for the selection of the comb spectrum , which increases the signal to noise ratio (SNR) of the beatnote between the laser and the frequency comb. Then, I will present the lock system which references the laser to the frequency comb, which concludes the discussion of the hardware layer of the system. Next, I will describe the software layer with four servers that control the hardware subsystems and present the data flow between them. Finally, I will discuss how the frequency of the laser is calculated and adjusted in various scenarios.

Motivation

Precise spectroscopy measurements performed in ultracold atomic or molecular samples require an advanced control over the laser light in terms of both the frequency tunability and the spectral linewidth. What is more, in many modern applications of lasers, in particular related to frequency metrology or quantum computing, it is a necessity to know the frequency of a laser with an accuracy much better than the

natural linewidth of the addressed transition. When this linewidth is below 1 MHz, even the best currently available wavemeters cease to be useful. The two most popular methods to stabilize the frequency of the laser at a given value are locking the laser to an ultra-low-expansion (ULE) optical cavity or to a frequency comb. In this research, we used the latter one.

The frequency comb is a high-end device developed around the turn of the twentieth century (foundations were laid by Theodor Hänsch for which he received the Nobel Prize [6]) and is commonly found in modern optics laboratories. Supported by a wavemeter, it can be used as an "optical ruler" to determine the absolute frequency of the laser and to lock it.

We have designed, built, and optimized a fully automated laser system in which the frequency reference is provided by the frequency comb. We programmed all of the hardware (the laser, the frequency comb, and electronics responsible for lock loops) in the system and provided an http-based application programming interface (API). Such an approach was chosen because it fits the architecture of experimental control and data acquisition in our laboratory, while also being flexible in terms of scaling and modularity.

A novel advantage of our system is that, thanks to wavemeter and frequency counter incorporation, the system can continuously monitor the laser frequency and apply corrections autonomously if needed. It also checks lock statuses of various variables and initiates the relock procedures. The software layer of the system was implemented and optimized with the idea of minimizing the possibility of unlocking a laser from the reference, providing a robust system suitable for precise spectroscopy in an ultracold atomic optics laboratory.

4.1 The concept of Allan variance

In this section, we briefly introduce the idea of a two-sample (Allan) variance. Whenever we come across a frequency source, and a laser can be viewed as one, the problem of characterizing its stability arises. For a stationary random variable, usually a proper variance estimator is the N-sample variance, square root of which is the standard deviation. However, oscillators have an intrinsic memory, because of their principle of operation as devices with resonators and positive feedback loops. This means that local frequency fluctuations accumulate in the phase error, and the assumptions of the central limit theorem are not fulfilled.

In other words, an oscillator amplifies low-frequency noise because its phase constantly integrates the perturbations. This leads to characteristic noise spectrum

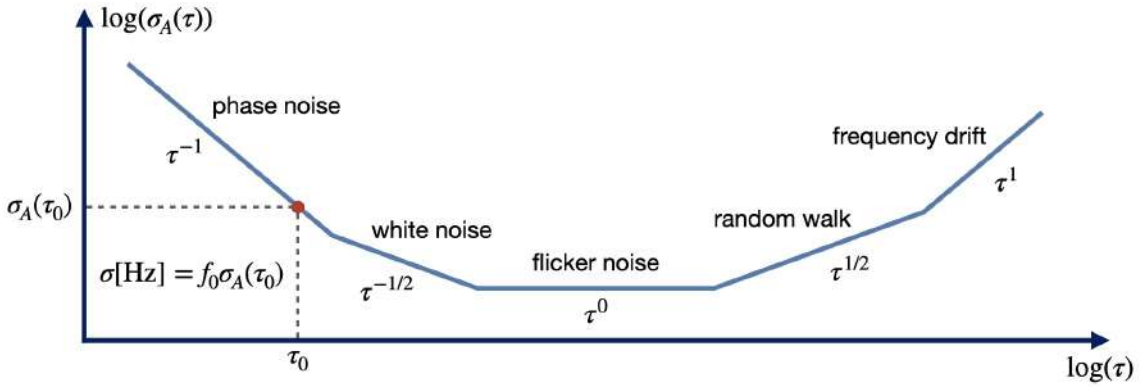

Figure 4.1: Exemplary sigma-tau plot of Allan deviation. Slope of the curve provides information about the dominating noise type.

components that are not integrable in terms of variance.

The types of noise are distinguished by their dependence on the frequency. In various regions, various effects give the strongest contributions, so the power spectral density of the fractional frequency is typically proportional to some power of frequency: $S_y(f) \propto f^\alpha$.

Two major effects encountered in oscillators are the flicker noise, where $\alpha = -1$ and the random walk noise, where $\alpha = -2$. The first causes random fluctuations around the central frequency, whereas the second results in a random drift of the oscillator frequency. The mechanism of origin of these noise types is characteristic for a specific type of oscillator. In case of a laser, they may come from micro-deviations of the cavity length, deformation of the cavity due to temperature drift, or integration of white noise if the laser is stabilized with an integrator.

If a standard N-sample variance is calculated with noise spectra with reciprocal dependence on frequency, it diverges with an increasing number of samples. A solution to this problem is the two-sample or Allan variance introduced in 1966 [104]. It is defined as one half of the expected square of the difference between two successive fractional frequency averages over an observation time τ, given explicitly by formula:

$$\sigma_y^2(\tau) = \frac{1}{2}\langle(\bar{y}_{n+1} - \bar{y}_n)^2\rangle \tag{4.1}$$

where $y_n = (f_n - f_0)/f_0$ is the fractional frequency difference with respect to the central oscillator frequency f_0, and the averaging, denoted by bar over a letter, is performed over the interval of τ.

In other words, instead of comparing each sample with the global mean, the Allan variance compares adjacent interval averages, so that long-term drifts and

low-frequency divergences are effectively canceled. This two-sample construction provides a convergent and meaningful measure of oscillator stability even in the presence of flicker or random-walk noise.

Another view of the Allan variance is given by analysis of the power spectral density. In such a picture, the variance is given by the formula [105]:

$$\mathrm{Var}[y(t)] = \int_0^{f_h} S_y(f)|H_x(f)|^2 \mathrm{d}f \tag{4.2}$$

where $H_x(f)$ is a weight function and f_h is the upper cutoff frequency, usually determined by hardware factors. For the N-sample variance, the weight function is equal to unity, and it is clearly visible that such an integral diverges for flicker and random walk noise. In case of Allan variance, the weight function is given as:

$$|H_A(f)|^2 = \frac{2\sin^4(\pi f\tau)}{(\pi f\tau)^2} \tag{4.3}$$

which is proportional to f^2 for small frequencies and effectively kills divergent noise contributions.

Allan deviation, a square root of the Allan variance, depends on the averaging time τ and is usually presented as a sigma-tau plot, rather than a single value. The unique feature of Allan deviation is that different types of noise that dominate in certain time-averaging (or frequency) regions can be easily distinguished by the slope of the deviation on a log-log sigma-tau plot. An example of such a plot is shown in Fig. 4.1.

The stability of the oscillator can be read from the plot as follows: given the period τ at which one is interested (for instance in case of laser stability, it can be the time at which we illuminate the sample) one needs to read the corresponding Allan deviation. Then it needs to be multiplied by the frequency of the oscillator, to translate the deviation from fractional to Hz units. This procedure is also shown in Fig. 4.1.

The last remark is that the Allan deviation comes with many versions of the algorithm, suited for particular needs while estimating the frequency source stability or types of noise contributions for different averaging times. The one used in this thesis is called the overlapped Allan deviation. In this version of variance estimation, the succeeding time intervals are shifted by one sample, so that more pairs of differences are constructed (in case of standard Allan variance it is $N/(2\tau)$, whereas in case of overlapped version it is $\approx N - 2\tau + 1$) and almost the whole record is used for variance estimation calculation. The overlapped Allan variance is statistically more

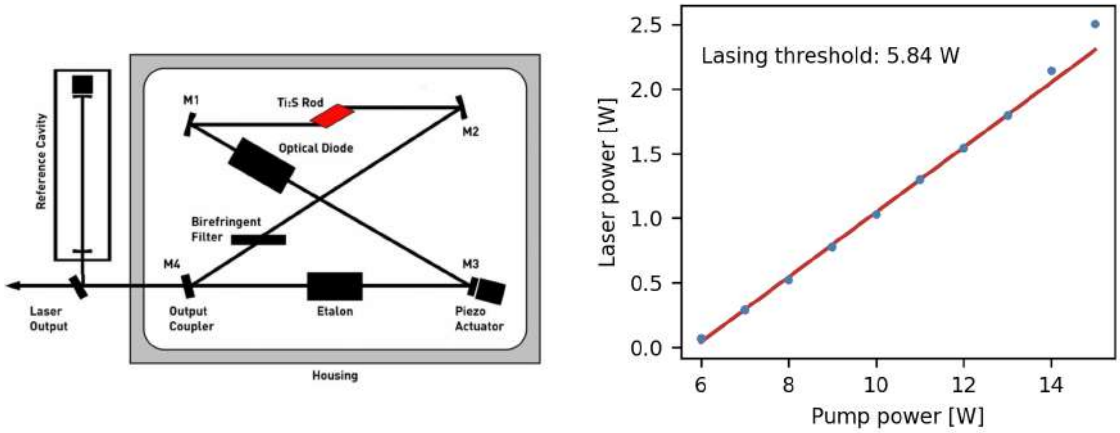

Figure 4.2: Left hand side: Scheme of the SolsTiS cavity. Image taken from laser's manual. Right hand side: Output power of SolsTiS versus the pump power, measured at default SolsTiS wavelength 780 nm. Linear function was fitted, yielding the lasing threshold at 5.84 W. This data was measured with borrowed laser pump Verdi V18, due to malfunction of our G-Sprout pump.

efficient, because it reuses all possible adjacent frequency averages rather than only non-overlapping blocks, which reduces the estimator's uncertainty for a given data record length.

Due to many variants of the variance and the corresponding deviations, a settled system of abbreviations is used in the literature. The standard Allan deviation is often denoted as ADEV, and the overlapped version is denoted as OADEV or ADEV overlapped. In this thesis, we use the latter.

As a comment from the author, while learning about the Allan deviation, a great source of information was the book "Handbook of Frequency Stability Analysis" [105]. It contains a clear explanation of the theory behind two-sample variance, as well as a lot of explicit formulae regarding different variants of Allan deviation, which were a great help when writing the code to analyze the data.

4.2 MSquared SolsTiS laser

This section discusses the continuous wave (CW) laser setup in the laser system. We utilize the MSquared SolsTiS Ti:Sapphire laser pumped with a 15 W G-Sprout 532 nm laser by Lighthouse Photonics. The scheme of the laser cavity alongside the

output power versus pump power measurement results are shown in Fig. 4.2. This particular measurement was conducted with the laser pumped by borrowed Verdi V18[1] pump, due to malfunction of our G-Sprout pump. All other measurements presented in this chapter were done with G-Sprout.

By design, SolsTiS is fully remotely controlled. All actuators of the laser cavity are adjusted by a laser controller unit called ICE-BLOC. It hosts a server with a website, which lets the user change the crucial SolsTiS parameters to control the wavelength of the laser or adjust technical parameters (temperatures, diode gains, PID coefficients, etc.). ICE-BLOC server also has an incorporated http-based API, which perfectly fits the architecture of our laser system. We use it to control the laser by our management software, however, the website is sometimes useful for diagnostics or manual intervention.

Optical setup

The optical setup of the laser, shown in Fig. 4.3, was constructed to distribute the light between the subsystems and the experiment. We have built two paths with fiber outputs for the wavemeter readout and the frequency comb lock subsystem. Only a small portion of the laser power is directed into those paths. The first one measures the laser frequency coarsely, while the second one is used to lock the laser finely, in reference to the frequency comb. The third path, with majority of the laser power, ends with a fiber output going to the main experimental chamber. It has an acousto-optic modulator (AOM) added acting as a fast switch of the laser light. We optimized the coupling of the -1$^{\text{st}}$ diffraction order of the AOM when the laser was tuned to 852 nm and the AOM carrier frequency was set to 110 MHz.

The diffraction order angle of the AOM depends on the light wavelength, and the laser is tunable over a broad range of hundreds of nm, so at different wavelengths the coupling to the fiber would lose efficiency. Effectively, we would lose the light power available in the experiment. We decided to compensate for this effect by changing the carrier frequency of the AOM and sustain high coupling efficiency at different wavelengths. We will now present the description of this calibration.

Due to the Bragg condition, the AOM fulfills the equation which links the laser wavelength λ, the AOM carrier frequency f_{AOM} and the diffraction order angle ϑ_{diff}:

$$f_{AOM} = \frac{2v_s\vartheta_{diff}}{\lambda} \tag{4.4}$$

[1]Verdi V18 532 nm pump laser by Coherent

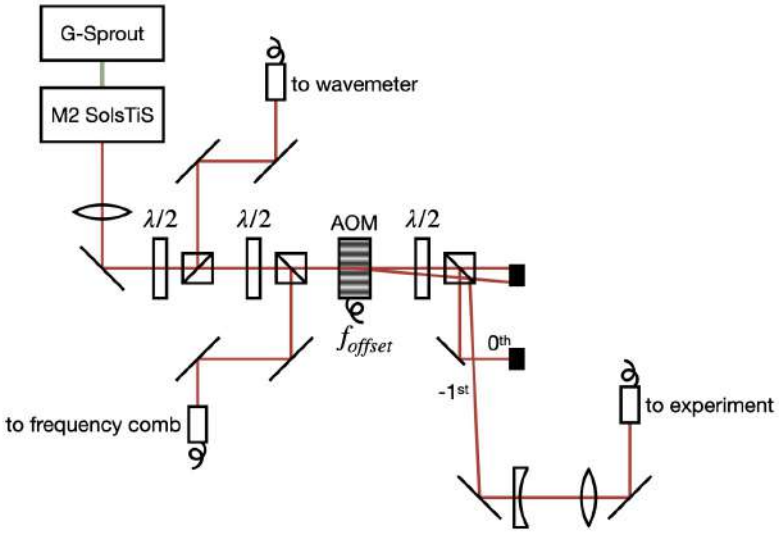

Figure 4.3: Scheme of the MSquared SolsTiS optical setup. Laser light is split into three paths. They distribute the laser power between fiber outputs to the wavemeter, frequency comb lock subsystem and the experiment. An AOM is added in the experiment output path, acting as a fast on/off switch.

where v_s is the speed of sound in the AOM crystal medium. As we would like to keep constant ϑ_{diff}, the equation gives us a relation between λ and f_{AOM}.

During the calibration measurements, we observed that a modification of this equation by an offset in the wavelength could be fitted with lower residual values. In the wavelength domain, the origin of the offset is not clear, however, when rewritten to the frequency of the light, it becomes a constant offset in the diffraction angle. We interpret this as coming from a slight misalignment of the AOM or from device-specific reasons. We have verified that the calibration results with such a corrected equation were indeed optimal ones. Taking this into account, the calibration function we used was as follows:

$$f_{AOM}^{fit}(\lambda) = \frac{a}{\lambda - \lambda_0} \tag{4.5}$$

The calibration curve was obtained using the following procedure. The carrier frequency of the AOM was scanned around the central frequency estimated from the Eq. 4.4 for different laser wavelengths. At the same time, laser power was measured at the output of the fiber. From this we obtained a set of gaussian-like curves of coupled power versus AOM carrier frequency, each for a different wavelength. To

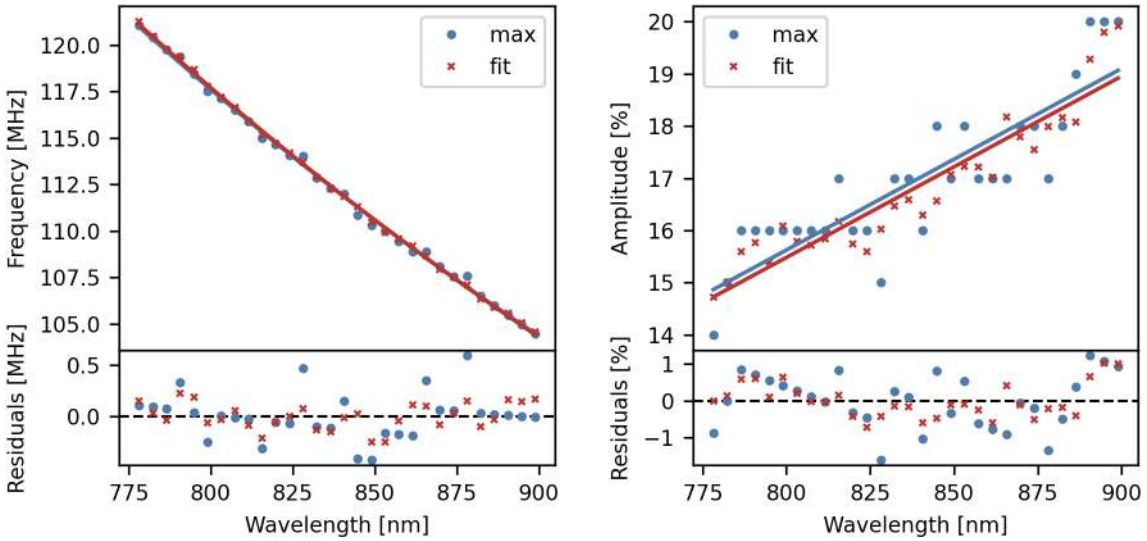

Figure 4.4: Calibration curves of the laser optical setup output AOM. Optimal values in here mean the highest efficiency of laser light coupling to the experiment output fiber. "Max" annotation means that points were chosen as the frequency/amplitude at which the coupled power was the highest. "Fit" annotation means that points were determined by fitting a gaussian function or higher-order polynomial. Left hand side: Optimal AOM carrier frequency versus the wavelength of the SolStiS laser. Right hand side: Optimal AOM carrier amplitude (at optimal carrier frequency) versus the wavelength of the SolsTiS laser. Percentage units are in terms of DDS output amplitude. Solid lines represents the calibration curves based on the fit to the data.

derive the calibration curve from this dataset, we estimated the optimal AOM carrier frequency with two techniques. The first was to choose the frequency corresponding to the highest coupled power. The second was to fit a gaussian function to each curve and get the peak position. The fit-based method proved to be more precise and gave lower residuals in the final calibration curve, which is shown in Fig. 4.4.

In principle, the efficiency of diffraction in a broad range of wavelengths may depend not only on the carrier frequency of the AOM but also on its power. As an RF source, we use the direct digital synthesizer (DDS), which also has a controllable output power set as a percent of the maximal value. For this reason, we performed the aforementioned measurement with an additional outermost loop scanning different DDS amplitudes. The procedure of data analysis was similar, however, in this case we chose a higher-order polynomial as the best fitting function, since the amplitude

efficiency of the AOM typically rises monotonically at low powers, then reaches an optimal peak value and finally falls to a saturation plateau at high powers. This behavior is not described by any straightforward function, so polynomials bounded by the measurement ranges are the easiest, yet precise estimation. We have found that the optimal calibration of the amplitude can be described by a linear function, which is shown in Fig. 4.4.

The calibration of the output AOM is crucial not only in order to achieve the highest coupling efficiency and thus the highest available power in the experiment, but also for the determination of the laser absolute frequency, since AOM introduces a shift in light frequency equal to the RF carrier. As we can see from the calibration, this shift is wavelength dependent and changes on the span of a few MHz, which is a large value compared with the obtained laser linewidth.

Frequency tuning

The SolsTiS laser has a few layers of frequency tuning actuators. I shall describe them starting with the coarsest one and going towards the finest.

The first layer is the tuning of the intracavity birefringent filter (BRF). It is able to tune the laser wavelength within approximately one etalon free spectral range (FSR) or better, so further tuning may proceed. The wavelength resolution of this step is around 0.15 nm, according to the manual.

The second layer is the adjustment of the intracavity etalon. It can tune the laser frequency to within 1 GHz from the desired frequency. It has a built-in stabilization loop which locks the peak of etalon transmission to the nearest longitudinal mode of the cavity. This loop sets the coarse value of the laser frequency.

The third layer is tuning the cavity length by controlling the piezo actuator on the mirrors of the cavity. There are two actuators, a coarse one and a fine one, which can tune the frequency down to the MHz range. In our case, we use this actuator to tune the laser frequency to around 110 MHz from the desired frequency. This value comes from the frequency comb characteristics.

The last, fourth layer is also controlling the cavity length through coarse (slow) and fine (fast) piezo actuators, however, these are controlled externally. Although their tuning range is similar to that of the third layer, we consider them as the last step since they are controlled by the stabilization loop that references the SolsTiS to the frequency comb.

The first three layers can be controlled by the user via the laser's webpage or by sending requests to the laser control system. We utilized the SolsTiS controller API in our automatization design and controlled them via a dedicated server. The

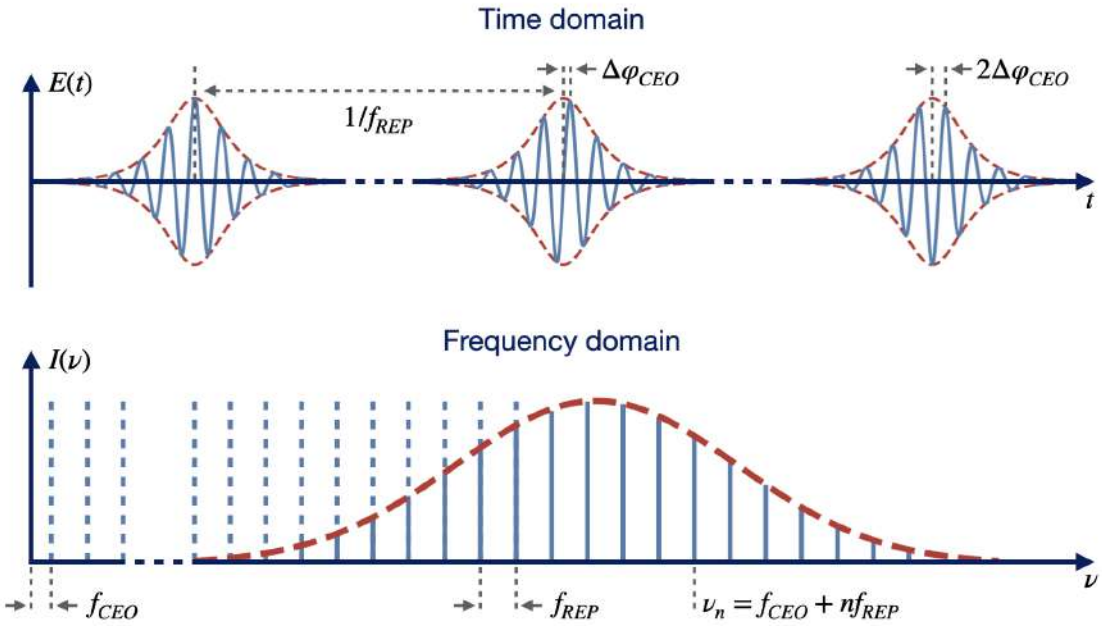

Figure 4.5: Visualization of the frequency comb in temporal (upper panel) and spectral (lower panel) domains. Details about the correspondence of f_{CEO} and f_{REP} between the regimes and their origin are discussed in the text.

first three layers are used to tune the laser frequency down to the value at which the lock setup referencing the laser to the frequency comb can be engaged, which, on the other hand, uses the fourth layer.

4.3 Frequency comb

In this section, I shall discuss the frequency comb hardware. I will start with a brief explanation of this particular laser type and follow with the stabilization system we have implemented.

The optical frequency comb (OFC) is a type of femtosecond pulsed laser with a spectrum that is a train of narrow, equidistant frequency spikes called teeth. The visualization of the comb in the temporal and spectral domains is shown in Fig. 4.5. There are two frequencies that govern the position of each tooth, namely the repetition frequency f_{REP} and the carrier envelope offset (CEO) frequency f_{CEO}. The first is simply equal to the repetition rate of the pulses in the temporal domain or to the separation between the teeth in the frequency domain. The CEO frequency

describes how the phase of the electromagnetic wave changes between concurrent pulses in the time domain, hence the name carrier (phase) envelope (group) offset. In the frequency domain, it is equal to the shift of the comb spectrum with respect to 0. If we denote the optical carrier phase relative to the pulse envelope as φ_{CEO}, the f_{CEO} is given as [106]:

$$f_{CEO} = \frac{1}{2\pi}\frac{\mathrm{d}\varphi_{CEO}}{\mathrm{d}t} \tag{4.6}$$

The f_{REP} and the f_{CEO} usually fall in the RF domain and can be electronically stabilized. In such a case, the frequency of the n^{th} tooth of the comb can be derived from a simple yet accurate formula [106, 6]:

$$\nu_n = f_{CEO} + n f_{REP} \tag{4.7}$$

where we use the Greek letter ν for the optical domain and the Latin letter f for the RF range.

Although it may seem as though the comb spectrum is infinite, it is in fact confined within certain optical frequency ranges. Eq. 4.7 is then physically correct for the f_{REP} and f_{CEO} in the RF range and n of the order of millions. This makes the stabilization of the f_{CEO} challenging, as it is not directly observed within the comb optical spectrum. The most common self-referencing method, called f-to-2f interferometry [107, 108, 109], utilizes non-linear effects to produce a second harmonic of the low-frequency part of the comb spectrum and beat it with the high-frequency wing. This requires a sufficiently broad comb spectrum, spanning across an optical octave, however, if the requirements are met, the f_{CEO} can be measured as the heterodyne beat:

$$2\nu_n - \nu_{2n} = (2f_{CEO} + 2nf_{REP}) - (f_{CEO} + 2nf_{REP}) = f_{CEO} \tag{4.8}$$

Frequency combs are used as modern frequency reference devices and have plethora of applications [110]. They can be used to lock CW lasers on absolute frequencies for high-precision spectroscopy purposes [111], as in this thesis. Another example is to phase lock two laser frequencies that are situated far away from each other in the optical spectrum by phase locking both lasers with the same comb [112, 113, 114].

Due to supercontinuum generation, modern frequency combs can have a broad spectrum of hundreds of nanometers, without destroying the integrity of the comb lines, so they may work as a bridge between a wide range of spectral regimes and the telecom regime [115]. This is used for instance to send an optical atomic clock signal at long distances via commercial fiber networks by first translating it to telecom frequency [116, 117]. OFCs have also found application in time metrology, where

they are used to produce microwave/RF frequency standards [25], or used to compare two optical atomic clocks for evaluation purposes [4, 118]. The last example is the direct application in spectroscopy with a large set of parallel detection channels [119] and its variations, dual comb spectroscopy [120, 121] or cavity enhanced frequency comb spectroscopy [122].

At first sight, the frequency comb may seem like a standard femtosecond laser with f_{CEO} stabilization. However, Eq. 4.7 returns frequencies in the optical range for n in the range of millions. This means that the uncertainty of f_{REP} is multiplied by the same coefficient and can contribute significantly to the total uncertainty of the determination of the frequency of the tooth. In order to outperform modern wavemeters, it must be stabilized to mHz or sub-mHz levels. Frequency combs are then designed as ultrastable femtosecond lasers with the availability to lock the f_{REP} with such low uncertainties.

Comb stabilization

We have locked our comb using standard laboratory electronics (Mode-Locked Technology phase comparator[2] and TEM Messtechnik LaseLock[3] for f_{REP} and STEMLab RedPitaya[4] with an open source PLL[5] for f_{CEO}).

In addition to the control devices, we have added other standard RF components to the loops, such as amplifiers to increase the signal power or filters to select the desired frequencies. The f_{REP} is controlled by piezo actuators, so we also included a high-voltage amplifier[6] between the LaseLock and the comb.

The filters reject the higher harmonics generated by the amplifiers and prevent aliasing as we are using digital control devices. It is especially important in case of f_{CEO} since its monitor output has low signal power and dominating residuals from the f_{REP}. In addition, parasitic frequencies, which are always present in a laboratory, captured by cables due to the antenna effect are filtered out. They do not possess high power, yet can still contribute to the noise.

We have also added 50:50 RF power splitters to create additional outputs. They are connected to the frequency counter that monitors f_{REP} and f_{CEO} in real time and provides the information for the calculation of the CW laser frequency.

[2] ModeXφ digital phase comparator by Mode-Locked Technology

[3] LaseLock universal and compact laser frequency stabilization electronics by TEM Messtechnik

[4] STEMLab 125-14, version with external clock

[5] Open source PLL firmware and software for RedPitaya, designed especially for frequency comb lock loops

[6] PDu150 high-voltage amplifier by PiezoDrive

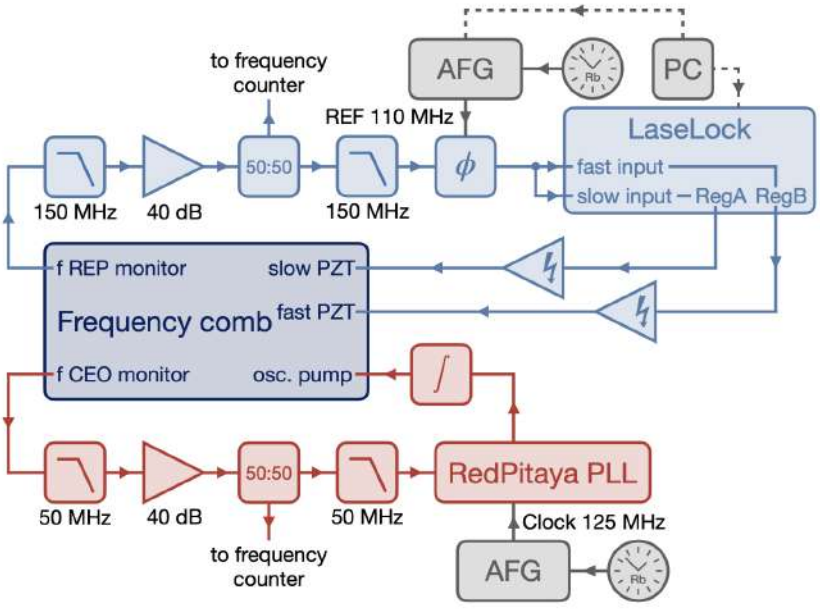

Figure 4.6: Scheme of the frequency comb electronic phase lock setup. The upper, light blue part is the repetition frequency lock using Mode-Locked Technology phase comparator and Messtechnik LaseLock. The lower, red part is the CEO frequency lock using an open source RedPitaya PLL. Gray parts correspond to clock sources and PC control. Details of the lock loops are described in main text.

We have found that the quality of the splitters is crucial, since later on we use an RF switch. It happens that when switching between frequency channels, the impedance of the line suddenly changes between 50 Ω and Hi-Z, which introduces noise spikes probably due to back reflected waves. They were high enough to destabilize the lock loop and in effect the frequency comb. Originally, we used custom-built 50 Ω 50:50 splitters, however, the problem was solved after exchanging them with proper parts from MiniCircuits with higher isolation between outputs.

The last part of the lock loop that we want to mention is our custom-built RedPitaya expander, which is described in detail in App. B and enhances the operation of RedPitaya by broadening its dynamic range. It is denoted in Fig. 4.6 as a square with an integral sign inside. Without this part the CEO lock loop needed to be adjusted twice a day by changing the setpoint frequency so that it is in the range of the RedPitaya's reach. Now, the CEO lock can run for a few days without any adjustments.

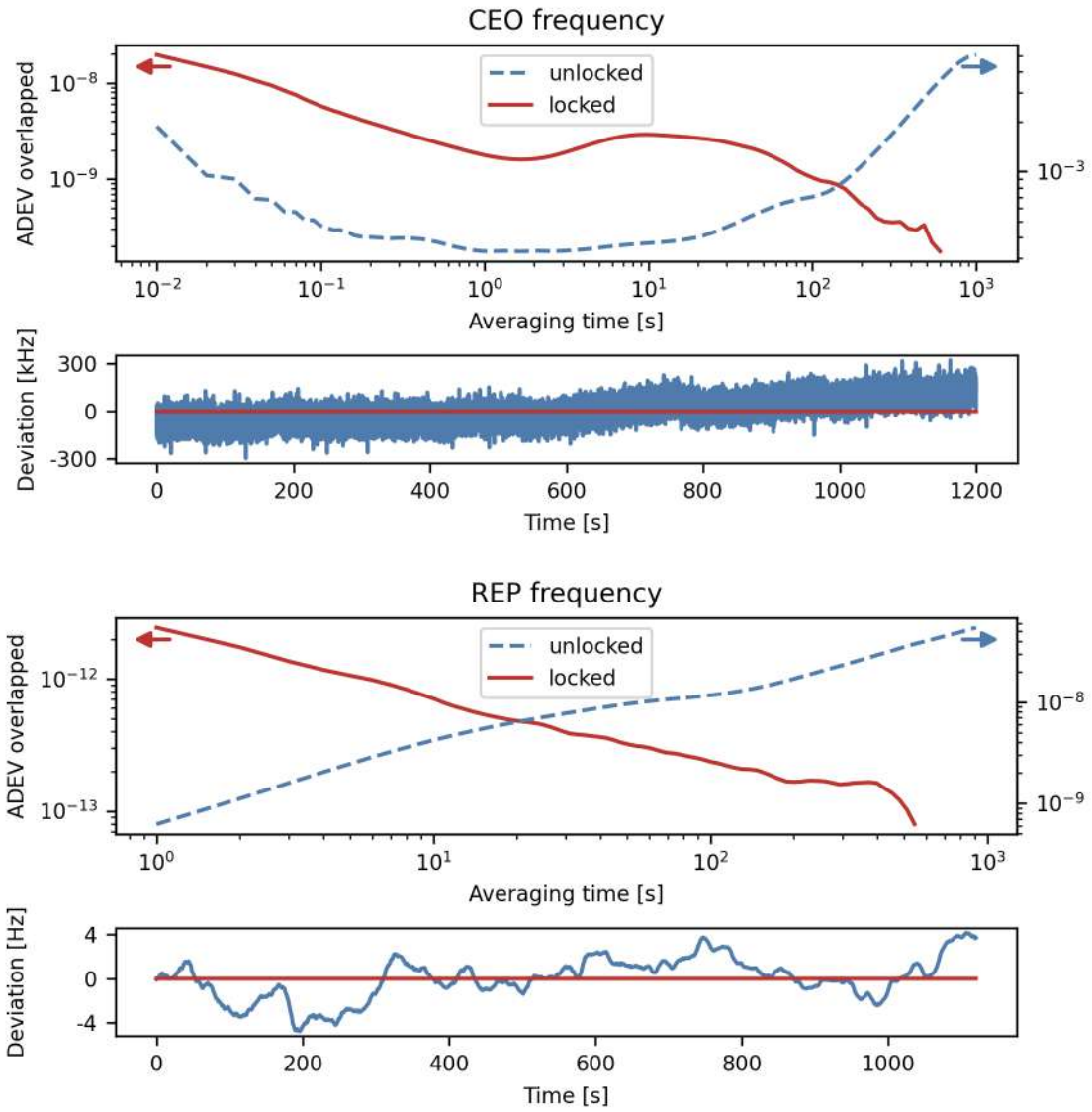

Figure 4.7: Overlapped Allan deviation plots for the comb stabilization. Locked (left y axes) and unlocked (right y axes) cases are shown. Lower panels show measured frequency as deviation from the average. Top plot: CEO frequency deviation measured over 20 min with gatetime of 10 ms. Bottom plot: repetition frequency deviation measured over 20 min with gatetime of 1 s.

To increase the stability and accuracy of the loop we referenced all oscillators in the system (RedPitaya clock, f_{REP} reference frequency, and a clock of a frequency counter used in measurements of the frequency stability) to a single Rb atomic clock. This ensures the phase coherence between all devices.

During the construction of the lock setup, we checked different combinations of the loop components and their placement order and present the complete and final scheme of the comb lock system in Fig. 4.6. We also optimized the loop settings of the controllers. In case of f_{CEO}, the RedPitaya PLL software has a GUI, which shows the QI diagram of the stabilized frequency. It is quite useful during optimization of the loop filter and makes the procedure easier for a user of limited experience. Basically, it gives a real-time view on how the system reacts to certain loop filter parameters. In case of f_{REP}, we observed the output of the phase comparator on the oscilloscope and locked it coarsely. Then we switched on the square frequency modulation of the reference frequency and observed the step response of the lock loop. This was helpful with the final optimization of the loop parameters.

After optimization of the design and building the lock system, we proceeded to the measurement of the long-term stability of comb frequencies. We have measured the overlapped Allan deviation over 20 min with gate times of 1 s for the f_{REP} and 10 ms for the f_{CEO}. Such gate times ensured that the required resolution of the measurement is reached. From the plots, presented in Fig. 4.7, one can read that over the averaging time of 1 s, which is a typical time range at which the atomic sample is illuminated with the laser, the uncertainties of the comb frequencies are around 10^{-12} for f_{REP} and 10^{-9} for f_{CEO}. Due to typical frequency values $f_{REP} \approx 110\,\text{MHz}$ and $f_{CEO} \approx 30\,\text{MHz}$ this translates to $\approx 0.22\,\text{mHz}$ and $\approx 60\,\text{mHz}$, respectively. These are state-of-the-art values and are suitable for high-precision spectroscopy applications.

4.4 Comb spectrum selection

In this section I will describe the optical subsystem for obtaining the beatnote signal between the CW laser and the frequency comb. It is the first step in referencing the laser to the frequency comb and has some subtleties which require discussion.

In case of phase-locking two CW lasers by their beatnote stabilization, the standard approach would be to overlap the beams spatially, project their polarizations onto a single axis, and measure the signal on a photodiode. However, if one of the lasers is a frequency comb, which is a pulsed laser, apart from the desired beatnote of the CW laser and the comb, a self-beat signal of the comb teeth would be produced at the repetition frequency. As the spectrum of the frequency combs is usually broad

(of the order of tens of nanometers), the self-beat signal between the succeeding teeth would dominate the CW laser beatnote used for locking.

This may be explained as follows: the optical power per tooth is usually small, and a useful beating signal comes from beating with just one tooth. Simultaneously, the self-beating of the comb occurs throughout its entire spectrum (tens of thousands of teeth). One could increase the beat power by increasing the CW laser power, but this on the other hand rises the noise level. Additional power from the self-beat may increase the noise level as well, not only around the repetition frequency, but also in other regions of the RF spectrum. These phenomena effectively lead to lowering the SNR of the desired beat signal and can introduce unwanted noise in the phase-locked loop (PLL) which worsens the lock tightness or even breaks it.

For this reason, there are methods to filter the comb spectrum and improve the SNR of the desired beatnote. Some of them are based on using dispersion optical elements, such as diffraction gratings [111] or AOMs [123], which distinguish different regions of the comb spectrum geometrically. Then, a small aperture is employed to spatially filter only the desired part of the comb's spectrum. A rather interesting method of improving the SNR is gated measurement, where the acquisition of the beatnote is synchronized with the repetition frequency of the comb [124]. This technique is based on the fact that because the period of the femtosecond pulse is small compared to the repetition rate, most of the time the photodiode is measuring and integrating the noise. However, when the measurement is gated, only the useful signal is captured, which lowers the floor of the noise, effectively increasing the SNR of the desired beatnote.

In this dissertation, we decided to employ a version with a diffraction grating, which was proposed by T. Hänsch et al. [111]. We have expanded the method to a fully automated system that works for a wide range of wavelengths. We will now describe the optical setup and our design for an automated rotation of the grating.

Optical setup

The optical setup consists of two parts, namely an input part and a spectrum selection part. The scheme of the setup is shown in Fig. 4.8.

In the first section the laser and frequency comb beams are coming in from optical fibers and are collimated and resized to the same diameter, around 2 mm of double Gaussian beam waist $2w_0$. Then they are overlapped on a polarization beam splitter (PBS) and pass through a half-wave plate, rotating the polarizations by 45°, and a second PBS. It is a crucial point because a beatnote between the laser beams is basically an interference, but happening in time, not as usually seen in space.

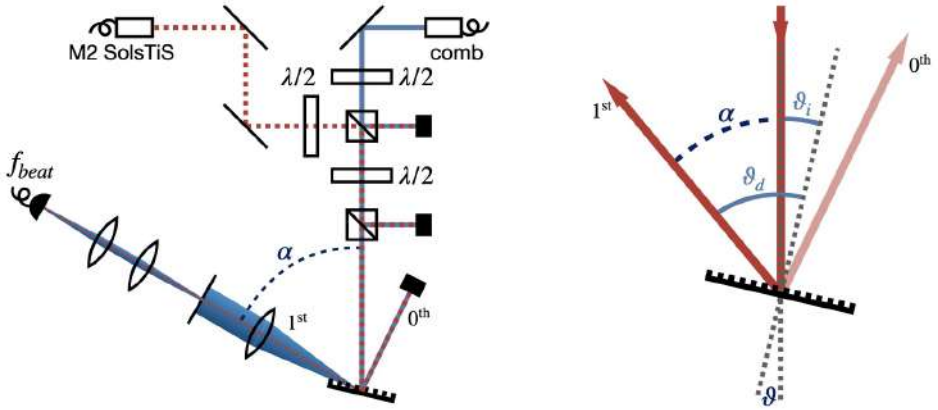

Figure 4.8: Left hand side: Scheme of the optical setup. Red dotted line represents the beam of the titanium sapphire laser. Blue line represents the beam of the frequency comb. Blue shapes with gradient of colors represent the diffraction effects on the frequency comb - geometric splitting due to a broad spectrum. Right hand side: Geometry of the rotating grating setup which leads to parametrization of the grating equation. ϑ_i - the incident beam angle, ϑ_d - diffraction angle both with respect to the grating normal. α - output beam angle, ϑ - grating rotation angle both with respect to the incident beam. Also specular reflection (0^{th} order) is shown.

Since interference does not occur between beams of orthogonal polarizations, it is important to project them onto the same axis. It may seem obvious, but from the author's experience (and I have built many beatnote-based setups during the PhD studies) it is the part of the setup that is the most common to forget.

The second section is built to select a narrow part of the comb spectrum within the requested range. This is done using the dispersive property of the diffraction grating. The frequency comb beam, which has a continuous spectral band of tens of nanometers, when reflected from the diffraction grating, splits and forms a thin line due to the fact that the reflection angle of a given diffraction order depends on a light wavelength. The laser beam is reflected only at a single angle as it has a narrow spectrum.

Since the beams are overlapped before being diffracted from the grating, the laser beam and a part of the comb spectrum with the same central wavelength are diffracted under the same angle and are geometrically overlapped. They are focused on a pinhole of 100 μm diameter using a 50 mm lens, which ensures that unwanted parts of the comb spectrum are filtered out. In addition, there are collimating and focusing lenses and a photodiode.

Crucial construction points of the setup are the perfect spatial overlap of the beams on the PBS and hitting the diffraction grating exactly in the rotation axis. The first ensures that the beams follow the same optical path after being diffracted off the grating. The second is important since slight misalignment would result in additional angular offset of the diffracted beam, which would not hit the center of the small pinhole.

In our setup we used a ThorLabs ruled reflective diffraction grating[7] with 750 nm blaze wavelength and 1200 grooves per mm. These parameters were the most suitable for our application.

Diffraction grating simulation

The setup was designed with the idea of being able to lock the laser to the comb for different wavelengths. However, the diffraction angle depends on the wavelength, so when the laser is tuned, the diffracted beam moves in space and misses the pinhole and photodiode. We use a Ti:Sapphire laser, which can be tuned in a wide range of wavelengths from around 780 nm to 1100 nm, so this effect is by no means negligible - in fact, it is dramatic. There are two options for the setup to be operational, namely, either we could move the lenses, pinhole, and photodiode and track the diffracted laser beam, or we could rotate the grating and compensate for the angular change. We chose the second option because it is much easier to build and implement as only one part is rotated instead of a few parts on a long arm.

By rotating the grating we are able to change the diffraction angle and compensate for the changes introduced by different wavelengths. The equation governing this process for the first diffraction order is following [125, 126]:

$$\sin\vartheta_d + \sin\vartheta_i = \frac{\lambda}{d} \tag{4.9}$$

where ϑ_d is the diffraction angle, ϑ_i is the incident beam angle, λ is the light wavelength and d is the diffraction grating constant.

Due to the geometry of the setup, we introduce a different set of coordinates, bound with the laboratory frame, not the grating. Then, the grating equation can be rewritten in terms of α - the constant output angle of the diffracted beam and ϑ - the rotation angle of the grating. From Fig. 4.8 it can be clearly seen that $\vartheta_i = \vartheta$ and $\vartheta_d = \vartheta + \alpha$. In such parametrization, the grating equation takes the form:

$$\sin(\vartheta + \alpha) + \sin\vartheta = \frac{\lambda}{d} \tag{4.10}$$

[7] GR13-1208 Ruled Reflective Diffraction Grating by ThorLabs

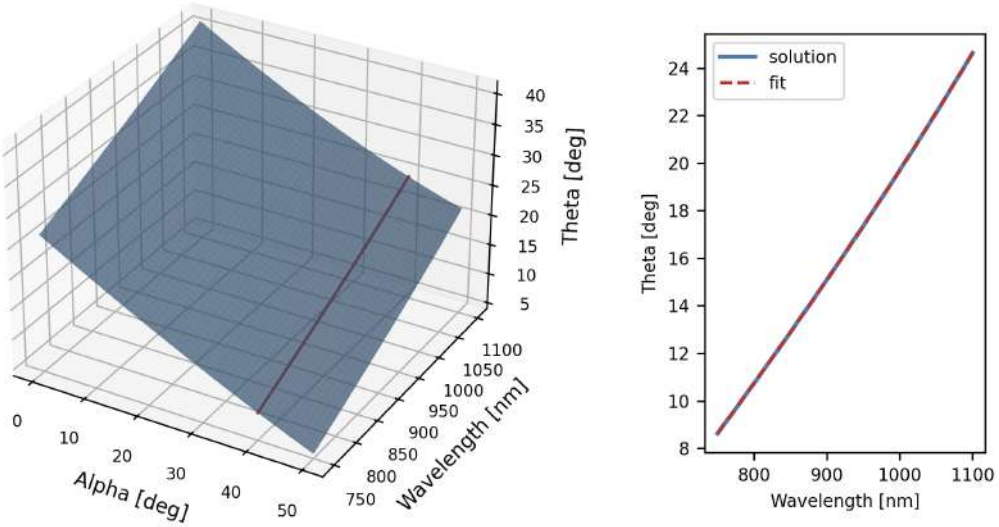

Figure 4.9: Left hand side: Simulation results of the grating equation (Eq. 4.10). α axis stands for the output angle of the setup. Wavelength axis stands for the wavelength of the laser light. ϑ axis stands for the rotation angle of the grating fulfilling Eq. 4.10 for given α and λ. Red line is the section of the surface at $\alpha = 40°$ which was chosen in our setup. Right hand side: Grating rotation ϑ vs wavelength, calculated for $\alpha = 40°$. A numerical solution to Eq. 4.10 and a fitted calibration curve are shown, which perfectly overlap.

Solving this equation with fixed α and λ returns a value of ϑ at which the grating needs to be rotated, so that the diffracted beams follow the optical axis of the lenses, the pinhole and the photodiode part of the setup.

Prior to the construction of the optical setup, we simulated this equation solving it for different α and λ values to obtain a theoretical calibration curve. In given parameter bounds, it returned a smooth and monotonic surface, shown in Fig. 4.9.

To parametrize the simulated surface we decided to slice it with respect to α and fit 3^{rd} order polynomials to each slice. This gives a theoretical prediction of ϑ for a fixed α and variable λ.

Further on, we took the coefficients resulting from the previous fit and plotted them against α. This way we obtained 4 curves, corresponding to the parameters of fits of each of the slices differing by α. To such curves we fitted a 4^{th} order polynomials.

Ultimately, we obtained a set of parameters, which can be used as follows. In a

given setup, the α is set to a constant value due to the geometry of the optical setup, as it is the angle between the beam incident onto the grating and the diffracted beam, hitting the pinhole and photodiode. For a given α we can calculate, from the second round of fits, the coefficients of a 3^{rd} order polynomial, which describes a curve of the optimal ϑ against the laser wavelength λ.

We chose such approach since the function describing the rotations was smooth. In a sense, we have exchanged one two-dimensional fit to two one-dimensional fits. Two-dimensional fit would be troublesome, because the function describing it would need to depend not only on powers of both α and λ, but also on mixed products $\alpha^i\lambda^j$. Two 1D fits separated in orthogonal directions were easier to parametrize than one two-dimensional fit and the solution of the grating equation was smooth enough for this method to converge.

In our case α was set to 40° due to the size of the lens focusing the diffracted light on a pinhole. We chose 50 mm lens because of its high enough focusing power, so that the waist at the focal length would fit in the 100 μm pinhole. The output angle of 40° was simply the smallest angle at which the one inch diameter lens with a mount would not block the beam that is incident on the grating. The diffraction efficiency would be higher for smaller angles, however, we have quite a lot of power available in the setup. In a case where frequency comb or the CW laser would provide no power to waste, a smaller lens diameter and smaller output angle would be more beneficial.

Diffraction grating mount

To rotate the diffraction grating, we have developed a dedicated mount, which is described below. At first we tried two options with a servomotor and stepper motor rotating the grating via 3D printed gears. Those approaches provided insufficient resolution and were not repetitive due to gears backlash. For this reason, we decided to utilize a rotation mount from Thorlabs, namely ELL14[8]. It is a piezoelectric mount with accuracy of 0.4° and repeatability of 0.05°. Although this solution is costly, it is far more effective than previous approaches.

The ELL14 motor is placed on a 3D printed base that can be attached to the optical table using standard elements. The motor has a threaded hole in the center, in which we placed an aluminum pole that can be attached with retainer rings, which also allow height adjustment. At the top of the pole, there is a holder for the grating, which is placed in such position that the grating surface is exactly at the axis of rotation of the pole. We added setting screws at the back of the grating mount to finely adjust the position and angle of the grating surface. Last element

[8]ELL14 Rotation Mount with Resonant Piezoelectric Motors by ThorLabs

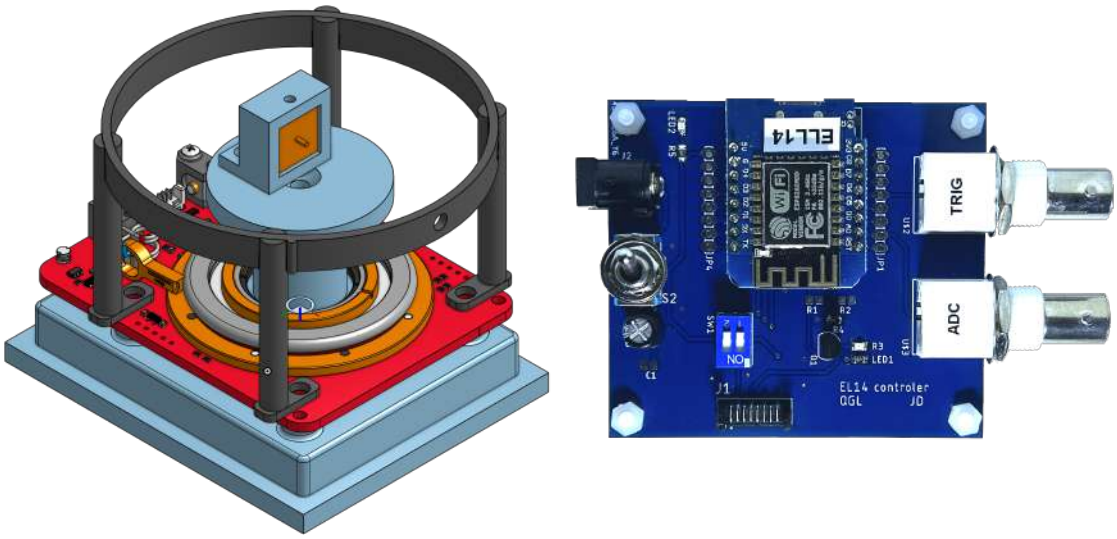

Figure 4.10: Left hand side: 3D model of the grating rotation mount. Blue base was 3D printed and is meant to hold the mount on an optical table. Colorful, mostly red part is the ELL14 piezoelectric rotation mount from ThorLabs. Top blue parts are the holders for the diffraction grating. Those parts were made in aluminum as it is stiffer than 3D printed parts and can withstand the rotation acceleration. The height of the grating can be adjusted by moving retainer rings in the ELL14 mount. Additional 3D printed black ring on posts was added with input and output holes at set angle $\alpha = 40°$ to coarsely align the setup and as a first filtering stage of the diffracted frequency comb light. Right hand side: A photograph of the custom made motor controller, based on ESP8266.

is a ring attached to the mount on 4 smaller poles, which has holes for the incident and output beams. It helps to adjust the position of the mount in the optical setup and also serves as the first filtering stage of the diffracted frequency comb light. The 3D model of the complete mount is shown in Fig. 4.10.

The mount is controlled by a self-made controller based on WemosD1 mini board with ESP8266 microcontroller, programmed in C++. Its major advantage is that it can connect to WiFi and host an http server, so control can be done via a hosted webpage or http-based API, which fits perfectly with the server-based architecture of the whole system.

For ease of operation, based on the solution of Eq. 4.10, we implemented an algorithm that rotates the grating for a given wavelength of the CW laser. However, because of the system's lack of ideal accuracy, it may not be rotated to a fully

optimized position. For this reason, we developed an algorithm to fine-adjust the position of the grating. It takes advantage of the fact that the DC component of the photodiode output is mainly proportional to the CW laser power. We filter it additionally with a self-made 10 Hz low-pass filter and sample with the microcontroller's built-in analog-digital converter (ADC). The one embedded in ESP8266 is not of particularly high quality, but operates sufficiently well for the purpose of DC measurement.

The fine-tuning algorithm operates in two steps. Firstly, it scans the angles around the theoretical optimum and sets the position to the one with maximal optical power. Secondly, a sequence of microsteps follows, of the order of 0.1°, further optimizing the position by trying to maximize the signal value. We tested the algorithm on different wavelengths and it was always converging to the optimal position, so we conclude that it fulfills its requirements, and the mount can be operated fully remotely.

Setup validation

The optical setup of the grating was validated with a Ti:Sapphire laser SolsTiS from MSquared in the absence of the frequency comb. The laser wavelength was tuned in the range from 780 to 900 nm and measured on a HighFinesse wavemeter[9]. For every wavelength, the grating rotation angle was scanned around the theoretical optimal position and the DC signal of the photodiode was measured. For each such passage, a Gaussian curve was fitted to find the angle of peak power. Those angles formed a curve against the laser wavelength that was validated with the theoretical one and showed up to be in 97.6% agreement. An exemplary passage is shown in Fig. 4.11.

The obtained optimal angles ϑ were plotted against the theoretical ones and a linear function was fitted. Its parameters can be interpreted as an indication of the agreement between the theory and the experiment. The free parameter is small compared to the ϑ values, so the constant offset is negligible. The direction coefficient of the linear function, which is a measure of agreement with the theoretical prediction, is almost equal to 1. The residuals show small deviations which may be due to an imperfect alignment of the beam which is not hitting the grating directly on the rotation axis or the grating surface is not placed exactly at the rotation axis of the mount. However, the values of residuals are negligible and do not influence the operation of the setup.

Up to this moment the measurements were made solely using the CW laser. However, due to accurate alignment of the overlap between the Ti:Sapph and the

[9]WS7-60 by HighFinesse

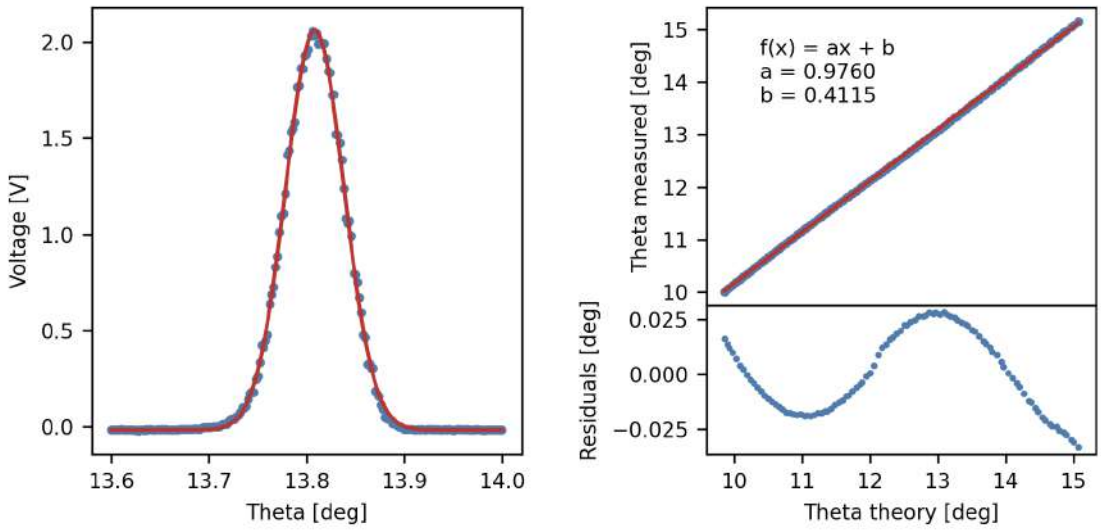

Figure 4.11: Left hand side: Exemplary passage of setup transmission for constant $\lambda = 780\,\text{nm}$ around theoretical optimal grating rotation angle. Fitted function is a Gaussian curve. Right hand side: Comparison between theoretical optimal grating rotation and measured one. Linear function is fitted with negligible offset and direction coefficient close to one, meaning 97.6% agreement between theory and experiment. Below, the fit residuals are plotted showing negligible values.

frequency comb beams, after turning on the comb, we immediately got a beatnote signal with SNR of around 25-30 dB for various wavelengths. From the author's experience, such value is sufficient to lock the beatnote and thus reference the CW laser to the frequency comb.

4.5 Referencing SolsTiS to the frequency comb

Once we had obtained a beatnote between the frequency comb and the SolsTiS laser, we proceeded to construct the electronic setup to lock it. We utilized a phase comparator by Mode-Locked Technology, the same model as with f_{REP} locking, and a STEMLab RedPitaya with open source proportional-integral-derivative (PID) controller[10]. Together, they form a phase-locked loop (PLL), which controls the slow (coarse) and fast (fine) external piezo actuators of the CW laser cavity. The lock

[10]RedPitaya Lock-in+PID, which also can be used as bare PID controller

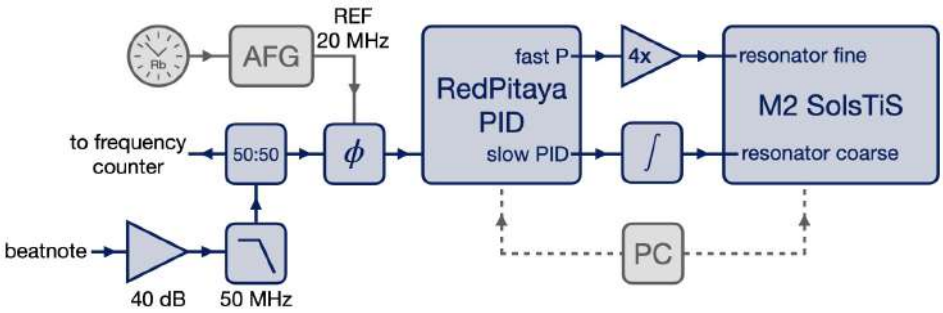

Figure 4.12: Scheme of the SolsTiS lock setup. We used an open source RedPitaya PID to lock the beatnote frequency between frequency comb and SolsTiS to reference 20 MHz. Gray parts correspond to clock sources and PC control.

system scheme is shown in Fig. 4.12.

The beatnote signal is amplified and filtered similarly as in the case of the frequency comb f_{REP} and f_{CEO} lock systems. There is also a 50:50 power splitter that is used as a signal monitor and is connected to the frequency counter setup.

We have also added our RedPitaya expander (see App. B) before the slow actuator and a 4 times amplifier before the fast one to enhance the loop performance. In case of the laser cavity, previously upon reaching the bounds of the RedPitaya output the instability of the lock loop was causing teeth jumps and laser frequency needed adjusting nearly every ten minutes. With our PCB the laser can work on a single frequency for hours.

The function generator used as a source of the RF reference for the lock was synchronized to the same Rb atomic clock as that of the comb lock system. This ensures the phase coherence between all parts of the laser system and increases the accuracy of the lock.

When we locked the laser to the frequency comb, we have observed that although the lock was stable, there were sudden events that caused destabilization of the loop. After a brief investigation, we correlated those events with the switching of the mechanical shutters, which are placed in the light distribution system of the main experiment on the same optical table. Apparently, mechanical vibrations introduced by the shutters switching caused noise spikes in the lock loops.

To dampen the oscillations we bought special vibration dampers[11] consisting of two metal plates with rubber in between. One plate has an M6 screw attached, the other has an M6 thread, making them ideal for mounting shutters and standard

[11]Rubber vibration damper with M6 thread

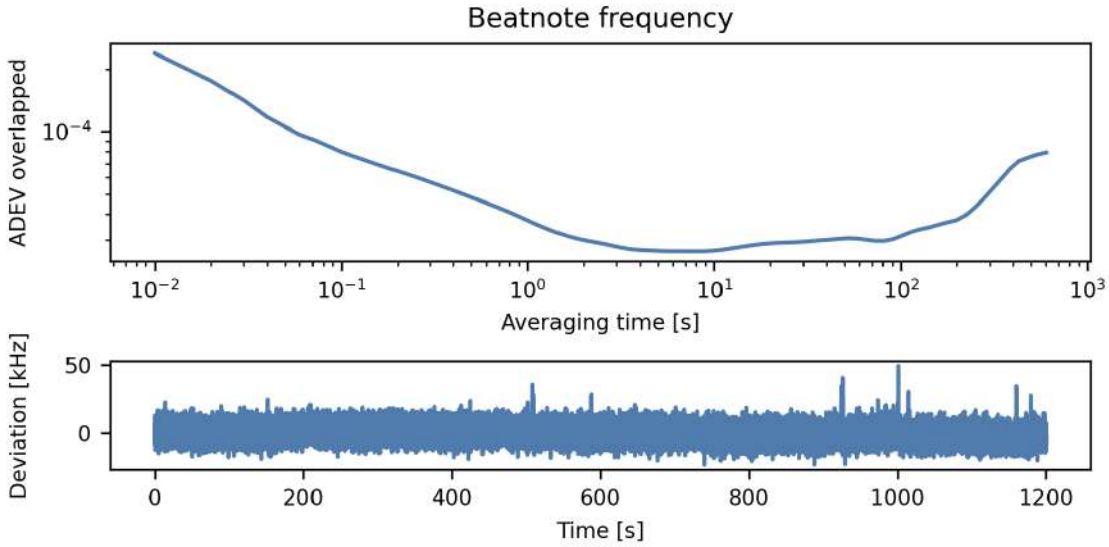

Figure 4.13: Overlapped Allan deviation plot for the SolsTiS referenced to the stabilized frequency comb. The beatnote frequency between the two lasers is shown, which was measured over 20 min with gatetime of 10 ms. Lower panel shows measured frequency as deviation from the average.

optomechanics. The rubber is 1.5 cm thick and has a diameter of 2 cm, just enough to damp the oscillations without wiggling of the whole shutter. We placed those spacers directly underneath the shutters and observed that the vibration problem vanished. Those spacers can also be used to galvanically isolate optical elements, such as battery-powered photodiodes, from the optical table.

Once all technical issues had been resolved, we measured the overlapped Allan deviation, presented in Fig. 4.13, using the frequency counter with gate time of 10 ms over 20 min. The obtained data showed that, with an illumination time of 1 s, we get around 4×10^{-5} of the Allan deviation, which for a typical lock frequency of 20 MHz corresponds to $\approx$ 0.8 kHz of frequency deviation. This dominates the deviations measured for the f_{CEO} and f_{REP} and limits the frequency resolution of our laser system. As we were unable to decrease it by adjusting the lock loops, we believe this is the limit we can achieve with the actuators of the laser. It is also an indirect measure of the laser linewidth, which can be narrowed down to a few kHz by reference to the external cavity, as stated in the laser manual. In our case, the reference is not the cavity, but the frequency comb, so we think that obtained deviation is due to the limit of the laser hardware in terms of linewidth.

A possible extension to fully phase lock the laser to the frequency comb would be to utilize the AOM at the output of the laser's optical setup as a fast phase actuator, however, we found the obtained resolution sufficient for our purposes.

4.6 Server-based architecture

We have developed a server-based architecture as it allows a smooth communication between decentralized devices and does not close the system in a single-purpose application as new request paths may be added upon need. This approach also fits perfectly into the laboratory experiment control and data acquisition systems. The details of each server and the hardware they are controlling will be described in this section.

The architecture is based on object-oriented servers written in Python using the `BaseHTTPRequestHandler` from `http.server` module as the base class. There are 4 servers in total, managing the wavemeter, the frequency counter, the frequency comb, and the MSquared SolsTiS laser. The architecture scheme is shown in Fig. 4.14.

We chose a decentralized approach where each server is a full-fledged entity corresponding to the single device in the system, yet responsible for a minimal set of actions. This architecture is easy to expand with smooth communication capability between smaller parts instead of a single, large script managing every aspect of the system. Due to its decentralized character, any server may work as a part of the architecture or as a standalone device, so if needed it may answer requests from other applications without disturbing the SolsTiS frequency tuning system.

The three main servers (frequency counter, frequency comb and SolsTiS laser) are written in such a way that the main thread handles the server part of the code while an additional thread is added to manage the hardware controlled by a given server. This separates the server and hardware areas of operation, allowing undisturbed handling of clients' requests. The actions induced by the requests are then FIFO queued and applied to hardware in a separate thread.

Wavemeter server

The wavemeter server is the most elementary. It connects to the High-Finesse WS7 wavemeter with a fiber switch expansion and, upon request, responds with the frequency of a given channel back to the client. According to the producer, the accuracy of our wavemeter is around 60 MHz, so it is meant to give a rough estimate of the laser wavelength.

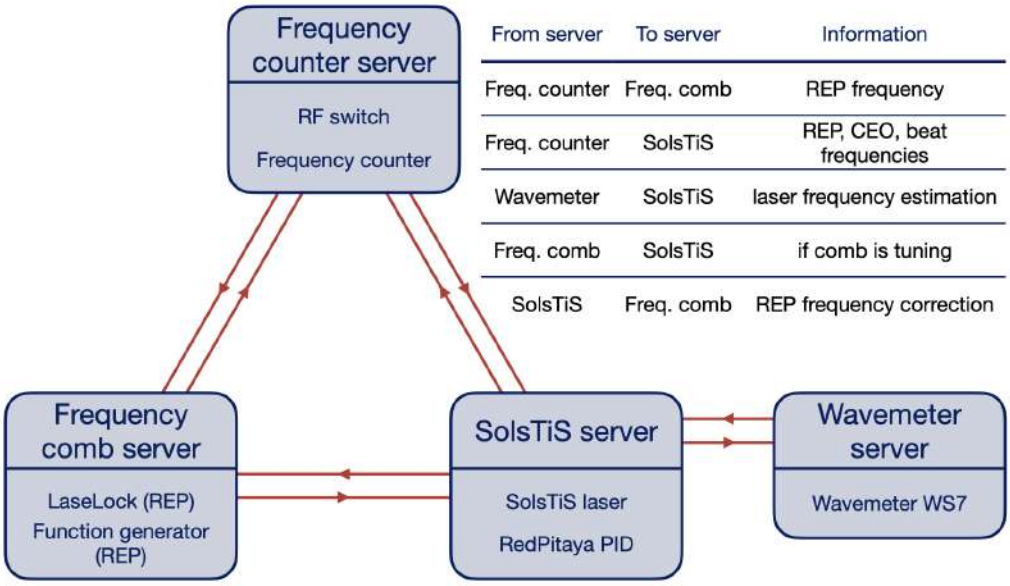

Figure 4.14: Scheme of the server-based architecture. Each block shows a single server in the system with managed hardware listing. Servers communicate with each other with http protocol in a decentralized architecture. Table in the plot shows what information is sent between various server pairs.

The wavemeter is also used by other researchers in the laboratory, which is possible because of the fiber switch expansion. For ease of use, the server hosts a website where the user may choose the channel and get real-time reading of the requested channel anywhere in the laboratory. The server basis is the ideal framework for such a multi-client application.

We have calibrated the wavemeter readout by measuring known atomic transition frequencies using our ECDLs used in K-Cs experiment. We have locked the lasers to various transitions of the Cs D2 line (852 nm) and the ^{39}K D1 line (770 nm) using lock-in detection in saturation spectroscopy experiment. D2 line of ^{39}K is not suitable for this measurement, as the transitions are so dense and indistinguishable that it is not possible to define the locked laser frequency with sufficient certainty. The wavemeter was found to have a constant offset of 110.0(30) MHz, which by coincidence is close to the f_{REP} and the output AOM carrier. The standard deviation of the fit residuals is 15.42 MHz, which we interpret as a measure of the accuracy of the wavemeter, and it is lower than the one stated by the producer. The calibration plot of the

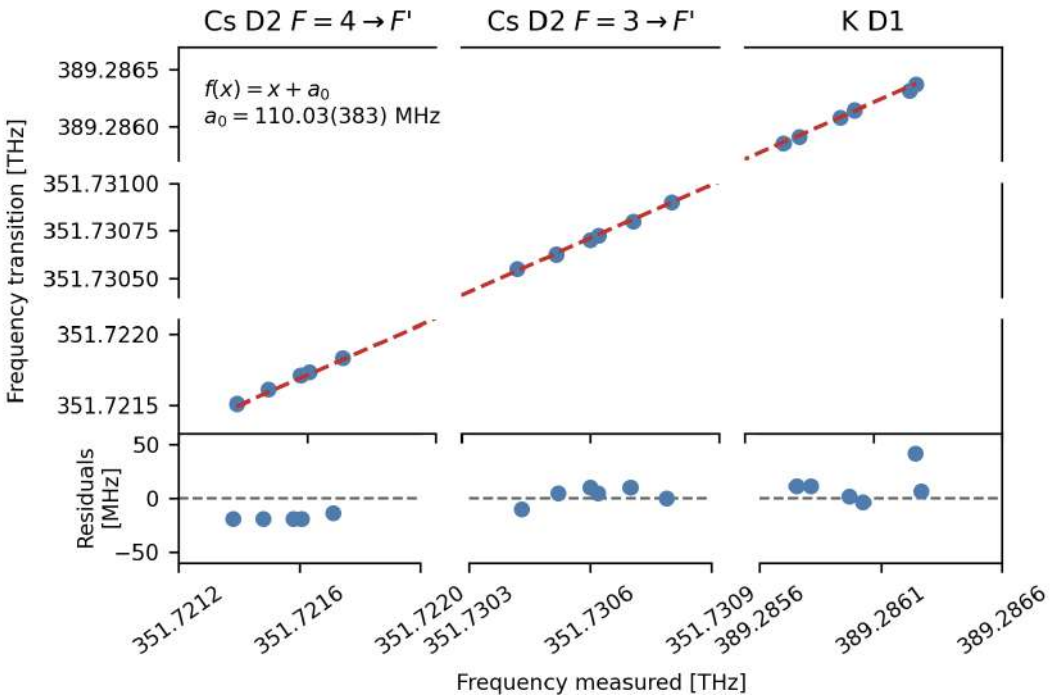

Figure 4.15: Calibration of the wavemeter by measuring frequencies of lasers locked to various Cs and ^{39}K transitions via saturation spectroscopy lock-in method. A constant offset function was chosen as a calibration curve. Lower panel shows the residuals to the fit.

wavemeter is shown in Fig. 4.15.

Frequency counter server

The frequency counter server is responsible for the connection with the frequency counter and an RF switch at its input. Our frequency counter[12] has two input channels, but the whole system requires at least three frequency measurements, namely comb's CEO and repetition frequencies, and the beat frequency. For this reason, we have added a digitally controlled 8-channel RF switch, as input multiplexer. It is controlled by an MCP2221 chip[13], which is a universal serial bus (USB) to general-purpose input/output (GPIO) converter. The scheme of the frequency counter setup

[12]FC53220 Frequency Counter by Keysight
[13]MCP2221 USB to GPIO converter by Adafruit

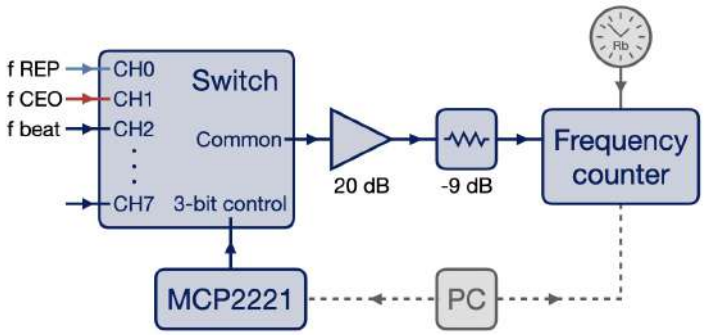

Figure 4.16: Scheme of the frequency counter setup. The 8-channel RF switch HMC253 is controlled by a USB to GPIO converter MCP2221 by a PC. Currently only 3 channels are used leaving the rest 5 free for further extension or other application. Frequency counter is also controlled by the PC and referenced to an atomic Rb clock.

is shown in Fig. 4.16.

The server responds with the frequency of a given channel upon request. There is also a variable gatetime setting implemented. For example, the repetition frequency should be measured with 1 mHz resolution to be considered accurate, which means 1 s gatetime. For other frequencies 1 Hz resolution is enough, so shorter gatetime was chosen. Gatetimes were chosen according to typical frequencies (110 MHz for f_{REP} and $20 - 30$ MHz for other frequencies). The sequenced measurement with these gatetimes limits the refresh rate of the laser frequency estimation but cannot be omitted.

An important feature of this particular system (already mentioned in Sect. 4.3) is that the RF switch when switching between channels causes sudden changes in the impedance of the signal lines. This particular device is a simple evaluation board of Analog Devices 8-channel RF switch HMC253[14] and does not provide impedance matching for closed channels. For this reason, proper channel isolation between switch inputs and lock loops is crucial.

Frequency comb server

The frequency comb server manages the function generator which sets the reference frequency for f_{REP} and the MessTechnik LaseLock PID controller which controls the f_{REP} lock. The f_{CEO} does not need to be changed as it does not take part in the

[14]HMC253 8-channel RF switch by Analog Devices, already obsolete

laser frequency tuning. Also, the RedPitaya PLL, which we have used in the f_{CEO} lock loop, does not have an API that would allow automatic control via a Python script.

The hardware management thread of the server is responsible for monitoring the f_{REP} lock status and automatically initiates a relock sequence if an error is detected. During scanning of the f_{REP}, which results in a proportional scan of the laser frequency, it may happen that it reaches the ranges of the lock setpoint where the loop becomes unstable. The algorithm then unlocks the f_{REP} and allows it to run freely. This natural frequency is measured by the frequency counter request and the reference frequency is set equal. Then, the f_{REP} is locked once again at this new frequency. This may result in a change of the laser frequency to an undesired value, but at the same time restores the full dynamic range of the f_{REP} lock loop. Due to the repetitive property of the comb teeth, the laser may be locked to the desired frequency but on a different tooth number, which is managed by the SolsTiS server. The information about the relock sequence running is sent to the SolsTiS server, so that it does not simultaneously perform any actions, as the readings of the repetition frequency may be defective during relock.

What is more, the server also changes the f_{REP} upon request, which is particularly useful when scanning a SolsTiS laser locked to the comb. Thanks to the multi-threaded architecture we have implemented a linear change between current and new setpoint values with 1 Hz step every 100 ms. Change even of the order of 1 Hz in the RF regime may be dramatic in the optical regime, since the numbering of the teeth is usually of the order of millions. The stepped change of frequency gives the lock loops time to follow the frequency scan, thereby preventing the laser locked to the comb from experiencing teeth jumps.

MSquared SolsTiS laser server

The SolsTiS server manages the SolsTiS controller unit, which takes requests that tune the frequency of the laser. It also connects via secure shell (ssh) to a RedPitaya with an open source PID that is responsible for the lock with respect to the frequency comb.

The main responsibility of the hardware management thread is to keep the laser on setpoint frequency. For this purpose, it continuously monitors the frequencies f_{REP}, f_{CEO} and f_{beat} measured by the frequency counter and the laser frequency estimation from the wavemeter. It also holds information about f_{offset}. From these data, roughly every second (limited by the f_{REP} measurement on the frequency counter), it calculates the current laser frequency and corrects it if needed by adjust-

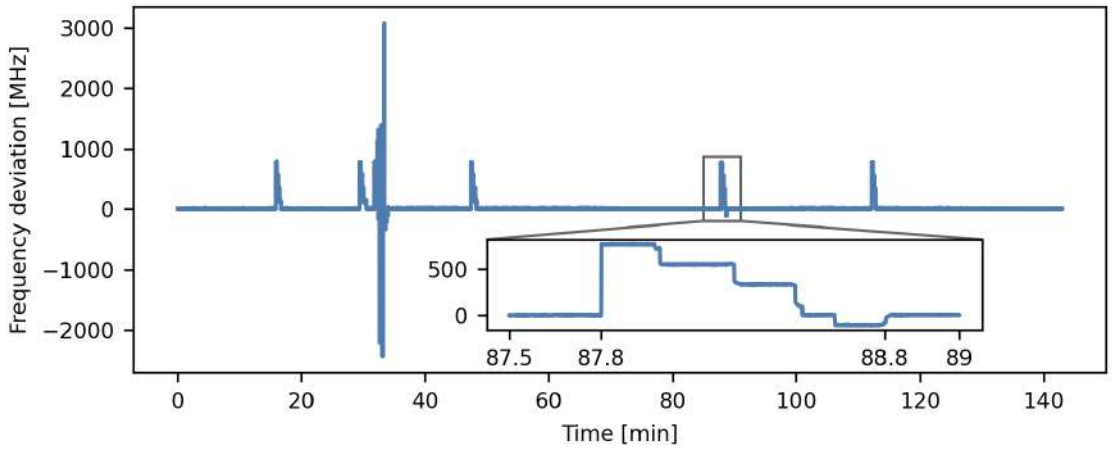

Figure 4.17: Deviation of laser setpoint frequency in a long-term. The smaller fluctuations, also presented in inset are caused by external factors. The large disturbance was caused by delicate shaking of the umbilical cord of the pump laser. The plot shows the operation of the stabilization algorithm, which upon detection of frequency change adjusts the laser frequency back to the setpoint value.

ing the internal actuators of the SolsTiS (the first three layers described in Sect. 4.2). Based on the magnitude of the frequency error, it automatically chooses which actuator to adjust with a proper resolution. Details of the frequency-tuning algorithm will be described in Sect. 4.7.

Apart from the value of the laser frequency, the server also monitors the status of the lock of the laser to the frequency comb. If a high error value is detected, it initiates the relock procedure by unlocking the PID controller, resetting the integral value which might have wound up, and turning the lock on again. This is possible due to an ssh API of the RedPitaya software we are using, which is also one of the reasons why this particular implementation was chosen.

With all the servers running, we performed a stability test, by locking the laser to an arbitrary frequency 351.73090 THz and letting it run for a while. We recorded the data measured by the wavemeter, which we present in Fig. 4.17. In the plot it is visible that during around two and a half hours period the laser fell of the lock five times and the algorithm corrected its frequency back to the locking setpoint within one minute. One of these events is shown in the inset, where subsequent frequency jumps by the f_{REP} are visible, while the laser is tuned back to the setpoint. We also observed that the laser tends to jump to higher frequencies when falling off the lock,

which we interpret as coming from some device-specific reasons. The large fluctuation was induced by delicate shaking of the umbilical cord of the SolsTiS pump to see if the algorithm can withstand stronger disturbance.

The time period in which algorithm returns to the setpoint can be reduced by decreasing the time that is left for laser stabilization between coarse adjustments of the laser cavity performed by the server. We tested this possibility, however, out of precaution regarding stability of the algorithm, stayed with the ones visible in the plot. While working with the laser, we observed that it takes random amount of time for it to jump in frequency upon server cavity correction, so we leave a safe margin, so that frequency calculation is performed on reliable values.

4.7 Frequency readout and tuning

Laser frequency determination

Solely, the beatnote does not give information about the number of the comb tooth with which the laser is beating. To determine it, we need a rough estimation of the laser frequency, which can be done with a wavemeter.

It is crucial that the accuracy of the wavemeter is at least better than half of the teeth separation. In our case, according to the producer, the wavemeter has 60 MHz accuracy and f_{REP} is typically around 110 MHz. These values break the rule of thumb, but based on the measurements of our diode lasers' wavelengths when locked to known atomic transitions, we believe that the accuracy of the wavemeter is actually better, of the order of 20 MHz (see residuals of wavemeter calibration in Fig. 4.15). This means that it is proper to use this particular wavemeter with the comb.

Another important aspect of the system is the fact that our comb is actually a second harmonic of a primary oscillator. The comb frequencies which we lock are the frequencies of the primary comb, however, the output is actually doubled. This does not affect f_{REP}, but f_{CEO} has to be doubled, so the calculations reflect reality.

Further, to determine the frequency of a CW laser ν_{laser}, we need to modify the comb equation by adding the term with the beat frequency f_{beat}:

$$\nu_{laser} = \pm 2 f_{CEO} + n f_{REP} \pm f_{beat} \tag{4.11}$$

where the $\pm$ signs are added in front of f_{CEO} and f_{beat} to indicate that the lock sign needs to be determined. Due to changes on a daily basis in environmental conditions such as temperature and humidity which affect the electronics, it may be sometimes more beneficial to lock to positive or negative loops.

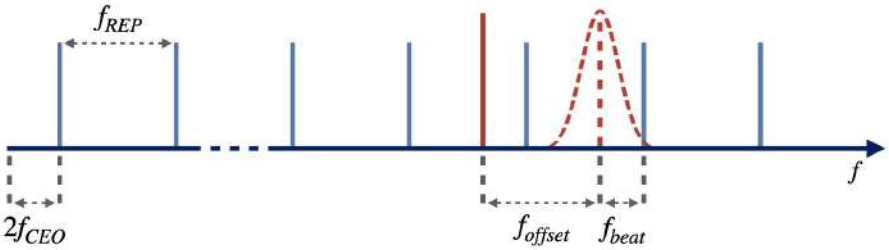

Figure 4.18: Graphical illustration of the frequencies used to determine the laser frequency. Light blue, lower lines represent the comb spectrum. Red, higher lines represent the laser frequency. The dashed red line is the laser frequency measured by the wavemeter and used to obtain the beat signal with the comb. The solid red line is the actual laser frequency shifted by the output AOM. The dashed red gaussian envelope represents the coarse estimation given by the wavemeter. Dashed horizontal line is a large gap in frequency, as f_{CEO} is defined as an offset to the first (hypothetical) tooth from 0 Hz, but the optical spectrum is in the range of millions of teeth numbers.

In case of f_{CEO}, the negative frequency means that the absolute value of the f_{CEO} is higher than $f_{REP}/2$, which also appears as lower frequency, complementary to the f_{REP}. This occurs due to both the method of obtaining the f_{CEO}, as well as the repetitive nature of the comb. We can utilize this lower frequency signal and assign it a negative sign, because the comb spectrum is invariant under the shifts of f_{CEO} by values equal to multiples of f_{REP}.

In case of f_{beat} the positive or negative frequency arises from the fact that the laser frequency may be below or above that of the closest comb's tooth. It can be determined by changing the f_{REP} and observing the beatnote signal while the laser is running freely. We were increasing the f_{REP} and at the same time the f_{beat} was also increasing, which means that we were moving away from the closest tooth. As the tooth was moving upward, we can conclude that in our case we were below the tooth and for laser frequency determination we need to take the f_{beat} with negative sign.

From now on, we will keep the sign of f_{beat} negative. For f_{CEO} we observed that over the course of a few weeks it tends to switch its sign. To account for both cases, we will keep the $\pm$ sign.

First, a coarse estimation of the laser frequency is done with the wavemeter. This

information is used to calculate the tooth number of the lock using the equation:

$$n = \frac{\nu_{WLM} \mp 2f_{CEO} + f_{beat}}{f_{REP}} \tag{4.12}$$

This, of course, returns a real number, so it has to be rounded to the nearest integer. Then, with the tooth number already known, the laser frequency can be estimated. A part of the laser optical setup is an AOM, which is used to turn the laser on and off swiftly and also to control the intensity of the laser light. It only affects the laser light going into the experiment, not the wavemeter nor the comb beatnote paths. As it shifts the light frequency, to compensate for it, we need to add a negative offset frequency f_{offset} as we utilize the -1st diffraction order. As described in Sect. 4.2, the acousto-optic effect depends on the wavelength of the laser. Therefore, when the wavelength of the laser is tuned, the offset frequency must be adjusted so that the light can be properly coupled into the output fiber. We have used our calibration curve to determine the frequency shift of the output light and included it in our calculations. The modified and final equation for determination of the laser frequency locked to the frequency comb is:

$$\nu_{laser} = \pm 2f_{CEO} + nf_{REP} - f_{beat} - f_{offset} \tag{4.13}$$

The graphical illustration of the frequencies used to determine laser frequency and their relations is shown in Fig. 4.18.

Frequency tuning

Frequency tuning starts with a request sent to the SolsTiS server which changes the setpoint frequency. The server calculates the tooth number closest to the new frequency assuming that there is no change in f_{REP}. Then it calculates a new f_{REP} based on the tooth number. At first sight, it may seem like an unnecessarily looped procedure, however, it actually gives the smallest f_{REP} correction, still resulting in a proper frequency lock. Minimal changes in the value of the f_{REP} help to keep it within the dynamic range of the comb lock loop. The corrected f_{REP} is sent to the comb server to be set, which changes the spectrum of the comb according to Eq. 4.7.

The laser, still locked to the comb, follows the frequency shift due to f_{REP} correction. As stated earlier, this change is not instantaneous, but linear in time, which lets the laser lock loop follow the moving tooth of the comb. If the frequency change is smaller than a set threshold, correction resulting from f_{REP} change is sufficient, and the laser settles on the new frequency, locked with respect to the *same* tooth number.

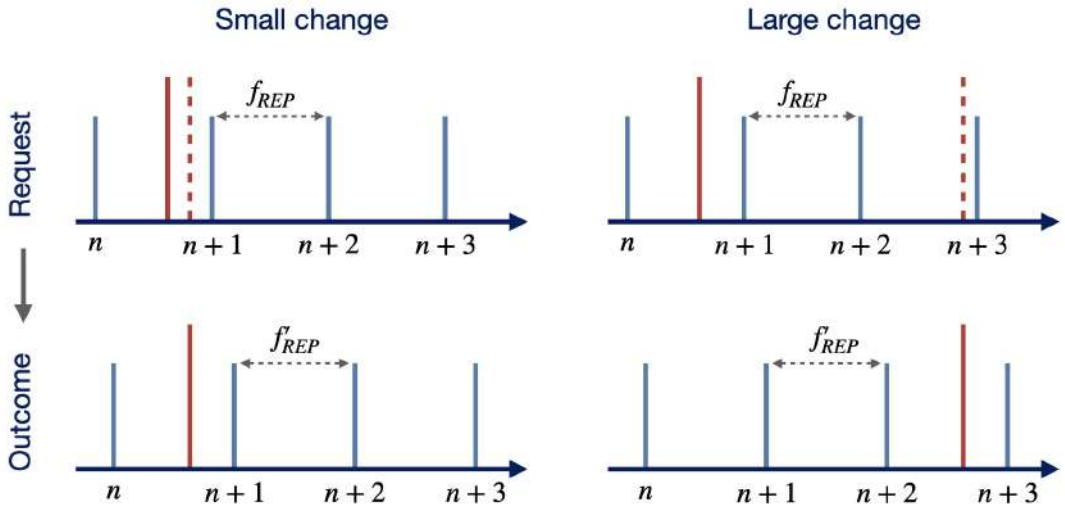

Figure 4.19: Graphical illustration of the frequency tuning algorithm in two cases, small and large frequency change. Lower, light blue lines represent the comb spectrum. Higher, red lines represent the laser frequency. Dashed red lines in upper panels show the new requested laser frequency setpoint. In both cases algorithm corrects the f_{REP} by the same value which changes the frequency comb spectrum according to new f'_{REP}. Left hand side: when frequency change is small algorithm does not move any SolsTiS actuators and RedPitaya PID locks the laser with respect to the same tooth number within the new comb spectrum (in here $n+1$). Right hand side: when frequency change is large, algorithm also changes the SolsTiS actuators and RedPitaya PID locks the laser with respect to another tooth number within the new comb spectrum (in here $n+3$).

It may happen that the user wants to make a bigger jump in frequency. Then, the algorithm still makes the smallest change in f_{REP}, but the larger laser frequency step is managed by the internal SolsTiS actuators. When the laser light approaches the desired setpoint, the Redpitaya PID locks on the correct position, with respect to *another* tooth number. The graphical illustration of both cases is shown in Fig. 4.19.

The variable that the algorithm focuses on setting is the absolute laser frequency, rather than a specific f_{REP} or n. This implementation of the laser system has the advantage of keeping the comb lock setup in its dynamic range by minimizing changes in the f_{REP}. This also minimizes the chances of the destabilization of the system because chaotic movements in the f_{REP} have dramatic results in the optical range, due to multiplication by n of the order of millions.

We have added request paths to both the frequency counter and the wavemeter servers. When these are called, they measure and send data for timetagging and storage alongside other data (like atomic cloud images or oscilloscope readings). In this way, in each iteration of the experimental sequence, all of the information required to retrieve the laser frequency is saved.

Summary

The laser system presented in this chapter provides a server-based architecture to lock the SolsTis laser on absolute frequency with respect to the frequency comb fully automatically.

It was designed, implemented, and optimized with the idea of minimizing user involvement and chooses appropriate actions to set the laser frequency with a frequency tuning algorithm. By implementation, it minimizes the chance of system destabilization and corrects any errors detected in the real-time monitored frequencies.

The system also provides request paths to store information needed for laser frequency retrieval in data post-processing, suited for the experiment control and data acquisition architecture used in the laboratory. All frequency references are synchronized with an atomic Rb clock to increase the accuracy of the frequency lock.

It is important to note that the algorithm is general in a way that it is not tied to a particular Ti:sapphire laser or frequency comb. The only requirement is that the laser can be operated remotely with sufficient frequency resolution. Most commercial lasers have ways of external tuning by managing different laser actuators, so if needed, an additional layer of remotely controlled DACs can be added in the SolsTiS server implementation. The system is also easy to expand to additional lasers locked to the same frequency comb.

The performed tests provided data showing an amazing stability and tunability, ensuring that the system is ready for precise, state-of-the-art spectroscopic measurements.

Chapter 5

Noise suppression in long-distance optical frequency transfer

This chapter will describe a system for residual noise suppression in a long-distance optical frequency transfer. During the PhD research period, I was involved in a project under grant Polish Metrology financed by the Ministry of Education and Science. It was focused on the transfer of optical atomic clock reference over large distances, which is strictly connected with high-precision spectroscopy and, as such, fits within the frames of this dissertation.

The system presented here was developed in a consortium between AGH University of Science and Technology (laser recovery modules and general scheme of the system), Jagiellonian University (optical setup of the cavity), Nicolaus Copernicus University (access to optical atomic clock reference and venue) and University of Warsaw (digital servo for drift cancellation). This chapter will describe the whole system and this author's contribution, which is detailed in Sect. 5.3.

5.1 Long-range optical frequency transfer

The optical transfer of information has become both commercially available (due to the development of cost-effective technologies) and inevitable (due to growing demand in data transfer rate). It gives scientists the opportunity to use commercial fiber networks that span across countries in research [127], just to mention the quantum key distribution [128, 129] or transfer of the optical atomic clock frequency [130, 131]. The latter has a particular research application of providing a time reference with the highest accuracy available.

A few years ago, there was a redefinition of the SI base units, which are now derived from physical constants, yet the time unit still refers to the hyperfine splitting of the ground state ($6S_{1/2}$) of cesium and as such needs to be measured. This choice was dictated by the fact that optical frequency is an observable that humanity can measure with the highest accuracy. As a consequence of the unit redefinition, we can refer other units to a second by physical constants, not by comparison with a one-and-only unit standard [132]. Optical atomic clocks are now built and developed in multiple laboratories and may serve as an absolute time reference for other researchers when transferred via a fiber network.

Long-distance optical frequency transfer, although flawlessly exploited, for example, in internet broadcasting, has drawbacks when used in scientific applications. Namely, the noise induced by coupling with the environment, which is not a stable, isolated physical laboratory, can make the frequency information unusable. For this reason various scenarios of noise cancellation are introduced, one of the most popular being retro-propagation of the laser light [12, 11, 133].

In this technique, another fiber in the same cable is used as noise reference, where a laser beam is propagated from the transmitter to the receiver, there it is back-reflected and follows the same path to the transmitter, where it is beated with the input. The assumption is that laser noise is common for both beams and thus cancels, but the noise acquired on the long distance can be measured and suppressed in the actual frequency signal. This method has a major constraint. The speed of light is enormous, yet finite, so it takes the light a non-negligible amount of time to travel both ways. This sets an upper bound on the noise spectrum, as frequencies above certain threshold cannot be measured properly due to the intrinsic delay in the stabilization loop [10]. Active feedback stabilization methods require then additional hardware on the receiver side. In this chapter, a novel approach to this problem is presented, which we call a clean-up system.

5.2 Architecture of the clean-up system

The idea behind the architecture of the system relies on two components, the transferred optical atomic clock reference, and the local laser stabilized to an Ultra-Low Expansion (ULE) cavity. The heuristic explanation is the following. In a sense, the architecture is designed to retain only the desirable properties of both components while discarding the unwanted ones, thus allowing them to complement each other. This will be described in detail in this section.

The frequency standard, when transferred over large distances, is blurred due to

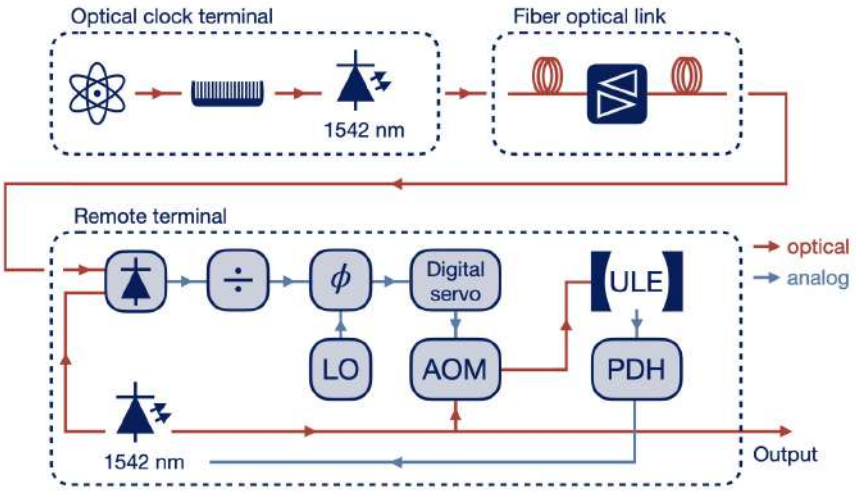

Figure 5.1: Scheme of the long-distance optical frequency transfer. At the local terminal the optical atomic clock signal is translated to the telecom regime using a frequency comb. Then the signal is transferred via a long-haul fiber optical link with optical amplifiers. In the remote terminal the clock frequency is restored using the clean-up system.

high-frequency noise. However, if integrated with high time constant, the average is still defined with high accuracy. This provides a stable reference frequency on large timescales, but has a drawback of unwanted noise on shorter ones.

On the other hand, the laser stabilized to an ULE cavity provides an excellent stability when it comes to high-frequency noise, yet exhibits a slow cavity drift. This provides a well-defined laser frequency, but the average is moving over time. It should be noted that this drift can be stabilized with a feedforward approach because it is usually constant over extended periods of time (it comes from slow cavity material deterioration). However, it is less reliable than an active stabilization approach and is not autonomous as it needs to be verified every now and then.

It is clearly visible that both components have complementing advantages and disadvantages. We have designed a digital servo as a distinctive bridge between the two, which aims to reproduce the frequency standard, as this is the ultimate goal of the whole system.

The architecture, shown in Fig. 5.1, begins on the transmitter side, where an optical frequency signal coming from an optical atomic clock is translated through a frequency comb into the telecom range at 1542 nm. Then it can be transmitted through a fiber link in a commercial network and arrive at the remote terminal. Both

ends of the fiber link are connected to the laser regeneration stations, which perform the aforementioned retro-propagation stabilization of the signal.

The light source of the clean-up system is an external cavity semiconductor laser (ECL) operating at 1542 nm. A part of the light goes through an AOM in a double-pass configuration. For clarity, for now, we will assume that it operates at constant carrier frequency 150 MHz. Then it is coupled to an ULE cavity of 12 cm length. Transmission through the cavity is stabilized by a Pound-Drever-Hall (PDH) method that effectively binds the laser frequency to the cavity mode. The cavity is kept at a temperature equal to its zero thermal expansion point to minimize drift.

At the same time, the ECL is beated on a photodiode with the transferred optical clock signal coming from the regeneration station. This produces a beatnote which carries information about the frequency difference between the local ECL and the frequency standard. The beatnote is compared with a local oscillator, providing a phase error signal between the two lasers, the local and the transferred one. We have built a custom digital servo to stabilize the phase difference by applying the correction to the aforementioned AOM carrier frequency. This shifts the frequency of light coupled to the ULE cavity, and the correction further propagates through the PDH algorithm, finally correcting the ECL frequency. In this way, in a sense, we deceive the PDH loop about the actual frequency of the laser and perform an offset lock.

The crucial point to note is that the servo has a sub-Hertz transfer function, so it can filter the super-Hertz noise spectrum. Then, it is not imprinted on the ECL, retaining the stability provided by the ULE cavity. At the same time, the slow drift of the cavity is corrected on the basis of comparison with the stable, averaged frequency of the transferred standard.

5.3 Drift servo

The digital drift servo, which design and construction was my part of the whole project, consists of four functional parts forming a controller and an interface. The scheme of the servo system is shown in Fig. 5.2.

We chose a digital approach which provides an unparalleled resolution of the direct digital synthesizer (DDS). In addition, the transmittance of the loop filter programmed on a microcontroller can be shaped with much higher flexibility than in an analog approach. The loop elements can be adjusted according to a specific application without the need to compensate for parasitic impedance. As the microcontroller is easily reprogrammable, this solution gives the opportunity to change the

design of the filter based on the system response, whereas with the analog approach a new hardware would have to be developed from the beginning.

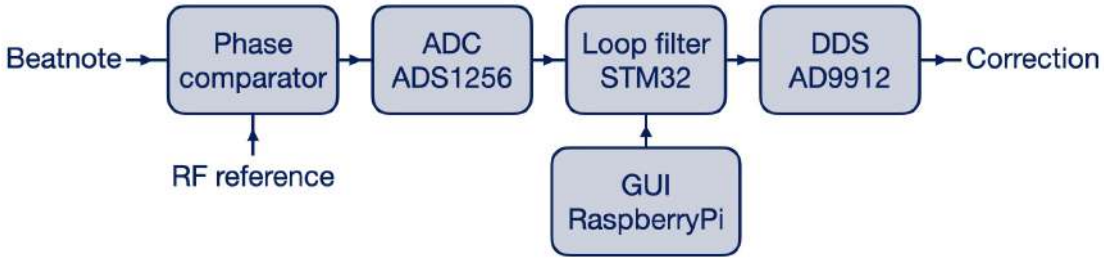

Figure 5.2: Scheme of the servo. Incoming beatnote signal is compared with RF reference on a phase comparator which returns an analog signal. It is measured on ADC and read out by STM32 microcontroller which calculates error and control signals according to the loop filter settings. It also controls a DDS which sends a correction signal to the AOM. Microcontroller is controlled by a GUI written in Python, running on a RaspberryPi

The first element of the servo is the phase comparator, provided by the AGH group, which compares the beatnote signal with an RF reference and returns an analog signal corresponding to the phase difference between the two. It is digitized by an analog-to-digital converter (ADC) to be further processed. We used an evaluation board of 24-bit ADS1256[1] from Texas Instruments, which has a sampling frequency of up to 30 kHz. The ADC parameters are sufficient for the servo purpose considering the loop bandwidth and required resolution. We sample the ADC at 2 kHz, as this is three orders of magnitude higher than the required loop bandwidth, providing an anti-aliasing, yet still leaving plenty of time for loop calculations. At the same same, this piece of hardware is not expensive compared to some high frequency ADCs.

The phase error signal is further processed by the STM32 H743ZI[2] microcontroller, where the loop filter is implemented, the scheme shown in Fig. 5.3. Firstly, the error is multiplied by the total gain factor filter. Due to the linearity of all of the operations, it is further propagated through all of the calculations.

The main part of the filter comprises three operations, the proportional, the integral and the double integral components, each with its own distinctive gain factor, realizing a PI^2 stabilization scheme. The sum of these is followed by two optional lowpass filters with variable cutoff frequency. They are implemented as first-order

[1] ADC1256 ADC by Texas Instruments
[2] STM32 H743ZI microcontroller with ethernet by STM32

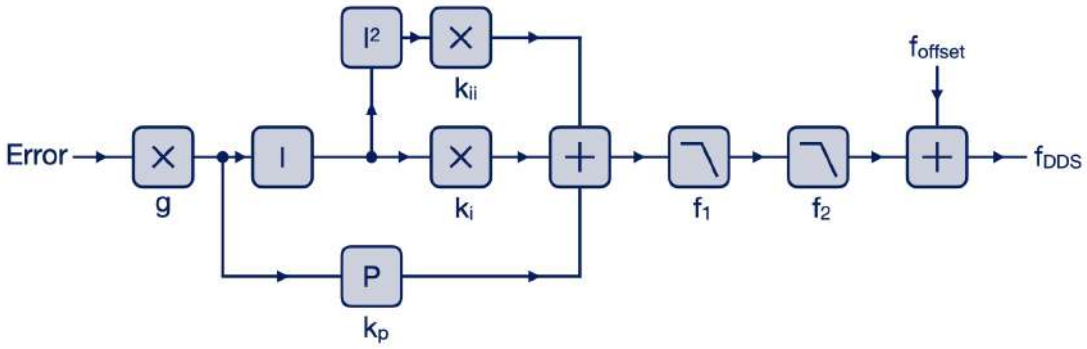

Figure 5.3: Scheme of the loop filter. The error is multiplied by filter total gain factor g. Then three calculations are performed: an integral and optional double integral with gains k_i and k_{ii} respectively and a proportional part with gain k_p. All three components are summed and optional lowpass filters may be applied. Last summation adds an offset frequency, so filter operates mostly around zero.

Butterworth type Infinite-Impulse-Response (IIR) filters. This algorithm has the advantage of low computational cost, which is important in real-time digital systems. Furthermore, the Butterworth type has a flat transmission band, which does not induce distortions in the processed signal.

The last element of the filter is summation with a constant offset frequency equal to the carrier of the AOM. This ensures that the PI^2 part operates mostly around zero. It also reduces the time required to reach the steady state, since the integral components acquire the offset slowly, as the bandwidth of the filter is low.

The computed control signal is then sent to the DDS which controls the AOM carrier frequency. We chose the AD9912 evaluation board[3] by Analog Devices, provided by the Nicolaus Copernicus University group. The AOM shifts the frequency of the laser beam passing through it, imprinting the correction calculated by the loop onto the light.

An additional part, which functions as a user interface, is a RaspberryPi 4B minicomputer, which communicates with the microcontroller and sets all the parameters of the servo. All communication in the system is done via SPI interface, commands sent by RaspberryPi are parsed by the microcontroller and either applied directly to the loop filter software, or sent further to the ADC or DDS. We have written a graphical user interface (GUI) in Python that runs on the RaspberryPi, to make the usage of the system more user-friendly.

[3]AD9912 DDS evaluation board by Analog Devices

5.4 Servo operation

In this section, we will describe the tests conducted with the servo. Of many, we chose two experiments performed prior to the installation in the system architecture, namely the measurement of the following band and the stability measurement in a short loop. We also present one of the final results, the stability of the long-link frequency transfer for different servo locking bandwidths.

Following band measurement

The first test we conducted was to measure the following band of the servo and verify that it operates in the sub-Hertz region.

For this purpose, we closed the loop of the servo without any additional elements, directly connecting the DDS output to the phase comparator input. Then, we drove the servo in closed loop with a local oscillator (LO) RF signal at 100 MHz modulated in frequency with deviation of 10 kHz and varied the modulation frequency.

We also decoupled the RF signals under investigation, in particular the DDS clock and the local oscillator signals were coming from different arbitrary function generators (AFG). This ensured us that the only stabilization of the servo output that we observed came from the servo operation solely, not from a synchronization effect, which could disturb the results.

We have connected an external phase comparator that measured the phase difference between the LO driving the servo and the servo output. The frequency modulation that we induced was also visible in the phase measurement, since the phase is the integral of the frequency. We have observed the external phase comparator output on the oscilloscope, which provided us with information about the servo following the modulation. When the signal was locked, the output was constant, as the servo modulated its output according to the input signal. Upon increasing the modulation frequency, we observed an increase in the phase comparator signal amplitude as the servo did not keep up with the modulation. At some point, the output signal reached a plateau, which meant that we were out of the following band of the servo.

We fitted a sine function with phase offset to the data collected from the oscilloscope, in accordance with a sinusoidal modulation, and extracted the parameter corresponding to the amplitude of the signal. For each modulation frequency, we ensured that the timebase was chosen such that we measured at least 3 periods of the modulation. This is generally a good experimental practice in oscilloscope measurements of system responses to harmonic signals.

The results of this measurement are shown in Fig. 5.4. For the chosen loop filter

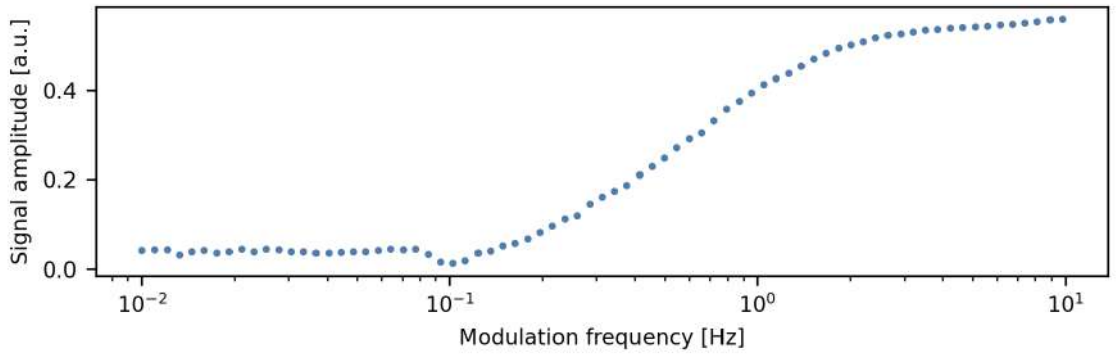

Figure 5.4: Following band of the servo. Small signal amplitude means that the servo is following the modulation induced on local oscillator. The signal does not drop to zero, because of the phase noise amplitude. Rising signal amplitude is the region where servo bandwidth drops. Plateau above 1 Hz is the region where servo is out of the following band and does not keep up with the LO modulation.

parameters we observed that the servo was indeed operating below 1 Hz with the cutoff frequency around 0.5 Hz.

Allan deviation in short loop

Another measurement we performed was verification that the stability of the frequency is improved when the servo is operating. For this purpose, we measured the output frequency of the servo on the frequency counter with the servo turned off and on for a period of half an hour. From the data, we calculated the overlapped Allan deviation, which we present in Fig. 5.5. The choice of the Allan deviation as frequency stability estimate is discussed in Sect. 4.1.

In this measurement, the LO was constant at 100 MHz. We synchronized the function generator that gives the LO signal and the frequency counter with our Rb atomic clock to avoid relative oscillator drifts in the measured data. The generator producing the DDS clock signal was not synchronized for the reason stated in the previous subsection.

We have observed an improvement of at least an order of magnitude between the two cases (servo off and on). The absolute value of the deviation is limited in our case by the accuracy of the Rb atomic clock we have used.

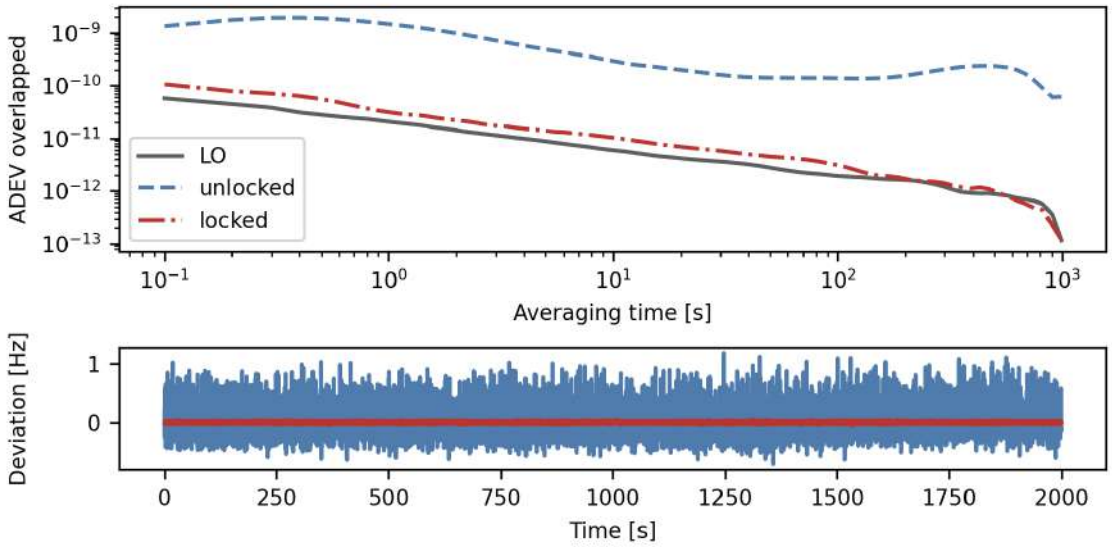

Figure 5.5: Allan deviation of the servo output in a short loop (DDS output directly connected to phase comparator input). The unlocked and locked cases are shown. The LO curve represents the noise baseline, limited by the accuracy of the atomic Rb clock used as the absolute frequency reference. Lower panel shows the deviation from the central frequency $f_0 = 100\,\mathrm{MHz}$.

Allan deviation in the final system

In the final experiment, the entire clean-up system was assembled, and an experiment was performed with a real outdoor fiber of approximately 650 km length. As the local frequency source, a fiber laser (Koheras Adjustic by NKT) was utilized, stabilized to a 10 cm ULE cavity, with feedforward drift cancellation. Although the project is centered around the optical atomic clock transfer, the experiment was rather a proof of concept, and this choice simplified the setup, still giving a reliable frequency source.

Both ends of the long-haul link were terminated with laser regeneration stations performing the standard phase-noise cancellation scheme by retro-propagation. This reduced the phase noise imposed by the long link, yet left the residual high-frequency noise. Both terminals were located in the same laboratory KL FAMO in Nicolaus Copernicus University.

The remote laser system was locked to the remote terminal and the clean-up system was engaged with locking bandwidth around 1 Hz. All additional fiber paths

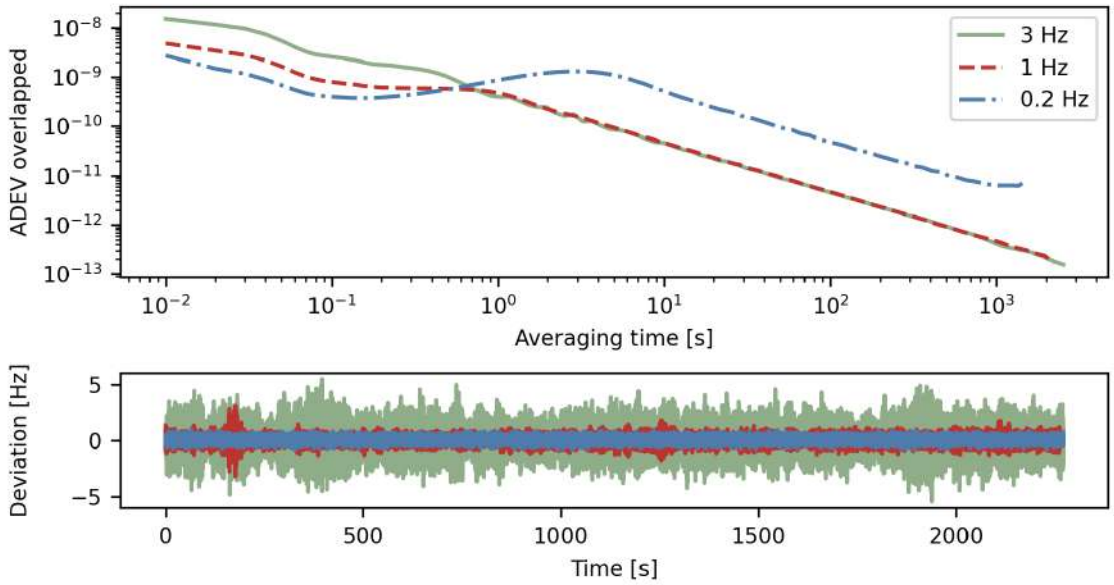

Figure 5.6: Allan deviation of the beatnote between the local and remote terminals. Different curves correspond to the different servo bandwidths settings. Lower panel shows the deviation from the central frequency $f_0 = 61.66\,\mathrm{MHz}$.

used in the experiment were stabilized, and we assume that all of the phase noise is canceled, the only contribution being the long link.

We measured the beatnote between the local reference laser and the remote clean-up output and calculated the Allan deviation for different lock bandwidths. We present the results in Fig. 5.6 with three data sets for bandwidths 0.2, 1, and 3 Hz. The first two cases showed similar results with the 1 Hz bandwidth operating slightly better at low averaging times. The 3 Hz bandwidth case, although excelling in the low τ region, was much worse as the averaging time increased. We interpret this as weaker suppression of the cavity noise. The data shows, as expected, that by varying the locking bandwidth of the servo, one may either improve the residual noise suppression by sacrificing the cavity noise cancellation or *vice versa*.

The beatnote was measured in the RF domain, however, when translating the outcome to the optical domain, we gain a six orders of magnitude improvement of the Allan deviation. This is because the absolute frequency deviation stays the same but is divided by a much higher optical frequency of the laser light. If recalculated, the results are 8×10^{-17} at 10 s and 2.5×10^{-19} at 1000 s which shows excellent performance for transferring stability of the state-of-the-art optical atomic clocks.

Chapter 6

Photoionization of excited states of cesium and potassium

In recent times, I was involved in a new project that started in our laboratory, which aims to produce KAg and CsAg molecules. I was responsible for the measurement of the photoionization cross section of the $P_{3/2}$ states in cesium and potassium caused by the silver MOT light. Firstly, I will describe the motivation for this measurement and then move on to the theoretical part. Further, I will describe the experimental setup and measurement procedures. I will also discuss additional results of light-induced atomic desorption (LIAD) caused by the silver light. Finally, I will present the experimental results and theoretical analysis that enabled the determination of the photoionization cross section of the $P_{3/2}$ in cesium and potassium.

The first Ag MOT was reported in 2000 [134], however, this line of research was not explored beyond this initial demonstration. One can only hypothesize what the reasons were behind not pursuing further studies in this direction. It is likely that it might have been influenced by the challenges that silver presents to experimentalists in particular the need to use cooling light at 328 nm, where high power laser sources have not been available until very recently.

Nevertheless, in recent years, the focus on the community has once again been put on silver, due to theoretical proposals regarding the Ag-alkali dimers [19], which state that such molecules have enormous static dipole moments, compared to the alkali dimers. This revived the research on silver and several groups like the David DeMille group and the Zoe Yan lab from the University of Chicago focused the spotlight on this element. Our group also started the construction of a new apparatus with the aim to obtain the KAg and CsAg molecules.

The high energy of 328 nm photons raises a concern about a possible photoioniza-

tion of alkalis in a MOT. The issue has been also reported for the Sr-Rb mixture [135] and Hg-Rb mixture [136]. Recently, a decrease of the number of magneto-optically trapped potassium atoms in the presence of a silver cooling beam was reported [137] and assigned to the photoionization.

Photoionization as a phenomenon was studied for cesium [138, 139] and potassium [140, 141] but the motivation of these works differed from ours. It is essential to study the influence of silver trapping light on the alkalis to design proper and optimal loading strategies before the construction of the vacuum system.

6.1 Photoionization in a magneto-optical trap

Atoms that are illuminated with a laser beam consisting of photons with energy higher than the ionization threshold are excited to the continuum state. This, effectively, breaks an atom into a positive ion and an electron, depositing some kinetic energy into the products. From the point of view of the loading dynamics of the magneto-optical trap, this can be considered as an additional loss mechanism. Assuming a single-photon process and neglecting the saturation effect, the loss rate γ_{PI} is given as [142]:

$$\gamma_{PI} = \frac{\sigma_{PI} I_{PI}}{h\nu_{PI}}, \tag{6.1}$$

where σ_{PI} is the photoionization cross section, I_{PI} is the intensity of the photoionizing beam, and ν_{PI} is its frequency. Similarly to the loss rates in the MOT rate equation, it is expressed in atoms per second. In principle, the cross section can be different for the ground and excited states, which can be accommodated as:

$$\gamma_{PI} = \sum_{i \in \{g,e\}} \Pi^{(i)} \frac{\sigma_{PI}^{(i)} I_{PI}}{h\nu_{PI}} \tag{6.2}$$

where $\Pi^{(g)/(e)}$ is the fraction of the population in the ground or excited state, with a constraint $\Pi^{(g)} + \Pi^{(e)} = 1$. In here we take into account only the fine structure, as the hyperfine splitting is negligible in comparison to the energy required to ionize the atom.

The additional loss factor coming from photoionization has to be included when analyzing the MOT dynamics. In the high-density approximation (see Sect. 2.3) the effective loss rate is therefore given as:

$$\gamma_t = \gamma + \gamma_{PI} = \gamma_{BG} + \beta\bar{n} + \gamma_{PI} \tag{6.3}$$

and the MOT rate equation reads:

$$\dot{N} = R(I_{PI}) - (\gamma + \gamma_{PI})N \tag{6.4}$$

where we included a possible modification of the loading rate R due to the presence of the photoionizing beam. In the literature, it has been discussed that the relation between the loading rate and the loss rate by photoionization is exponential, $R(I_{PI}) \propto \exp(-\tau_{PI}\gamma_{PI})$,where τ_{PI} is the time that atom travels through the cross section of the ionizing beam [44].

Fraction of atoms in the excited state

For a deeper understanding of the photoionization phenomenon, we wrote a simulation in Python that solves the optical Bloch equations (OBE) of a 4-level system by numerical propagation. We included two hyperfine ground states and two excited states, coupled by two laser beams as in the MOT scheme (see Fig. 3.5). The simulation propagates a set of ordinary differential equations (ODE) using the Dormand-Prince algorithm, a member of the Runge-Kutta family, which is described in detail in App. A.

Optical Bloch equations come from the density matrix approach, where the time evolution of the system is described by a master equation [143]:

$$\frac{\partial}{\partial t}\hat{\rho} = -\frac{i}{\hbar}\left[\hat{H}, \hat{\rho}\right] + \mathfrak{L}(\hat{\rho}), \tag{6.5}$$

where we included the Lindblad operator $\mathfrak{L}$ to account for dissipation in the system, such as spontaneous emission [73, 143]. This equation leads to a set of differential equations for the elements of the density matrix, under rotating wave approximation (RWA). The derived equations in explicit form are presented in App. C.

We solved the OBE with intensities and detunings of the cooler and repumper beams as in our cesium and potassium MOTs, without the ionizing beam, which allowed us to estimate the fraction of the atoms in the ground and excited states. It also confirmed that the species under investigation behave utterly differently. In the case of cesium, because of a large hyperfine splitting compared to the natural linewidth, it can be approximated as a two-level system, as the repumper ground state is nearly depleted. On the other hand, in the case of potassium, the off-resonant couplings are much stronger and the population distribution in the ground state is around 60:40.

The initial population in the simulation was chosen as evenly distributed between both ground states. We also verified that for different initial ratios the outcome in the steady state is unchanged.

For visual clarity, we label the hyperfine states as follows:

- $|g_R\rangle$: $6^2S_{1/2}F = 3$ for cesium and $4^2S_{1/2}F = 1$ for potassium 39
- $|g_C\rangle$: $6^2S_{1/2}F = 4$ for cesium and $4^2S_{1/2}F = 2$ for potassium 39
- $|e_R\rangle$: $6^2P_{3/2}F' = 4$ for cesium and $4^2P_{3/2}F' = 2$ for potassium 39
- $|e_C\rangle$: $6^2P_{3/2}F' = 5$ for cesium and $4^2P_{3/2}F' = 3$ for potassium 39

We propagated the OBE for a period equal to 400 lifetimes of the excited state, when the population balance is established. This period lasts around 12.2 μs for cesium and 10.6 μs for potassium, so it is almost instantaneous compared to the MOT loading, which takes around 10 s. We extracted the occupation factors from the simulated curves by taking the last values of the propagated density matrix, where a steady state is reached. These results are presented in Fig. 6.1 and Tab. 6.1.

Species	$\|g_R\rangle$	$\|g_C\rangle$	$\|e_R\rangle$	$\|e_C\rangle$	$\|e_R\rangle + \|e_C\rangle$
Cs	2.04%	85.31%	0.68%	12.58%	13.26%
^{39}K	60.11%	34.95%	3.36%	1.58%	4.94%

Table 6.1: Simulation results for the steady state occupation factors in a MOT.

Another approach to estimate the fraction of excited atoms is to use the scattering theory, from which we get the explicit formula for a single beam excitation [144, 84]:

$$\Pi^{(e)} = \frac{1}{2}\frac{\Omega^2/2}{\Delta^2 + \Gamma^2/4 + \Omega^2/2} \tag{6.6}$$

where the Rabi frequency Ω is related with the intensity as [84]:

$$\frac{I}{I_{sat}} = 2\left(\frac{\Omega}{\Gamma}\right)^2 \tag{6.7}$$

With this formula, for the parameters as in the simulation, we get estimates $\Pi^{(e)} = 12.9\%$ for cesium and $\Pi^{(e)} = 4.3\%$ for potassium, which are slightly underestimated compared to the previous approach. This is because scattering theory does not include the off-resonant coupling and the influence of the repumper, which, especially in the case of potassium, are not negligible.

Both models do not take into account the influence of the magnetic field and the corresponding Zeeman shifts. In addition, Eq. 6.6 is perfectly valid only for cesium, which has large hyperfine splitting. In the case of potassium, the excited states can exhibit significant off-resonant coupling from both the cooling and repumping beams.

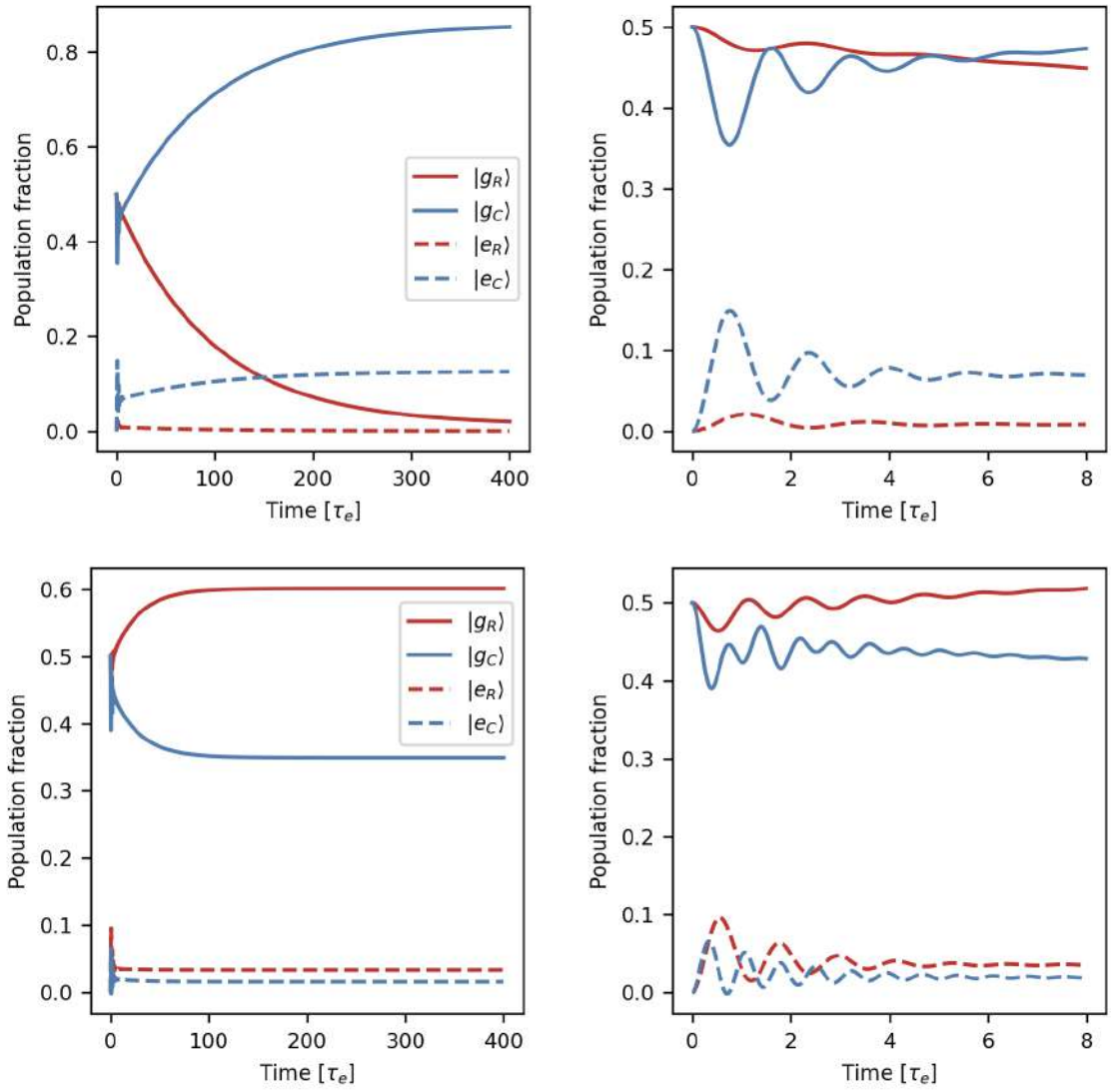

Figure 6.1: Simulation results for the population evolution in the magneto-optical trap for cesium (top plots) and potassium (bottom plots). Blue (red) lines correspond to the states coupled by cooler (repumper). Solid (dashed) lines represent the ground (excited) states. Time axes are expressed in units of the excited state lifetimes $\tau_e = \Gamma^{-1}$. Plots on the right hand side show the Rabi oscillations at the beginning of the evolution, vanishing due to decoherence after a few lifetimes. The steady state population occupation is extracted as the values at time $400\,\tau_e$. Note the difference in occupation tendency of the $|g_R\rangle$ and $|g_C\rangle$ states for both species.

Photoionization of ^{133}Cs and ^{39}K

The discussion presented above was general in the sense that we included photoionization from both the ground and the excited states. However, for cesium and potassium 39, and the photoionizing wavelength used in this dissertation, this is not the case. The energy of photons in the 328 nm laser beam is equal to 3.78 eV and, based on the literature [145, 146], is sufficient to photoionize both atoms only from their excited states. This is presented in Tab. 6.2, where the excess energy ΔE shows the difference between the threshold energy for ionization from relevant atomic states and the photon energy in the ionizing beam. A negative value, as for the ground states of both species, means that the laser beam has less energy than required for ionization.

Species	**Initial state**	**Ionization energy**	**Excess energy for 328 nm**
Cs	$6^2S_{1/2}$	3.89 eV	−0.11 eV
Cs	$6^2P_{3/2}$	2.44 eV	1.34 eV
^{39}K	$6^2S_{1/2}$	4.34 eV	−0.56 eV
^{39}K	$6^2P_{3/2}$	2.72 eV	1.06 eV

Table 6.2: Ionization energies for ground and excited states of cesium and potassium 39. Excess energy is calculated for ionization wavelength 328 nm. Data based on [145] and [146].

Taken this into account, we repeated the simulation of our 4-level system, this time including the ionization process only for the excited state. It is modeled as an incoherent loss of the excited state population given by a term $-\gamma_{PI}\rho_{e_C}$. We arbitrarily set the ionization rate as one thousandth of the natural linewidth $\gamma_{PI} = 0.001\Gamma$, so that it is much slower than the basic dynamics of the system. The propagated results are presented in Fig. 6.2, where it can be seen that the total population, given by the trace of the density matrix, falls exponentially.

We fitted exponential decays to the total population curves and obtained almost perfect agreement with the exponential decay assumption. The curves deviate from the model only at the beginning of the propagation, where Rabi oscillations occur and the steady state occupation balance is not yet established. However, this timescale is negligible within the total interval of the simulation.

In addition, the results of the fits show that the decay is suppressed by the small population of the excited states. Although the ionization rate was comparable for both species, in reference to the characteristic time scale given by Γ, the process depletes the cesium population faster than for potassium, which is due to different

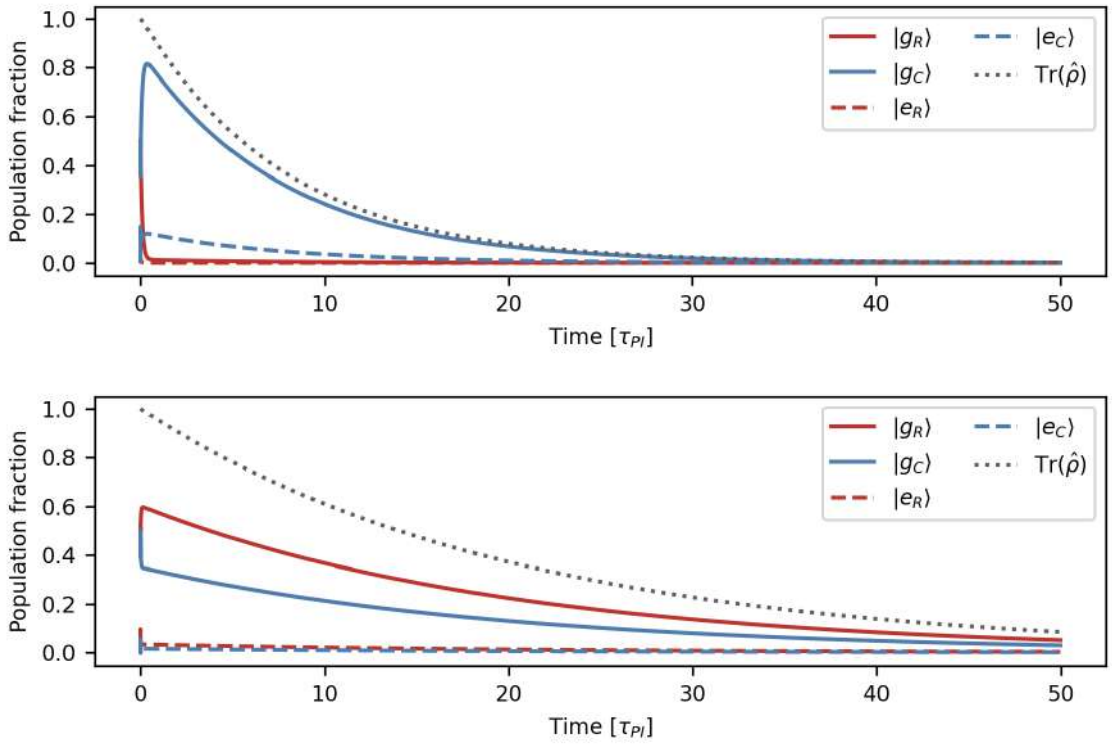

Figure 6.2: Simulation results for the population evolution in the magneto-optical trap for cesium (top plots) and potassium (bottom plot) with the ionizing beam present. Blue (red) lines correspond to the states coupled by cooler (repumper). Solid (dashed) lines represent the ground (excited) states. Gray dotted lines shows the trace of the density matrix equal to the total population, which exhibits an exponential decay. Time axes are expressed in units of the inverse ionization rate $\tau_{PI} = \gamma_{PI}^{-1} = 1000\Gamma^{-1}$.

pumping efficiencies. As already discussed, most of the atoms occupy the ground state, which is not affected by the ionizing beam. Yet, it is coupled with the excited state via the cooler light, and this coupling is stronger for cesium than for potassium, as implied by the steady state population occupation. From the exponential fits, we found that the damping rates were equal to $0.127\gamma_{PI}$ for cesium and $0.049\gamma_{PI}$ for potassium, which reflect occupation factors 13.26% and 4.94%, respectively.

6.2 Photoionization cross section

Optical setup

To generate the 328 nm beam, we utilize a second harmonic generation (SHG) cavity, which was custom made by Agile Optic[1]. The cavity is injected with 656 nm light that is generated by the frequency sum (SFG) of 1120 nm and 1584 nm. These wavelengths are provided by a laser system by Precilasers[2], which also encompasses the SFG in the laser head, generating up to 5 W of 656 nm light. Taking into account the SHG efficiency of our cavity, we have about 2 W of the available UV power.

The length of the cavity was stabilized using the Hänsch-Couillaud method [147], which monitors the change in polarization of the reflected pump light. We detect it with a simple setup consisting of a $\lambda/4$-waveplate, a polarizing beam splitter (PBS), and a balanced photodiode. The error signal is analyzed by RedPitaya[3] with an open source software Linien [148], which calculates the control signal for the cavity. It is amplified with a high-voltage amplifier[4] and applied to the piezo actuator of one of the cavity mirrors. The scheme of the optical setup for UV generation is presented in Fig. 6.3.

The output UV beam was Gaussian in the x and y directions, however elliptical in shape and diverging horizontally. To collimate both axes, we used two spherical lenses in a telescope configuration, which were tilted to behave as toric lenses. In this way, the vertical axis was magnified by a factor of 2, and the horizontal axis was collimated to a similar size by adjusting the tilt of the lenses and hence their effective focal length. Finally, we obtained a slightly elliptical beam with diameters $d_x = 1.76\,\text{mm}$ and $d_y = 2.84\,\text{mm}$ defined as double beam waist. The distortion of 1.6 could be eliminated with a telescope setup based on cylindrical lenses, which would allow independent shaping of the x and y axes.

The presented optical setup is a rather improvised arrangement because at that time we did not have at our disposal cylindrical lenses suitable for the UV light. In the future we plan to replace the lenses with a proper cylindrical telescope, unless, as they say, a temporary fix becomes permanent.

The last aspect to mention regarding the UV generation setup is the power control of the laser beam. At first, we used a standard approach of a $\lambda/2$-waveplate and a PBS to adjust the light power; however, the latter got burnt when we increased

[1] SHG VIS to UV cavity by Agile Optic
[2] FL-SF-656-5-CW by Precilasers
[3] STEMLab 125-14 by RedPitaya
[4] PDu150 by PiezoDrive

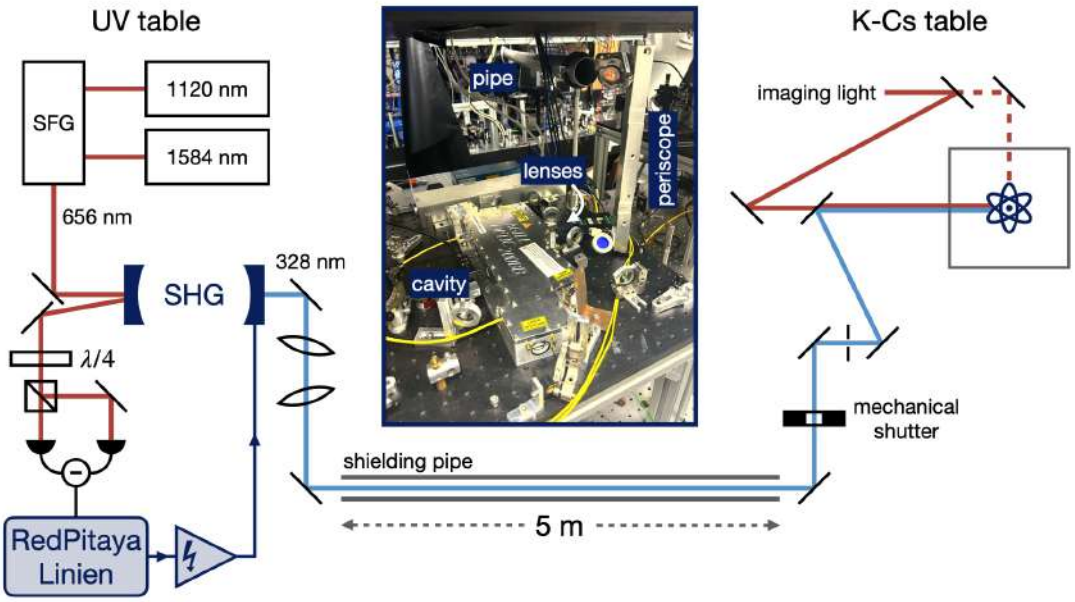

Figure 6.3: Optical setup for the photoionization cross section measurement. Left hand side: the setup for the generation of 328 nm light with Hänsch-Couillaud cavity stabilization. Inset photograph shows the SHG cavity, beam collimation, periscope and the entrance to the 5 m pipe, which is used to shield the UV beam, mainly for protection of people working in the laboratory. Right hand side: Light distribution on the optical table with the K-Cs chamber. The redirected imaging light path was used as a guide beam for the spatial adjustment. The red dashed line shows the usual path of the imaging beam.

the power to around 100 mW. We learned that we would need to buy high-power beamsplitters and decided to control the power of the 656 nm light injected into the SHG cavity by adjusting the pump current of the fiber laser. We use a side output port in the cavity, usually used to observe the transmission peak of the cavity on a photodiode, to track the UV power at the output. We verified that the photodiode output and the available UV power are linearly related and obtained a calibration curve for further reference.

The cavity setup was built and optimized by Dr. Jorge Mellado, one of the members of our laboratory. My sole contribution to the UV generation was to collimate the UV beam and add the RedPitaya expander, described in App. B, which enhanced the stability of the cavity length lock.

With the UV light prepared, we proceeded to send it to the experimental chamber in order to illuminate the atomic sample. The UV laser system and the MOT were placed on two optical tables in two different corners of the laboratory, around 5 m apart. We decided to send the UV light through free space, so we added a periscope to direct the laser beam parallel to the ground, at the level of the target MOT. We also installed PVC pipes that covered the beam, which was particularly important for safety reasons because the experimental chamber is situated near the eye level.

With the beam successfully delivered to the main experimental table, we observed that its shape, apart from the central gaussian part, has some low-power residuals in the form of horizontal stripes above and below the beam center. These probably come from reflections inside the cavity and were angularly separated as a result of long propagation. Therefore, we put a pinhole to spatially filter the beam and transmit only its Gaussian part. We also added a mechanical shutter to turn the UV light on and off, which we placed on a rubber damper to suppress vibrations.

Because of the long optical path we were concerned about the position of the UV beam and a potential need to stabilize it. For this reason, we measured the beam on a CCD camera for a time interval and extracted the center of the beam by fitting Gaussian profiles to the projections of the beam images onto the x and y axes. We performed two rounds of measurements, one short-term with exposure 10 ms and duration of 10 s, and one long-term with exposure 1 s and duration of 1 min. Based on the fits, we calculated the root mean square (RMS) displacement of the beam position, which is equal to $\delta^{(s)}_{RMS} = 18.9\,\mu$m for the short-term case and $\delta^{(l)}_{RMS} = 26.1\,\mu$m for the long-term case. Both are negligible in comparison to the beam size, so we decided that there is no need to implement any active beam position stabilization. The results are presented in Fig. 6.4.

Influence of the light-induced atomic desorption

As discussed in Sec. 3.2, the high-energy UV light can introduce desorption of atoms that are stuck to the surface of the glass cell and effectively increase the vapor pressure. Partially out of curiosity and to infer whether it is a strong effect, which would have to be included in the cross section measurements, we measured the loading curves of the cesium MOT illuminated by 328 nm light for different UV powers. To ensure that there is no photoionization, we moved the beam up so that it was passing through the experimental cell above the MOT cloud. Also, to enhance the LIAD we increased the beam size five times, so that the UV would illuminate a larger surface of the cell.

Similarly as in Sec. 3.2, we loaded the MOT for 5 s without UV light, and then

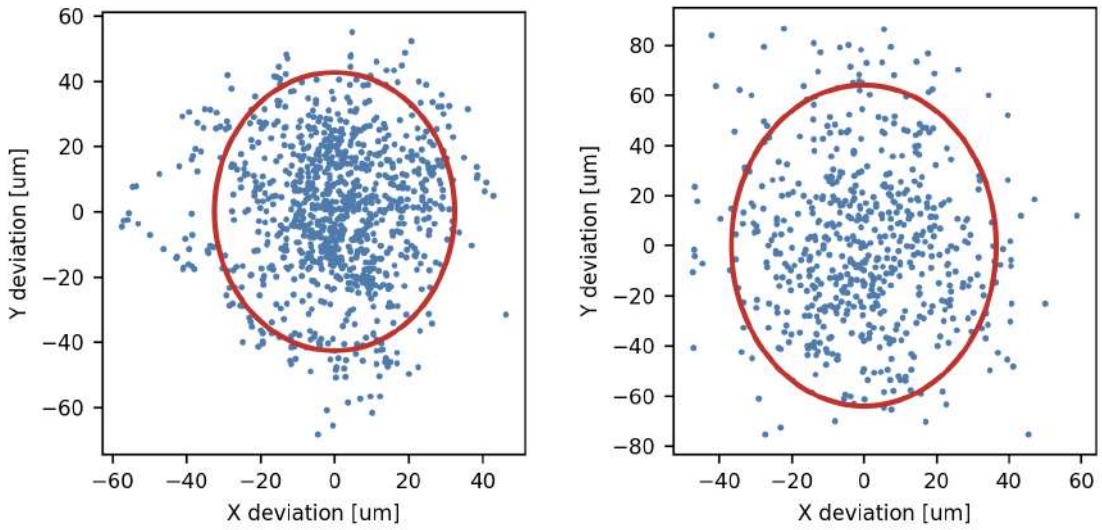

Figure 6.4: Beam pointing results for the short-term (left hand side) and long-term (right hand side) measurement. The axes show the deviation of the position from the average. Red ellipses represent the area of two standard deviations and encompass 84.2% and 86% of all points for the short and long-term cases, respectively.

opened the mechanical shutter to illuminate the cell surface with high-energy photons for another 5 s. We measured the loading curve with our fluorescence imaging system for different powers of UV. We fitted the MOT loading equation to the obtained curves with the Dormand-Prince propagation algorithm. The results are presented in Fig. 6.5 with a fit of the increase factor of the loading rate as a function of the UV power, coming from the adsorption-desorption theory (to remind the reader):

$$R(P_{UV}) \propto \frac{1 + \frac{k}{k_d} P_{UV}}{1 + \frac{k_a}{k_d} + \frac{k}{k_d} P_{UV}} \tag{6.8}$$

This time we got the coefficients $k_a/k_d = 7.3(50)$ and $k/k_d = 0.138(86)$. We observed a discrepancy in the k_a/k_d coefficient, with the value obtained in Sec. 3.2, which is supposed to be independent of UV wavelength or intensity, as in our model it is a property of the experimental setup, not the LIAD effect. In addition, the uncertainties of the fit are quite large, casting doubt on the applicability of the model.

The LEDs that we used for the LIAD in Sec. 3.2 were specifically chosen to avoid inducing photoionization, however, in the present experiment, UV light may

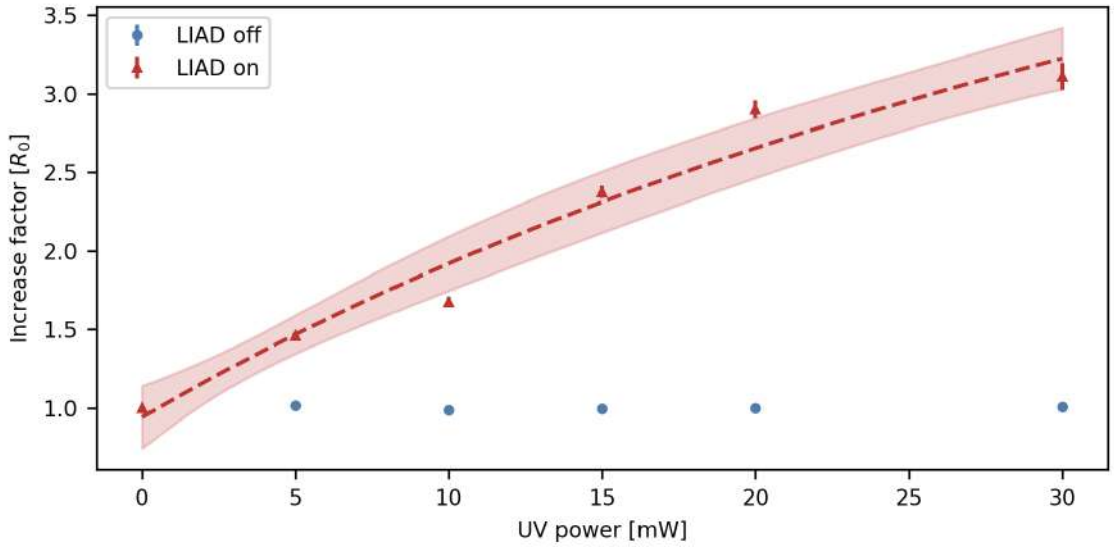

Figure 6.5: Relative increase factor of the loading rate for various 328 nm UV powers. The dashed red line is the fit of the adsorption-desorption model. Shaded area shows the uncertainty of the fit.

also ionize the background gas. This leads to higher vapor pressure but not of the "good kind", in a sense that we are not increasing the available number of atoms to be captured, but rather the background-induced losses. The ionization and recombination of the background gas have been studied in the literature [44], however, it has not yet been applied to LIAD. Nevertheless, we think that the adsorption-desorption model fails in this particular example.

Even with the improper model, the measurement showed an increase in the loading rate of the MOT, which means that we have to take into account the LIAD effect. With this knowledge, we proceeded to the next step, which was to measure the photoionization cross section.

The MOT loading rate

Firstly, we removed the previously inserted telescope to restore the beam size of $d_x = 1.76\,\text{mm}$ and $d_y = 2.84\,\text{mm}$ $2w_0$ diameters. This is slightly bigger than our MOT, so we encompass the atomic cloud with the UV light, especially in the most dense central region. In addition, the reduction in beam size decreases the influence of LIAD, as a smaller surface of the cell is irradiated with UV light.

The next step was to aim the UV beam at the atomic cloud, but at that moment we did not know how strong the effect of photoionization would be and whether it would be visible to the bare eye when observing the real-time view from our camera. We decided to use the imaging light as a pilot beam, a small portion of which we can turn on during the MOT operation. This light was overlapped with the UV on a dichroic mirror designed to reflect 328 nm and transmit 852 nm and 767 nm. We then adjusted the position of the imaging light such that it was destroying the MOT. The light was resonant with the cycling transition, so even small power was enough to significantly influence the balance of optical forces acting on the MOT. It is particularly convenient, as we can observe this effect in real-time on a camera. With the imaging beam position set, we simply adjusted the UV beam such that the two beams were concentric. We indeed observed the change of the size of the MOT with the UV beam on, so we proceeded to the actual measurements.

To suppress the LIAD effect even more, in each experimental sequence, we opened the UV shutter one second before the actual MOT loading. As we discussed in Sec. 3.2, the vapor pressure increase due to UV light is not permanent and vanishes after a while. We verified that this one-second period is sufficient by comparing two MOT loading curves, one with a one-second blast of the UV before the actual loading and one without, and did not observe any significant differences.

Then we measured the MOT loading curves for various UV powers and repeated the procedure ten times to acquire substantial statistics. We fitted the MOT rate equation using our propagation software and extracted the photoionization rate parameter γ_{PI}. These results are shown in Fig. 6.6. The UV induced losses indeed scale linearly with the light intensity, so we fitted a linear function to the extracted γ_{PI} data.

Finally, we calculated the cross section for photoionization which is equal to $1.14(15) \times 10^{-17}\,\mathrm{cm}^{-2}$ for cesium and $9.7(12) \times 10^{-18}\,\mathrm{cm}^{-2}$ for potassium. We compared these values with the theoretical predictions, which are presented in Fig. 6.7. The theoretical curve for cesium was plotted based on Tab. 2 in reference [149], whereas for potassium we digitized Fig. 4 in reference [150].

The values measured by us are higher than the theoretical predictions, yet for cesium our result lies within 2σ range. For potassium, the experimental value is almost two times larger than the theoretical one. We interpret this as resulting from the underestimation of the excited state occupation. As already stated several times, potassium is a problematic species due to its small hyperfine splitting. Our 4-level model does not take into account the excited state $F' = 1$, which can also exhibit the off-resonant driving of both the repumper and cooler beams and $F' = 0$ state, which can be influenced by the repumper. As shown in Fig. 6.1, for potassium the impact

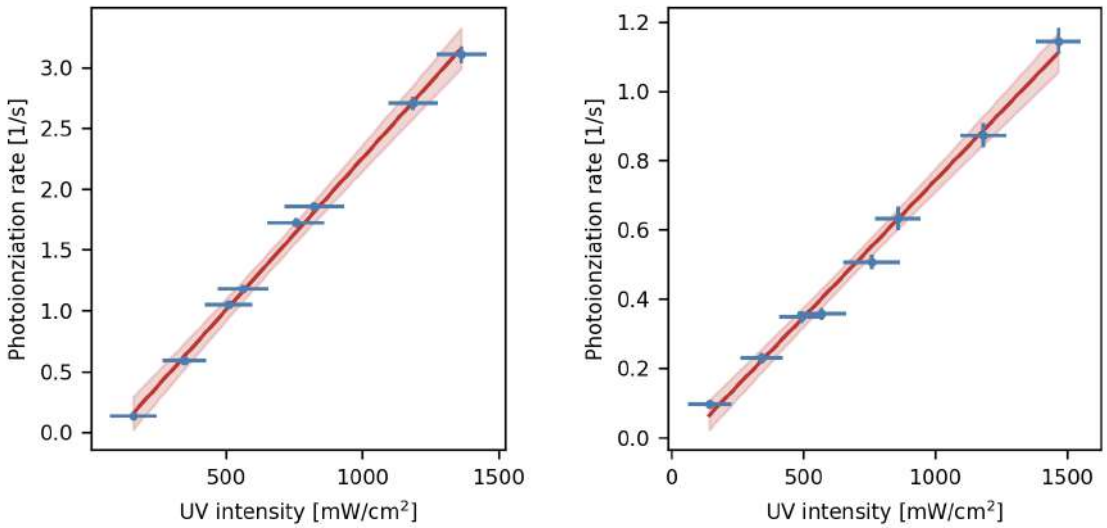

Figure 6.6: Photoionization rate γ_{PI} vs UV light intensity measured for cesium (left hand side) and potassium 39 (right hand side). Red solid lines are linear fits and the red shade represents the fit uncertainty.

of the repumper is crucial and it needs to be better accounted for in an extended model.

Ground state photoionization

This discussion has already shown that only the excited states can be photoionized by 328 nm for both cesium and potassium. Despite this fact, we decided to verify this experimentally. There have been reported methods of distinguishing between the photoionization of the ground and excited states in alkalis, either by alternating between the MOT and the UV light [136, 151] such that the probed sample is always in the ground state, or by observing the cloud fluorescence after switching off the atomic source with and without the MOT beams [152]. These two methods rely on optical pumping induced by the MOT beams and allow for distinction between the ground and the excited states.

We propose another approach, namely, photoionization in a dipole trap, which, as a conservative one, preserves the hyperfine state of the atomic population. The UV light, when turned on, should in principle introduce a loss mechanism and reduce the lifetime of the trap. We performed a series of measurements in the dipole traps of cesium and potassium 39, for both hyperfine ground states.

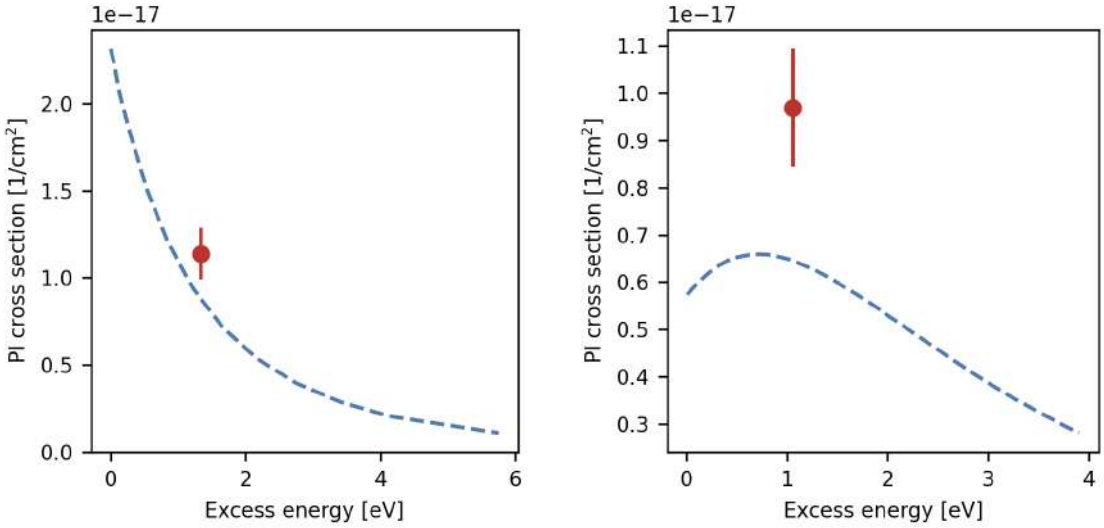

Figure 6.7: Photoassociation cross section for 328 nm (red dots) and theoretical predictions for cesium [149] (left hand side) and potassium 39 [150] (right hand side). The details of the discrepancy for potassium are described in the main text.

In none of the measured cases, presented in Fig. 6.8, did we observe a significant difference between the lifetimes, regardless of whether the trap was illuminated by the UV light or not. This proves that indeed the 328 nm photons carry too little energy to photoionize the atoms from their ground states, as expected. There is another conclusion that could be drawn from these measurements: we have shown that indirect ionization, for example via off-resonance excitation of a Rydberg state, does not occur for cesium and potassium atoms in the ground state. This is an important conclusion for devising experimental sequences involving silver and one of the studied alkalis because it points at a possible pathway to limiting the consequences of the alkali MOT depletion by the silver cooling light - one can transfer the alkali species into the optical dipole trap first and only then start loading the silver magneto-optical trap.

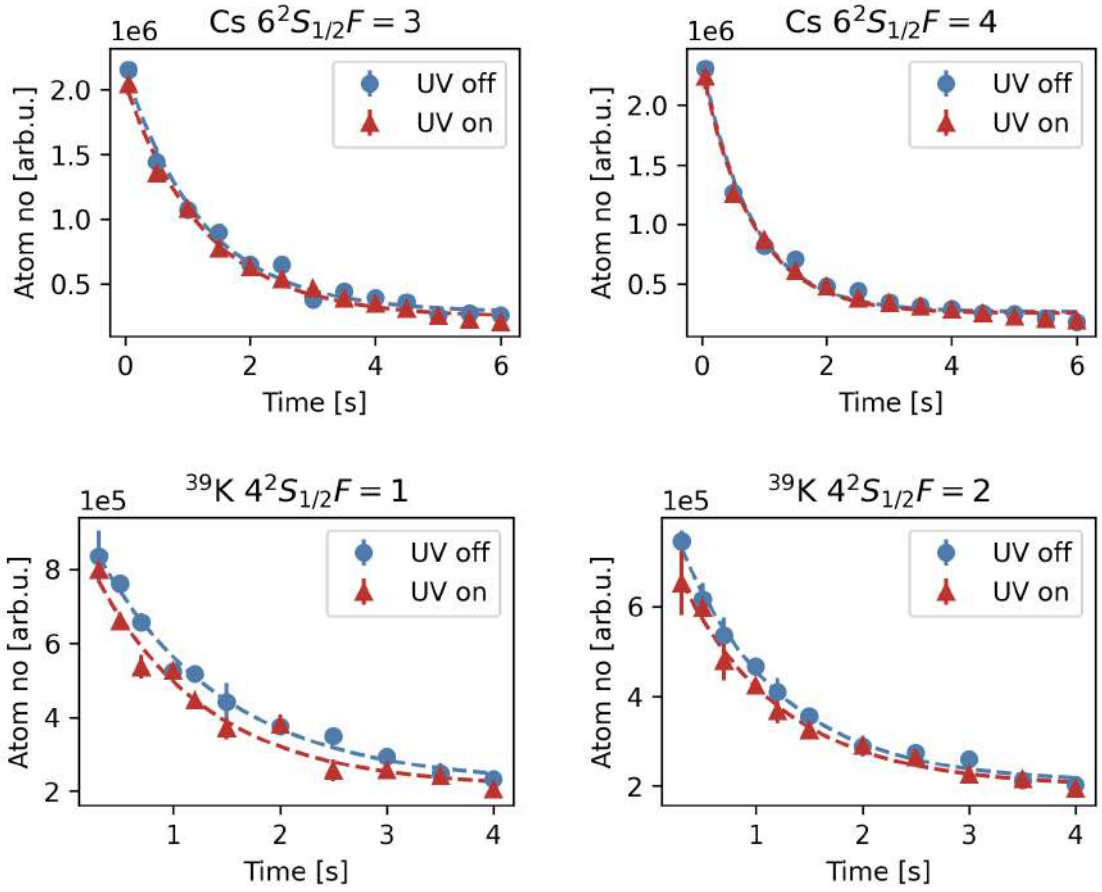

Figure 6.8: Measurements of the lifetimes of dipole traps with and without the photoionizing beam present. The traps were loaded with different ground states of cesium and potassium-39, which are denoted as the title of the plot. The dashed curves are fits of an exponential decay. The UV intensity in each of the measurements was around $1000\,\mathrm{mW/cm^2}$.

Chapter 7

Conclusions and outlook

In this final chapter, I would like to conclude the dissertation by reviving crucial results of each of the topics discussed. I will also discuss the possible extensions of the projects that I was involved in, which hopefully will be continued by other researchers in our laboratory.

Firstly, regarding the magnetic field control in the apparatus, we presented two circuits that allowed for precise control and timing in the experimental sequences.

The sub-millisecond switch-off provides a fast current decay in our main coils, responsible for generating the quadrupole and uniform magnetic fields. Thanks to its simplicity and independence from the initial current value, this reliable add-on ensures that no unwanted residual field is present in the experimental chamber.

This was particularly important for two stages, gray molasses cooling and Feshbach resonance measurement. The GMC is highly sensitive to the magnetic field, which was also investigated in the dissertation. Since this stage directly follows after the MOT, the residual field would disturb the cooling process. To some extent, thanks to the fast switch we were able to reach the state-of-the-art temperatures of the atomic samples. With regard to Feshbach resonances spectroscopy, it requires high field values, reaching hundreds of Gauss, which directly translates to high currents flowing through the coils. Without our extension, the residual field would last during the imaging sequence, which could disturb the obtained data. The same mechanism applies to magnetic trap which we use for the Stern-Gerlach measurement of spin states occupation.

Following the topic of magnetic field control, we designed and built a bi-directional current source that allows us to precisely adjust the current flowing through the compensation coils. We presented an extensive study on the influence of the magnetic field on the temperatures reached in GMC cooling, and used it to compensate the

stray field present in the experimental chamber. Our current sources are also an invaluable solution for controlling the quantization axis, which is extremely important for preserving the spin states of the atomic sample. Our setup does not only generate the quantization axis, but also allows for its adiabatic rotation in space, which we employ in Feshbach spectroscopy [83], and Feshbach-enhanced photoassociation spectroscopy [79].

We also started the design and prototyping of the controller for the main coils, based on other projects described in the literature. This topic was not covered in the present thesis, as after the first prototypes failed, we decided to focus on other aspects, more important for the main research direction. However, the work that has already been completed on this topic gave us important insight into the problem, which can now be continued by future members of the research group.

We presented a setup for offset lock of our cesium external cavity diode lasers, which incorporates a frequency divider in the optical phase-locked loop. Although this project did not fully meet expectations and did not provide phase coherence, it allows us to simplify the optical setup for preparing light for experiments with cesium. With the lesson learned, we also proposed essential amendments that could improve the setup. This project was developed alongside other investigations regarding the phase-coherent light source for cesium, based on injecting laser diodes with the 9 GHz sidebands generated by electro-optic modulator [153]. This indicates, that in cesium systems the laser coherence is an essential issue.

Further, we presented the investigation of the light-induced atomic desorption in our apparatus and discussed its application in single-chamber systems. This allowed us to improve the loading rate of the MOT by a factor of 3.5 and hence the trappable number of atoms, while maintaining the vacuum conditions for further experimental stages. It also provided us with information about the behavior of the background gas in our apparatus, considering its tendency to stick to the surface of the glass cell. Out of curiosity, we made an attempt to derive a model of the pressure restoration after turning LIAD off, with an original method of propagation of MOT rate equation including the transient response of trap fluorescence to switching LIAD on and off. This was merely a qualitative result that was not extensively investigated and did not suit this dissertation. However, some foundations are laid for future research, as vacuum quality is always of high importance in the ultracold experiments.

The longest chapter of this dissertation was devoted to an extensive study on a laser system, that was designed with the aim of delivering light suitable for the needs of the precise spectroscopy of ultracold molecules. W presented a fully automated system referenced to a frequency comb that meets the standards of modern equipment. The device was supplied with a decentralized server-based architecture

providing autonomous operation regarding frequency tuning, detecting deviations from the setpoint and applying proper corrections. The design of the system is general in a sense, that it is easily scalable and can be transferred to any other laser that assists automatic tuning. The choice of servers as the main software layer enables platform-independent integration with any experimental control architecture.

We reached sub-millihertz Allan deviation averaged over 1 s of the comb repetition frequency, which enabled high stability of the referenced laser and precise determination of its frequency. We also extended the design of comb spectrum selection proposed by Hänsch et al. [111] by automatizing the diffraction grating rotation and including it within the architecture of the system. This in turn allowed for broad tunability of the laser across the spectrum of the frequency comb.

The laser system was planned to be used in ultracold Cs_2 precision spectroscopy, as an extension of studies already started in our laboratory [79], yet due to malfunction of our pump laser the research had to be interrupted at the final stage. Although we obtained some preliminary data and validated the laser system on the cesium D_2 line spectroscopy, its quality is not sufficient for the requirements of a doctoral dissertation. However, even without the pinnacle results, our approach towards an automated and autonomous operation is a novelty in the field.

In addition to a high-accuracy topic, we also presented a clean-up system for retrieval of the optical carrier signal referenced to an optical atomic clock after long-distance transmission. In particular, we depicted the design and validation of a digital servo that is responsible for correction of the frequency of a remote laser locked to an ultra-low expansion cavity, based on comparison with transferred optical carrier. It opens a possibility to transfer the time standard across large distances, which is crucial not only for metrology but also for fundamental research regarding comparison between optical atomic clocks.

In the last chapter, we presented studies on the photoionization of excited states of cesium and potassium-39 caused by UV light with wavelength 328 nm. This research was conducted within a new direction our laboratory is heading, namely toward formation of highly polar CsAg and KAg molecules. This area is not yet explored as the theoretical proposals are still recent [19] and experimental groups are only beginning to construct Ag apparatuses [137].

The photoionization measurements are valuable, because they show that this process is non-negligible and can easily suppress the obtainable number of atoms in the alkali MOT, when illuminated with UV. This means, that a certain strategy for the experimental sequence has to be considered, especially because silver in addition to an exotic UV wavelength also requires quite high laser intensities.

The results obtained show small discrepancy between the measured photoioniza-

tion cross section and the theoretically predicted value for potassium-39, which we interpret as coming from underestimating the occupation factor of the excited state in the MOT. An extension of the model including all of the excited states would be required for better estimation, or direct measurement as proposed in literature [136].

As depicted in the introduction, this thesis is a summary of a six-year work. The direction of the research at the beginning was aimed at the spectroscopy of ultracold molecules, yet over time new opportunities arose from the projects that our laboratory and I were involved in. This caused a slight deviation from the initially obtained course, yet still within the field of precise time-frequency measurements. The technical problems that occurred along the way also contributed, the major one being the malfunction of the laser pump in our Ti:Sapphire system.

In addition to the topics described herein, there were also many others that I did not discuss, as they were minor improvements to the apparatus that would extend this already comprehensive thesis. To name a few, I was also responsible for minor electronic circuits like power switches enhancing the operation of AOMs, or developing the software layer that allowed for automatization of oscilloscopes, arbitrary function generators, signal generators, and spectrum analyzers or the monitoring of environmental conditions in the laboratory.

Ultracold apparatuses are rarely constructed by a single human being, and we were employing our best abilities to develop a system which we built from the first mirror placed the optical table. In writing this dissertation, I close a certain chapter in hope that this work will be a valuable opening for future researchers in our laboratory.

Appendix A

Runge-Kutta algorithm

To propagate the rate equations, we utilized a method called the Runge-Kutta algorithm (RK) [154, 155], which is a higher-order version of the Eulerian method. It calculates the prediction of the evolution of the function using only the first derivative, which makes it a useful tool for solving first-order ordinary differential equations, such as MOT loading, trap loss, or Bloch equations.

Given a function value at the point t_0, we can approximate its value at the point $t_0+\Delta t$ by estimating the function change based on its derivative. The simple Eulerian method follows a formula $y(t_0 + \Delta t) = y(t_0) + y'(t_0)\Delta t$ that uses the information about the tangent to the function at the point t_0. RK algorithm is a variation of this method, which takes into account the derivative values at different midpoints in the section $[t_0, t_0 + \Delta t]$ to approximate not only the tangent but also the curvature of the function. The order of the algorithm used is denoted at the end of the acronym.

We will briefly describe the RK4 algorithm, which is a decent compromise between the computational cost and the approximation error ($\mathcal{O}(\Delta t^5)$). The graphical schemes that present the algorithm are shown in Fig. A.1. Let us assume that we have an equation of the form $y'(t) = f(t, y)$ with an initial condition $y(t_0) = y_0$. Although it is fulfilled only by the points given by a solution $y(t)$, we can treat the right-hand side of the equation as a separate function defined in the (t, y) plane. The function $f(t, y)$ should be continuous, so that when evaluated in the points in proximity to the solution it returns valid approximations of the tangent. In principle, y can be a vector, which can be easily implemented and extend the algorithm to propagate a set of differential equations.

The algorithm calculates k_i contributions in an iterative manner, following the

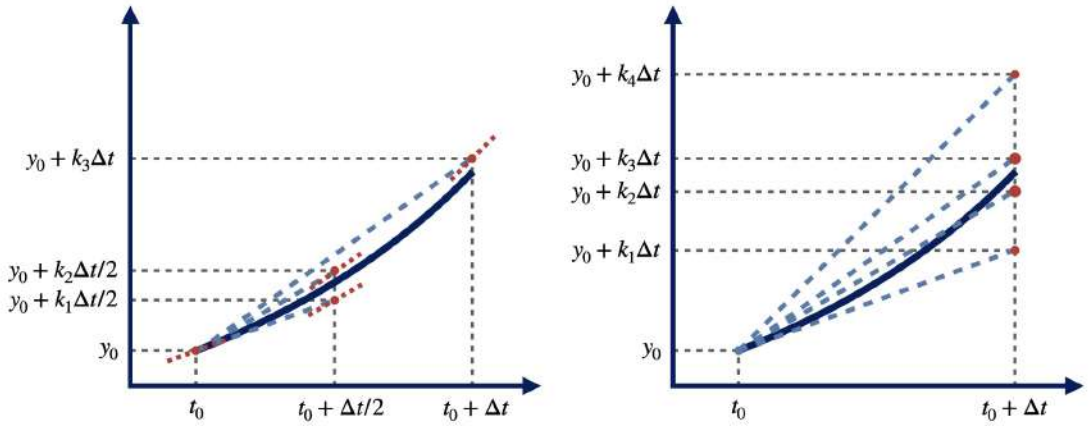

Figure A.1: Graphical scheme of the Runge-Kutta algorithm of the 4^{th} order. Dark blue curve is the actual solution. Left hand side: Procedure of calculating the k_i contributions. Red dots correspond to points on the (t, y) plane where $f(t, y)$ is evaluated. Dashed red lines present the evaluated tangent. Right hand side: Procedure of approximating the solution value based on k_i combination. Red dots correspond to contributions to the final approximation with dot size showing the weight.

formulae:

$$\begin{cases} k_1 = f(t_0, y_0) \\ k_2 = f(t_0 + \frac{\Delta t}{2}, y_0 + k_1 \frac{\Delta t}{2}) \\ k_3 = f(t_0 + \frac{\Delta t}{2}, y_0 + k_2 \frac{\Delta t}{2}) \\ k_4 = f(t_0 + \Delta t, y_0 + k_3 \Delta t) \end{cases} \tag{A.1}$$

which carry information about the tangent approximations in different midpoints. Then they are combined with different weights to estimate the solution:

$$y(t_0 + \Delta t) = y(t_0) + \frac{\Delta t}{6}(k_1 + 2k_2 + 2k_3 + k_4) \tag{A.2}$$

The coefficients used in a certain method variation can be represented as a Butcher table, an exemplary one for RK4 is shown in Tab. A.1. It contains the time midpoints and combinations of k_i used to calculate both the other k_i and the final solution approximation.

This algorithm has the drawback of a constant timestep Δt, which must be chosen sufficiently small to encompass the highest frequencies present in the solution variability, increasing the required number of iterations and $f(t, y)$ evaluations. For some equations, regions where the solution changes rapidly and slowly are separated,

k_i	Δt	Δy			$y^{(4)}$
k_1	0				$\frac{1}{6}$
k_2	$\frac{1}{2}$	$\frac{1}{2}$			$\frac{1}{3}$
k_3	$\frac{1}{2}$	0	$\frac{1}{2}$		$\frac{1}{3}$
k_4	1	0	0	1	$\frac{1}{6}$
		k_1	k_2	k_3	

Table A.1: Butcher table of the Runge-Kutta 4$^{\text{th}}$ order method (RK4). The Δt column contains coefficients corresponding to the temporal midpoints. The Δy column contains coefficients used to calculate the k_i contributions. Last column contains weight coefficients of k_i combination to approximate the solution.

so the computational cost is risen unnecessarily in the slowly changing part. For this reason, a modification of the RK4 algorithm with a variable timestep size is introduced [156], called the Dormand-Prince algorithm or RK45.

In RK45 version, two approximations are calculated, of orders 4 and 5, with the latter treated as a more robust. The comparison between the two outcomes delivers an estimate of the local error of the algorithm and is used to determine the change in the timestep. If the error is larger than a threshold, the timestep is reduced, so that the algorithm converges within the set tolerance. If the error is, on the other hand, smaller than the threshold, the timestep is increased to lower the computational cost and accelerate the calculations.

In general, two tolerances can be introduced, relative and absolute, which correspond to the relative and absolute local errors. The tolerances settings are case-dependent, with absolute or relative accurate when the solution has low or large values, respectively. The local approximation error can be calculated from the formula:

$$\text{err} = \left\| \frac{y^{(5)} - y^{(4)}}{\text{tolAbs} + |y^{(5)}|\text{tolRel}} \right\| \tag{A.3}$$

If an error value is greater than unity, the propagation step is considered invalid and is repeated with a new timestep. Otherwise, the timestep is increased, and the propagation runs further. In both cases, the timestep is calculated as follows:

$$\Delta t_{new} = \eta \Delta t_{old} \left(\frac{1}{\sqrt[5]{\text{err}}} \right) \tag{A.4}$$

k_i	Δt	Δy						$y^{(5)}$	$y^{(4)}$
k_1	0							$\frac{35}{384}$	$\frac{5179}{57600}$
k_2	$\frac{1}{5}$	$\frac{1}{5}$						0	0
k_3	$\frac{3}{10}$	$\frac{3}{40}$	$\frac{9}{40}$					$\frac{500}{1113}$	$\frac{7571}{16695}$
k_4	$\frac{4}{5}$	$\frac{44}{45}$	$-\frac{56}{15}$	$\frac{32}{9}$				$\frac{125}{192}$	$\frac{393}{640}$
k_5	$\frac{8}{9}$	$\frac{19372}{6561}$	$-\frac{25360}{2187}$	$\frac{64448}{6561}$	$-\frac{212}{729}$			$-\frac{2187}{6784}$	$-\frac{92097}{339200}$
k_6	1	$\frac{9017}{3168}$	$-\frac{355}{33}$	$\frac{46732}{5247}$	$\frac{49}{176}$	$-\frac{5103}{18656}$		$\frac{11}{84}$	$\frac{187}{2100}$
k_7	1	$\frac{35}{384}$	0	$\frac{500}{1113}$	$\frac{125}{192}$	$-\frac{2187}{6784}$	$\frac{11}{84}$	0	$\frac{1}{40}$
		k_1	k_2	k_3	k_4	k_5	k_6		

Table A.2: Butcher table of the Dormand-Prince method (RK45). The Δt column contains coefficients corresponding to the temporal midpoints. The Δy column contains coefficients used to calculate the k_i contributions. Last columns contains weight coefficients of k_i combination to approximate the solution of 5^{th} ($y^{(5)}$) and 4^{th} ($y^{(4)}$) order.

where η is a safety coefficient that protects against too large timestep changes, usually around 0.9.

The Dormand-Prince method uses a carefully designed set of midpoints and weights, to reduce the computational cost even more, by reducing the number of $f(t, y)$ evaluations. For this algorithm, we will confine ourselves to presenting the Butcher table, shown in Tab. A.2, as enumerating all algorithm formulae would be illegible.

Appendix B

RedPitaya expander

In most of the lock loops presented in this thesis, we used some version of the RedPitaya, working as either a PLL or a PID controller. It is generally a handy and universal device, with many open-source firmware varieties, capable of the state-of-the-art operation in modern laboratories. Its drawback is that it has a limited output range, and for this reason, we designed an expander to enhance the performance and used it in various lock loops presented in this thesis.

The output voltage range of the RedPitaya is $\pm 1\,\mathrm{V}$, which is usually enough to acquire a lock. However, the controlled device often has a wider input range, which means that there is limited utilization of the input capabilities of the subsequent device. From the experience with stabilizing various devices, the broader range is often exploited by the integral or offset components of the control signal. We usually engage the stabilization loop in the middle of the control ranges so that we take advantage of the full dynamic range of the controller. As time passes and the devices exhibit slow drift, the control loop compensates for it by adding a constant offset. Its accumulation may result in getting closer to the boundary of the RedPitaya output, limiting its dynamic range, and potentially making the lock loop unstable.

To compensate for this effect, we designed a printed circuit board (PCB), which we insert between the RedPitaya and the subsequent device. The idea of operation of the PCB is to integrate the slow offset drift of the RedPitaya's output signal, while maintaining the mid- and high-frequency components.

Circuit description

The input signal is divided into two paths. The first goes through a unity gain amplifier with 1 MHz bandwidth to preserve the control signal without changes. The

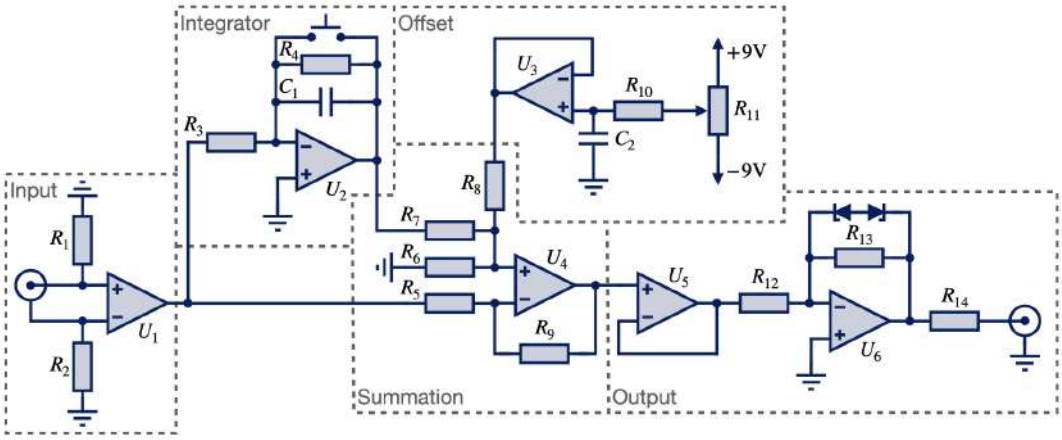

Figure B.1: Electronic scheme of the RedPitaya expander circuit. Values of the components are listed in the Tab. B.1. The circuit is described in detail in text.

second has an integrating amplifier with low bandwidth, around 1 Hz. Then the two signals are added by a summing amplifier. The last part is another operational amplifier with unity gain and clamping Zener diodes to bound the output voltage to the desired levels. We have also added a push button in the integral feedback loop, to reset the integral value manually if needed, by short-circuiting the feedback capacitor. The scheme of the circuit is shown in Fig. B.1 and the components values are described in Tab. B.1.

Whenever a drift occurs in the controlled device, the RedPitaya output adds a little offset, which is integrated by our PCB, returning the RedPitaya back to 0. As a result, the part of the control loop responsible for keeping the constant offset and drift cancellation is the integrator on our PCB. This ensures that RedPitaya is always working around 0 V with the highest dynamic range.

It looks like we are introducing an extra integrator into the loop, which could cause instability of the lock. It is not exactly the case because here we integrate the control signal, rather than the error. In addition, we choose the integrator bandwidth below 1 Hz, so that the phase lag induced by it does not decrease the phase margin [102] of the loop, since the controller's integrators usually have much higher bandwidth.

Also worth mentioning is the choice of electronic components. For the input section, we chose the INA128[1] instrumentation amplifier for its low noise levels and to isolate the input and PCB grounds with high impedance. For the operational ampli-

[1]INA128 instrumentation amplifier by Texas Instruments

Component	Model/value	Symbol
Instrumentation amplifier	INA128	U_1
Operational amplifier	TL074	U_2, U_4, U_5, U_6
	OP07	U_3
Resistor	100 kΩ	R_1, R_2
	R_{i1}	R_3
	R_{i2}	R_4
	1 kΩ	R_5, R_6, R_7, R_8, R_9, R_{10}, R_{12}, R_{13}
	50 Ω	R_{14}
Potentiometer	20 kΩ	R_{11}
Capacitor	C_i	C_1
	100 nF	C_2

Table B.1: Values of the electronic components used in the RedPitaya expander PCB. Symbols are corresponding to the ones in Fig. B.1
. Values R_{i1}, R_{i2} and C_i are not given explicitly because they are used to shape the transmittance of the circuit and are chosen for a specific application.

fiers which have to pass the control signal unchanged, we chose TL074[2] due to their 3 MHz bandwidth at unity gain, as we usually assume that the reasonable bandwidth of the lock loop should be around 1 MHz. The integrator is also implemented with TL074, which is not a requirement in terms of bandwidth, but we were left with one amplifier in a quad package, so we decided to use all available resources. There is also an additional section to control the DC offset of the expander and compensate for the parasitic offset voltage, where we used OP07[3] which has a lower bandwidth of 0.6 MHz at unity gain, yet sufficient to keep constant voltage, and we had spare ones in the laboratory.

Circuit transfer function

The transfer function of the designed circuit is the product of the transfer functions of the integrator and a unity gain. We used an inverting leaky integrator circuit[157], which means that the gain at low frequencies is limited by a resistor in parallel with the capacitor in the amplifier's feedback loop. Due to residual drift of the operational amplifier, even with grounded input, the integrator wanders off. An

[2]TL074 operational amplifier by Texas Instruments
[3]OP07 operational amplifier by Texas Instruments

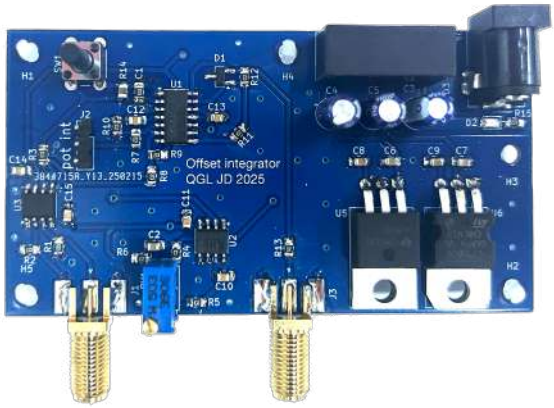

Figure B.2: A photograph of the assembled RedPitaya expander.

additional resistor provides DC feedback for stable biasing, so that in an idle state, the output does not swing to the supply voltage.

The open-loop transmittance of the circuit can be shaped by choosing proper values of the integrator feedback loop components and, keeping the notation from Tab. B.1, is given by:

$$H(s) = -\frac{R_{i2}}{R_{i1}} \frac{1}{1 + sR_{i2}C_i} \tag{B.1}$$

where $s = \sigma + i\omega$ is a parameter on the s-plane, where the real and imaginary parts describe the attenuation and the frequency response of the system, respectively. The transfer function is usually presented in the form of a Bode plot [102], where the gain and phase shift of the system are plotted. To derive them, we need to confine s to the imaginary axis by assuming $s = 2\pi if$, so that we only analyze the frequency response. Then the gain of the system is given by $k(f) = |H(2\pi if)|$ and the phase shift by $\varphi(f) = \arg(H(2\pi if))$.

From this formula, we can extract the two parameters that shape the transfer function, namely the DC gain $g_{DC} = -R_{i2}/R_{i1}$ and the integrator pole frequency $f_i = 1/(2\pi R_{i1}C_i)$. The latter is the frequency at which the gain is 3 dB lower than the DC gain.

A quite useful parameter in terms of shaping the transfer function is the gain crossover, which is a frequency at which the gain of the transfer function is equal to one. In our case this is the point where the integral starts to operate, as seen from the high frequency perspective. It is crucial in the design, as we would like it to be much lower than the analogous parameter in the controller loop to avoid decreasing

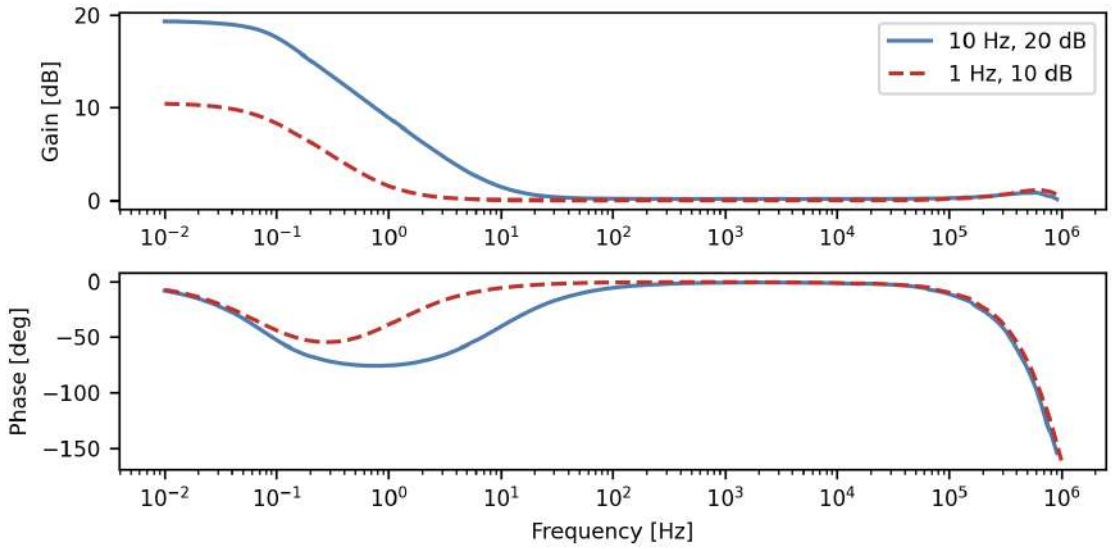

Figure B.3: Bode plots of open-loop transmittance for two PCBs with different DC gains and gain crossovers.

the phase margin. The gain crossover is given by formula:

$$f_{0\mathrm{dB}} = \frac{1}{2\pi R_2 C}\sqrt{\left(\frac{R_2}{R_1}\right)^2 - 1} \tag{B.2}$$

We measured the open-loop transfer function of the assembled circuit to verify that it works according to the design. For this we drove it in an open loop with a sine function and measured the output on the oscilloscope. We measured at least three periods of the signal for each frequency and fitted a sine function with phase offset. From the fit results, we obtained the amplitude and the phase parameters. Simultaneously we measured the input signal on a second channel as a reference, to calculate the gain and the phase shift, which we plotted on a Bode plot. The results for two boards with different g_0 and $f_{0\mathrm{dB}}$ are shown in Fig. B.3.

An additional lowpass filter behavior is visible at the end of the measurement range, which comes from the finite bandwidth of the operational amplifiers. The formula in Eq. B.1 is derived in an ideal circuit, yet in reality, the components have a roll-off frequency of around 1 MHz.

The open-loop transfer function measurements showed the agreement between the design assumptions and the realization. The PCB was then successfully implemented in various lock loops in laboratory laser systems.

Appendix C

Optical Bloch equations for 4-level system

For visual clarity, we label the hyperfine states as follows:

- $|g_R\rangle$: $6^2S_{1/2}F = 3$ for cesium and $4^2S_{1/2}F = 1$ for potassium 39
- $|g_C\rangle$: $6^2S_{1/2}F = 4$ for cesium and $4^2S_{1/2}F = 2$ for potassium 39
- $|e_R\rangle$: $6^2P_{3/2}F' = 4$ for cesium and $4^2P_{3/2}F' = 2$ for potassium 39
- $|e_C\rangle$: $6^2P_{3/2}F' = 5$ for cesium and $4^2P_{3/2}F' = 3$ for potassium 39

The relative line strength factors for a $F \to F'$ transition, averaged over m_F states, are given as [84]:

$$S_{FF'} := (2F'+1)(2J+1) \begin{Bmatrix} J & J' & 1 \\ F' & F & I \end{Bmatrix}^2 \tag{C.1}$$

and are used to calculate the branching ratios for spontaneous emission, which describe the probability of a decay channel $F' \to F$:

$$\beta_{F'F} := \frac{(2F+1)S_{FF'}}{\sum_q (2F_q+1)S_{F_qF'}} \tag{C.2}$$

In the Bloch equations, the light intensity is represented by the Rabi frequency Ω. The laser beam intensity is usually expressed in reference to the saturation intensity of the cycling transition, which allows a reliable comparison between species.

For optical fields coupling other transitions, the corresponding Rabi frequency is calculated as:

$$\Omega_{FF'} = \Gamma\sqrt{\frac{I}{2I_{sat}}\frac{S_{FF'}}{S_{g_C e_C}}} \tag{C.3}$$

In addition, in the optical Bloch equations presented herein, we changed the typical terms $\rho_{ge} - \rho_{eg}$ with an imaginary part $\mathfrak{Im}(\rho_{ge})$, which is valid because the density matrix is hermitian and exhibits symmetry $\rho_{ge} = \rho^*_{eg}$. This simplifies the numerical calculations by reducing the number of evaluations of the equation functions.

Populations

$$\dot{\rho}_{g_R} = (\Gamma\beta_{RR} - \gamma^{(g)}_{PI})\rho_{e_R} + \Omega_R\mathfrak{Im}(\rho_{g_R e_R})$$

$$\dot{\rho}_{g_C} = (\Gamma\beta_{RC} - \gamma^{(g)}_{PI})\rho_{e_R} + \Gamma\rho_{e_C} + \Omega_C\mathfrak{Im}(\rho_{g_C e_C}) + \Omega_{off}\mathfrak{Im}(\rho_{g_C e_R})$$

$$\dot{\rho}_{e_R} = -(\Gamma + \gamma^{(e)}_{PI}))\rho_{e_R} - \Omega_R\mathfrak{Im}(\rho_{g_R e_R}) - \Omega_{off}\mathfrak{Im}(\rho_{g_C e_R})$$

$$\dot{\rho}_{e_C} = -(\Gamma + \gamma^{(e)}_{PI})\rho_{e_C} - \Omega_C\mathfrak{Im}(\rho_{g_C e_C})$$

Coherences

$$\dot{\rho}_{g_R e_R} = (i\Delta_R - \Gamma/2)\rho_{g_R e_R} + i\frac{\Omega_R}{2}(\rho_{e_R} - \rho_{g_R})$$

$$\dot{\rho}_{g_C e_C} = (i\Delta_C - \Gamma/2)\rho_{g_C e_C} + i\frac{\Omega_C}{2}(\rho_{e_C} - \rho_{g_C})$$

$$\dot{\rho}_{g_C e_R} = (i\Delta_{off} - \Gamma/2)\rho_{g_C e_R} + i\frac{\Omega_{off}}{2}(\rho_{e_R} - \rho_{g_C})$$

Bibliography

[1] Dalibard, J. and Cohen-Tannoudji, C. "Laser cooling below the Doppler limit by polarization gradients: simple theoretical models". *JOSA B* **6**(11), (1989). DOI: 10.1364/JOSAB.6.002023.

[2] Lett, P. D. et al. "Observation of Atoms Laser Cooled below the Doppler Limit". *Physical Review Letters* **61**(2), (1988). DOI: 10.1103/PhysRevLett.61.169.

[3] Phillips, W. D. "Nobel Lecture: Laser cooling and trapping of neutral atoms". *Reviews of Modern Physics* **70**(3), (1998). DOI: 10.1103/RevModPhys.70.721.

[4] Ludlow, A. D. et al. "Sr Lattice Clock at 1×10^{-16} Fractional Uncertainty by Remote Optical Evaluation with a Ca Clock". *Science* **319**(5871), (2008). DOI: 10.1126/science.1153341.

[5] Cundiff, S. T. and Ye, J. "Colloquium: Femtosecond optical frequency combs". *Reviews of Modern Physics* **75**(1), (2003). DOI: 10.1103/RevModPhys.75.325.

[6] Hänsch, T. W. "Nobel Lecture: Passion for precision". *Reviews of Modern Physics* **78**(4), (2006). DOI: 10.1103/RevModPhys.78.1297.

[7] Hall, J. L. "Nobel Lecture: Defining and measuring optical frequencies". *Reviews of Modern Physics* **78**(4), (2006). DOI: 10.1103/RevModPhys.78.1279.

[8] Oelker, E. et al. "Demonstration of $4.8 \times 10^{--17}$ stability at 1 s for two independent optical clocks". *Nature Photonics* **13**(10), (2019). DOI: 10.1038/s41566-019-0493-4.

[9] Brewer, S. M. et al. "$^{27}Al^{+}$ Quantum-Logic Clock with a Systematic Uncertainty below 10^{-18}". *Physical Review Letters* **123**(3), (2019). DOI: 10.1103/PhysRevLett.123.033201.

[10] Williams, P. A., Swann, W. C., and Newbury, N. R. "High-stability transfer of an optical frequency over long fiber-optic links". *JOSA B* **25**(8), (2008). DOI: 10.1364/JOSAB.25.001284.

[11] Predehl, K. et al. "A 920-Kilometer Optical Fiber Link for Frequency Metrology at the 19th Decimal Place". *Science* **336**(6080), (2012). DOI: 10.1126/science.1218442.

[12] Ma, L.-S. et al. "Delivering the same optical frequency at two places: accurate cancellation of phase noise introduced by an optical fiber or other time-varying path". *Optics Letters* **19**(21), (1994). DOI: 10.1364/OL.19.001777.

[13] Ferrero, V. and Camatel, S. "Optical Phase Locking techniques: an overview and a novel method based on Single Side Sub-Carrier modulation". *Optics Express* **16**(2), (2008). DOI: 10.1364/OE.16.000818.

[14] Wang, F. et al. "Simple, low-cost, and well-performing optical phase-locked loop for frequency and phase locking of semiconductor lasers". *Applied Optics* **62**(27), (2023). DOI: 10.1364/AO.496663.

[15] Bohn, J. L., Rey, A. M., and Ye, J. "Cold molecules: Progress in quantum engineering of chemistry and quantum matter". *Science* **357**(6355), (2017). DOI: 10.1126/science.aam6299.

[16] Augenbraun, B. L. et al. "Molecular Asymmetry and Optical Cycling: Laser Cooling Asymmetric Top Molecules". *Physical Review X* **10**(3), (2020). DOI: 10.1103/PhysRevX.10.031022.

[17] Stevenson, I. et al. "Ultracold Gas of Dipolar NaCs Ground State Molecules". *Physical Review Letters* **130**(11), (2023). DOI: 10.1103/PhysRevLett.130.113002.

[18] Gong, T. et al. "Measurement of the permanent electric dipole moment of ultracold ground state ^{85}Rb^{133}Cs molecules by microwave coherent spectroscopy". *Optics Express* **29**(2), (2021). DOI: 10.1364/OE.411249.

[19] Śmiałkowski, M. and Tomza, M. "Highly polar molecules consisting of a copper or silver atom interacting with an alkali-metal or alkaline-earth-metal atom". *Physical Review A* **103**(2), (2021). DOI: 10.1103/PhysRevA.103.022802.

[20] Chin, C. et al. "Feshbach resonances in ultracold gases". *Reviews of Modern Physics* **82**(2), (2010). DOI: 10.1103/RevModPhys.82.1225.

[21] Ulmanis, J. et al. "Ultracold Molecules Formed by Photoassociation: Heteronuclear Dimers, Inelastic Collisions, and Interactions with Ultrashort Laser Pulses". *Chemical Reviews* **112**(9), (2012). DOI: 10.1021/cr300215h.

[22] Davis, K. B. et al. "Bose-Einstein Condensation in a Gas of Sodium Atoms". *Physical Review Letters* **75**(22), (1995). DOI: 10.1103/PhysRevLett.75.3969.

[23] Anderson, M. H. et al. "Observation of Bose-Einstein Condensation in a Dilute Atomic Vapor". *Science* **269**(5221), (1995). DOI: 10.1126/science.269.5221.198.

[24] Greiner, M. et al. "Quantum phase transition from a superfluid to a Mott insulator in a gas of ultracold atoms". *Nature* **415**(6867), (2002). DOI: 10.1038/415039a.

[25] Diddams, S. A. et al. "An Optical Clock Based on a Single Trapped $^{199}Hg^{+}$ Ion". *Science* **293**(5531), (2001). DOI: 10.1126/science.1061171.

[26] Takamoto, M. et al. "An optical lattice clock". *Nature* **435**(7040), (2005). DOI: 10.1038/nature03541.

[27] Schmidt-Kaler, F. et al. "Realization of the Cirac–Zoller controlled-NOT quantum gate". *Nature* **422**(6930), (2003). DOI: 10.1038/nature01494.

[28] Leibfried, D. et al. "Experimental demonstration of a robust, high-fidelity geometric two ion-qubit phase gate". *Nature* **422**(6930), (2003). DOI: 10.1038/nature01492.

[29] Hänsch, T. W. and Schawlow, A. L. "Cooling of gases by laser radiation". *Optics Communications* **13**(1), (1975). DOI: 10.1016/0030-4018(75)90159-5.

[30] Chu, S. et al. "Three-dimensional viscous confinement and cooling of atoms by resonance radiation pressure". *Physical Review Letters* **55**(1), (1985). DOI: 10.1103/PhysRevLett.55.48.

[31] Chu, S. "Nobel Lecture: The manipulation of neutral particles". *Reviews of Modern Physics* **70**(3), (1998). DOI: 10.1103/RevModPhys.70.685.

[32] Mandl, F. *Statistical Physics*. Wiley, 1988.

[33] Lett, P. D. et al. "Optical molasses". *JOSA B* **6**(11), (1989). DOI: 10.1364/JOSAB.6.002084.

[34] Foot, C. J. *Atomic Physics*. Oxford University Press, 2005.

[35] Stenholm, S. "The semiclassical theory of laser cooling". *Reviews of Modern Physics* **58**(3), (1986). DOI: 10.1103/RevModPhys.58.699.

[36] Cooper, C. J. et al. "The Temperature of Atoms in a Magneto-optical Trap". *Europhysics Letters* **28**(6), (1994). DOI: 10.1209/0295-5075/28/6/004.

[37] Chang, R. et al. "Three-dimensional laser cooling at the Doppler limit". *Physical Review A* **90**(6), (2014). DOI: 10.1103/PhysRevA.90.063407.

[38] Metcalf, H. J. and Straten, P. V. d. *Laser Cooling and Trapping*. Springer Science & Business Media, 1999.

[39] Cohen-Tannoudji, C. N. "Nobel Lecture: Manipulating atoms with photons". *Reviews of Modern Physics* **70**(3), (1998). DOI: 10.1103/RevModPhys.70.707.

[40] Raab, E. L. et al. "Trapping of Neutral Sodium Atoms with Radiation Pressure". *Physical Review Letters* **59**(23), (1987). DOI: 10.1103/PhysRevLett.59.2631.

[41] Gallagher, A. and Pritchard, D. E. "Exoergic collisions of cold Na*-Na". *Physical Review Letters* **63**(9), (1989). DOI: 10.1103/PhysRevLett.63.957.

[42] Monroe, C. et al. "Very cold trapped atoms in a vapor cell". *Physical Review Letters* **65**(13), (1990). DOI: 10.1103/PhysRevLett.65.1571.

[43] Bagnato, V. S. et al. "Measuring the capture velocity of atoms in a magneto-optical trap as a function of laser intensity". *Physical Review A* **62**(1), (2000). DOI: 10.1103/PhysRevA.62.013404.

[44] Fuso, F. et al. "Ion processes in the photoionization of laser cooled alkali atoms". *Optics Communications* **173**(1), (2000). DOI: 10.1016/S0030-4018(99)00609-4.

[45] Lindquist, K., Stephens, M., and Wieman, C. "Experimental and theoretical study of the vapor-cell Zeeman optical trap". *Physical Review A* **46**(7), (1992). DOI: 10.1103/PhysRevA.46.4082.

[46] Haw, M. et al. "Magneto-optical trap loading rate dependence on trap depth and vapor density". *JOSA B* **29**(3), (2012). DOI: 10.1364/JOSAB.29.000475.

[47] Sesko, D. et al. "Collisional losses from a light-force atom trap". *Physical Review Letters* **63**(9), (1989). DOI: 10.1103/PhysRevLett.63.961.

[48] Weiner, J. et al. "Experiments and theory in cold and ultracold collisions". *Reviews of Modern Physics* **71**(1), (1999). DOI: 10.1103/RevModPhys.71.1.

[49] Prentiss, M. et al. "Atomic-density-dependent losses in an optical trap". *Optics Letters* **13**(6), (1988). DOI: 10.1364/OL.13.000452.

[50] Mancini, M. W. et al. "Trap loss rate for heteronuclear cold collisions in two species magneto-optical trap". *The European Physical Journal D - Atomic, Molecular, Optical and Plasma Physics* **30**(1), (2004). DOI: 10.1140/epjd/e2004-00066-6.

[51] Shevy, Y. et al. "Bimodal speed distributions in laser-cooled atoms". *Physical Review Letters* **62**(10), (1989). DOI: 10.1103/PhysRevLett.62.1118.

[52] Salomon, C. et al. "Laser Cooling of Cesium Atoms Below 3 uK". *Europhysics Letters* **12**(8), (1990). DOI: 10.1209/0295-5075/12/8/003.

[53] Gerz, C. et al. "The Temperature of Optical Molasses for Two Different Atomic Angular Momenta". *Europhysics Letters* **21**(6), (1993). DOI: 10.1209/0295-5075/21/6/005.

[54] Landini, M. et al. "Sub-Doppler laser cooling of potassium atoms". *Physical Review A* **84**(4), (2011). DOI: 10.1103/PhysRevA.84.043432.

[55] Bruce, G. D. et al. "Sub-Doppler laser cooling of ^{40}K with Raman gray molasses on the D_2 line". *Journal of Physics B: Atomic, Molecular and Optical Physics* **50**(9), (2017). DOI: 10.1088/1361-6455/aa65ea.

[56] Boiron, D. et al. "Three-dimensional cooling of cesium atoms in four-beam gray optical molasses". *Physical Review A* **52**(5), (1995). DOI: 10.1103/PhysRevA.52.R3425.

[57] Boiron, D. et al. "Laser cooling of cesium atoms in gray optical molasses down to 1.1 μK". *Physical Review A* **53**(6), (1996). DOI: 10.1103/PhysRevA.53.R3734.

[58] Grier, A. T. et al. "Λ-enhanced sub-Doppler cooling of lithium atoms in D_1 gray molasses". *Physical Review A* **87**(6), (2013). DOI: 10.1103/PhysRevA.87.063411.

[59] Salomon, G. et al. "Gray-molasses cooling of ^{39}K to a high phase-space density". *Europhysics Letters* **104**(6), (2014). DOI: 10.1209/0295-5075/104/63002.

[60] Rosi, S. et al. "Λ-enhanced grey molasses on the D2 transition of Rubidium-87 atoms". *Scientific Reports* **8**(1), (2018). DOI: 10.1038/s41598-018-19814-z.

[61] Walhout, M., Sterr, U., and Rolston, S. L. "Magnetic inhibition of polarization-gradient laser cooling in $\sigma_+ - \sigma_-$ optical molasses". *Physical Review A* **54**(3), (1996). DOI: 10.1103/PhysRevA.54.2275.

[62] Walhout, M. et al. "σ_+–σ_- Optical molasses in a longitudinal magnetic field". *JOSA B* **9**(11), (1992). DOI: 10.1364/JOSAB.9.001997.

[63] Hsiao, Y.-F., Lin, Y.-J., and Chen, Y.-C. "Λ-enhanced gray-molasses cooling of cesium atoms on the D_2 line". *Physical Review A* **98**(3), (2018). DOI: 10.1103/PhysRevA.98.033419.

[64] *Magnetic Declination in Warsaw, Poland*. en. URL: https://www.magnetic-declination.com/Poland/Warsaw/2121594.html?utm_source=chatgpt.com (visited on 09/01/2025).

[65] Ashkin, A. "Acceleration and Trapping of Particles by Radiation Pressure". *Physical Review Letters* **24**(4), (1970). DOI: 10.1103/PhysRevLett.24.156.

[66] Ashkin, A. and Dziedzic, J. M. "Optical Levitation of Liquid Drops by Radiation Pressure". *Science* **187**(4181), (1975). DOI: 10.1126/science.187.4181.1073.

[67] Ashkin, A. et al. "Observation of a single-beam gradient force optical trap for dielectric particles". *Optics Letters* **11**(5), (1986). DOI: 10.1364/OL.11.000288.

[68] Ashkin, A. *Nobel Lecture: Optical Tweezers and their Application to Biological Systems*. URL: https://www.nobelprize.org/prizes/physics/2018/ashkin/lecture/ (visited on 09/01/2025).

[69] Chu, S. et al. "Experimental Observation of Optically Trapped Atoms". *Physical Review Letters* **57**(3), (1986). DOI: 10.1103/PhysRevLett.57.314.

[70] Barrett, M. D., Sauer, J. A., and Chapman, M. S. "All-Optical Formation of an Atomic Bose-Einstein Condensate". *Physical Review Letters* **87**(1), (2001). DOI: 10.1103/PhysRevLett.87.010404.

[71] Grimm, R., Weidemüller, M., and Ovchinnikov, Y. B. "Optical Dipole Traps for Neutral Atoms". *Advances In Atomic, Molecular, and Optical Physics* **42**, (2000). DOI: 10.1016/S1049-250X(08)60186-X.

[72] Dobosz, J. "Heterodyne interferometer for fast detection of cold atomic mixtures". en. MSc thesis. University of Warsaw, 2019.

[73] Cohen-Tannoudji, C., Dupont-Roc, J., and Grynberg, G. *Atom-Photon Interactions: Basic Processes and Applications*. Wiley, 1992.

[74] Savard, T. A., O'Hara, K. M., and Thomas, J. E. "Laser-noise-induced heating in far-off resonance optical traps". *Physical Review A* **56**(2), (1997). DOI: 10.1103/PhysRevA.56.R1095.

[75] Gardiner, C. W. et al. "Evaluation of heating effects on atoms trapped in an optical trap". *Physical Review A* **61**(4), (2000). DOI: 10.1103/PhysRevA.61.045801.

[76] Arciszewski, P. "An experimental apparatus for laser cooling of potassium and caesium". MSc thesis. University of Warsaw, 2019.

[77] Arciszewski, P. *WebBasedDataBrowser (WBDB). Internal lab project.* `https://github.com/pwarciszewski/WebBasedDataBrowser`. Accessed: 2025-07-28. 2024.

[78] Bocheński, M., Dobosz, J., and Semczuk, M. "Magnetic trapping of an ultracold ^{39}K-^{40}K mixture with a versatile potassium laser system". *Optics Express* **32**(27), (2024). DOI: `10.1364/OE.529071`.

[79] Dinçer, K. "Observation of 'Missing' Vibrational Levels and Extending Photoassociation Spectra of Excited Ultracold Cesium Dimers". PhD thesis. University of Warsaw, 2024.

[80] Escudero, R. G. "Magnetic Field Control and Laser Frequency Stabilization for Strontium Magneto-Optical Traps". en. MA thesis. Max-Planck-Institut für Quantenoptik, 2016.

[81] Todd, P. C. "Snubber circuits: Theory, design and application". In: *Unitrode-Power Supply Design Seminar*. Vol. 2. 1993.

[82] Nilsson, J. W. and Riedel, S. *Electric Circuits*. Pearson Education, 2014.

[83] Bocheński, M. "Feshbach Spectroscopy of Potassium-Cesium Mixtures". PhD thesis. University of Warsaw, 2025.

[84] Steck, D. A. *Cesium D Line Data*. (revision 2.3.4, 8 August 2025). URL: `http://steck.us/alkalidata`.

[85] Tiecke, T. G. "Feshbach resonances in ultracold mixtures of the fermionic quantum gases ^{6}Li and ^{40}K". PhD thesis. University of Amsterdam, 2009.

[86] Wu, X. et al. "Multiaxis atom interferometry with a single-diode laser and a pyramidal magneto-optical trap". *Optica* **4**(12), (2017). DOI: `10.1364/OPTICA.4.001545`.

[87] Deb, A. B., Rakonjac, A., and Kjærgaard, N. "Versatile laser system for experiments with cold atomic gases". *JOSA B* **29**(11), (2012). DOI: `10.1364/JOSAB.29.003109`.

[88] Valenzuela, V. M. et al. "Multiple isotope magneto-optical trap from a single diode laser". *JOSA B* **30**(5), (2013). DOI: `10.1364/JOSAB.30.001205`.

[89] Kittlaus, E. et al. "Semiconductor optical amplifier-based laser system for cold-atom sensors". *EPJ Quantum Technology* **12**(1), (2025). DOI: `10.1140/epjqt/s40507-025-00348-z`.

[90] Alibert, J. et al. "A millimeter magnetic trap for a dual (^{85}Rb and ^{87}Rb) species atom interferometer". *Review of Scientific Instruments* **88**(11), (2017). DOI: 10.1063/1.4997149.

[91] Banerjee, D. *PLL Performance, Simulation, and Design*. Texas Instruments, 2017.

[92] Gardner, F. M. *Phaselock Techniques*. John Wiley & Sons, 2005.

[93] Gozzini, A. et al. "Light-induced ejection of alkali atoms in polysiloxane coated cells". *Il Nuovo Cimento D* **15**(5), (1993). DOI: 10.1007/BF02482437.

[94] Torralbo-Campo, L. et al. "Light-induced atomic desorption in a compact system for ultracold atoms". *Scientific Reports* **5**(1), (2015). DOI: 10.1038/srep14729.

[95] Hatakeyama, A., Wilde, M., and Fukutani, K. "Classification of Light-Induced Desorption of Alkali Atoms in Glass Cells Used in Atomic Physics Experiments". *e-Journal of Surface Science and Nanotechnology* **4**, (2006). DOI: 10.1380/ejssnt.2006.63.

[96] Dobosz, J., Bocheński, M., and Semczuk, M. "Bidirectional, Analog Current Source Benchmarked with Gray Molasses-Assisted Stray Magnetic Field Compensation". *Applied Sciences* **11**(21), (2021). DOI: 10.3390/app112110474.

[97] Borkowski, M. et al. "Active stabilization of kilogauss magnetic fields to the ppm level for magnetoassociation on ultranarrow Feshbach resonances". *Review of Scientific Instruments* **94**(7), (2023). DOI: 10.1063/5.0143825.

[98] Linzen, S. et al. "Low-noise computer-controlled current source for quantum coherence experiments". *Review of Scientific Instruments* **75**(8), (2004). DOI: 10.1063/1.1771499.

[99] Koivuniemi, J., Luusalo, R., and Hakonen, P. "Bipolar programmable current supply for superconducting nuclear magnetic resonance magnets". *Review of Scientific Instruments* **69**(9), (1998). DOI: 10.1063/1.1149109.

[100] Yang, Y.-M. et al. "Ultra-low noise and high bandwidth bipolar current driver for precise magnetic field control". *Review of Scientific Instruments* **90**(1), (2019). DOI: 10.1063/1.5046484.

[101] Arango, N. and Kuang, I. A. A. Martinos Center for Biomedical Imaging. Accessed: 2025-07-30. URL: https://rflab.martinos.org/index.php/Current_driver:Current_driver.

[102] Franklin, G. F., Powell, D., and Emami-Naeini, A. F. *Feedback Control of Dynamic Systems, Global Edition*. Pearson Education, 2019.

[103] Nath, D. et al. "Quantum-interference-enhanced deep sub-Doppler cooling of ^{39}K atoms in gray molasses". *Physical Review A* **88**(5), (2013). DOI: 10.1103/PhysRevA.88.053407.

[104] Allan, D. "Statistics of atomic frequency standards". *Proceedings of the IEEE* **54**(2), (1966). DOI: 10.1109/PROC.1966.4634.

[105] Riley, W. and Howe, D. A. "Handbook of Frequency Stability Analysis". *NIST*, (2008).

[106] Fortier, T. and Baumann, E. "20 years of developments in optical frequency comb technology and applications". *Communications Physics* **2**(1), (2019). DOI: 10.1038/s42005-019-0249-y.

[107] Telle, H. et al. "Carrier-envelope offset phase control: A novel concept for absolute optical frequency measurement and ultrashort pulse generation". *Applied Physics B* **69**(4), (1999). DOI: 10.1007/s003400050813.

[108] Jones, D. J. et al. "Carrier-Envelope Phase Control of Femtosecond Mode-Locked Lasers and Direct Optical Frequency Synthesis". *Science* **288**(5466), (2000). DOI: 10.1126/science.288.5466.635.

[109] Holzwarth, R. et al. "Optical Frequency Synthesizer for Precision Spectroscopy". *Physical Review Letters* **85**(11), (2000). DOI: 10.1103/PhysRevLett.85.2264.

[110] Diddams, S. A., Vahala, K., and Udem, T. "Optical frequency combs: Coherently uniting the electromagnetic spectrum". *Science* **369**(6501), (2020). DOI: 10.1126/science.aay3676.

[111] Reichert, J. et al. "Measuring the frequency of light with mode-locked lasers". *Optics Communications* **172**(1), (1999). DOI: 10.1016/S0030-4018(99)00491-5.

[112] Udem, T. et al. "Absolute Optical Frequency Measurement of the Cesium D_1 Line with a Mode-Locked Laser". *Physical Review Letters* **82**(18), (1999). DOI: 10.1103/PhysRevLett.82.3568.

[113] Telle, H., Lipphardt, B., and Stenger, J. "Kerr-lens, mode-locked lasers as transfer oscillators for optical frequency measurements". *Applied Physics B* **74**(1), (2002). DOI: 10.1007/s003400100735.

[114] Stenger, J. et al. "Ultraprecise Measurement of Optical Frequency Ratios". *Physical Review Letters* **88**(7), (2002). DOI: 10.1103/PhysRevLett.88.073601.

[115] Foreman, S. M. et al. "Coherent Optical Phase Transfer over a 32-km Fiber with 1 s Instability at 10^{-17}". *Physical Review Letters* **99**(15), (2007). DOI: 10.1103/PhysRevLett.99.153601.

[116] Terra, O. et al. "Phase-coherent comparison of two optical frequency standards over 146 km using a telecommunication fiber link". *Applied Physics B* **97**(3), (2009). DOI: 10.1007/s00340-009-3653-2.

[117] Fujieda, M. et al. "All-optical link for direct comparison of distant optical clocks". *Optics Express* **19**(17), (2011). DOI: 10.1364/OE.19.016498.

[118] Deschênes, J.-D. et al. "Synchronization of Distant Optical Clocks at the Femtosecond Level". *Physical Review X* **6**(2), (2016). DOI: 10.1103/PhysRevX.6.021016.

[119] Stowe, M. C. et al. "Direct frequency comb spectroscopy". *Advances In Atomic, Molecular, and Optical Physics* **55**, (2008). DOI: 10.1016/S1049-250X(07)55001-9.

[120] Coddington, I., Swann, W. C., and Newbury, N. R. "Coherent Multiheterodyne Spectroscopy Using Stabilized Optical Frequency Combs". *Physical Review Letters* **100**(1), (2008). DOI: 10.1103/PhysRevLett.100.013902.

[121] Coddington, I., Newbury, N., and Swann, W. "Dual-comb spectroscopy". *Optica* **3**(4), (2016). DOI: 10.1364/OPTICA.3.000414.

[122] Thorpe, M. and Ye, J. "Cavity-enhanced direct frequency comb spectroscopy". *Applied Physics B* **91**(3), (2008). DOI: 10.1007/s00340-008-3019-1.

[123] Bergeron, H., Deschênes, J.-D., and Genest, J. "Improving the signal-to-noise ratio of the beat note between a frequency comb and a tunable laser using a dynamically tracking optical filter". *Optics Letters* **41**(18), (2016). DOI: 10.1364/OL.41.004253.

[124] Deschênes, J.-D. and Genest, J. "Heterodyne beats between a continuous-wave laser and a frequency comb beyond the shot-noise limit of a single comb mode". *Physical Review A* **87**(2), (2013). DOI: 10.1103/PhysRevA.87.023802.

[125] *Diffraction Gratings Tutorial*. en. URL: https://www.thorlabs.com/newgrouppage9.cfm?objectgroup_id=9026 (visited on 08/26/2025).

[126] Loewen, E. G. and Popov, E. *Diffraction Gratings and Applications*. CRC Press, 2018.

[127] Lopez, O. et al. "Frequency and time transfer for metrology and beyond using telecommunication network fibres". *Comptes Rendus Physique* **16**(5), (2015). DOI: 10.1016/j.crhy.2015.04.005.

[128] Peev, M. et al. "The SECOQC quantum key distribution network in Vienna". *New Journal of Physics* **11**(7), (2009). DOI: 10.1088/1367-2630/11/7/075001.

[129] Mao, Y. et al. "Integrating quantum key distribution with classical communications in backbone fiber network". *Optics Express* **26**(5), (2018). DOI: 10.1364/OE.26.006010.

[130] Morzyński, P. et al. "Absolute measurement of the $^1S_0$ - $^3P_0$ clock transition in neutral ^{88}Sr over the 330 km-long stabilized fibre optic link". *Scientific Reports* **5**(1), (2015). DOI: 10.1038/srep17495.

[131] Guéna, J. et al. "First international comparison of fountain primary frequency standards via a long distance optical fiber link". *Metrologia* **54**(3), (2017). DOI: 10.1088/1681-7575/aa65fe.

[132] Stock, M. et al. "The revision of the SI—the result of three decades of progress in metrology". *Metrologia* **56**(2), (2019). DOI: 10.1088/1681-7575/ab0013.

[133] Bercy, A. et al. "Two-way optical frequency comparisons at 5×10^{-21} relative stability over 100-km telecommunication network fibers". *Physical Review A* **90**(6), (2014). DOI: 10.1103/PhysRevA.90.061802.

[134] Uhlenberg, G., Dirscherl, J., and Walther, H. "Magneto-optical trapping of silver atoms". *Physical Review A* **62**(6), (2000). DOI: 10.1103/PhysRevA.62.063404.

[135] Aoki, T. et al. "Photoionization loss in simultaneous magneto-optical trapping of Rb and Sr". *Physical Review A* **87**(6), (2013). DOI: 10.1103/PhysRevA.87.063426.

[136] Witkowski, M. et al. "Photoionization cross sections of the $5S_{1/2}$ and $5P_{3/2}$ states of Rb in simultaneous magneto-optical trapping of Rb and Hg". *Physical Review A* **98**(5), (2018). DOI: 10.1103/PhysRevA.98.053444.

[137] Vayninger, M. et al. *A magneto-optical trap of silver and potassium atoms.* arXiv:2507.11434 [physics]. July 2025. DOI: 10.48550/arXiv.2507.11434.

[138] Maragò, O. et al. "Photoionization cross sections for excited laser-cooled cesium atoms". *Physical Review A* **57**(6), (1998). DOI: 10.1103/PhysRevA.57.R4110.

[139] Patterson, B. M., Takekoshi, T., and Knize, R. J. "Measurement of the photoionization cross section of the $6P_{3/2}$ state of cesium". *Physical Review A* **59**(3), (1999). DOI: 10.1103/PhysRevA.59.2508.

[140] Kalyar, M. A. et al. "Measurements of photoionization cross section of the 4p levels and oscillator strength of the 4p→nd $^2D_{3/2,5/2}$ transitions of potassium". *Optics & Laser Technology* **77**, (2016). DOI: 10.1016/j.optlastec.2015.09.001.

[141] Amin, N. et al. "Measurements of photoionization cross sections from the 4p, 5d and 7s excited states of potassium". *Journal of Quantitative Spectroscopy and Radiative Transfer* **109**(5), (2008). DOI: 10.1016/j.jqsrt.2007.09.008.

[142] Wippel, V. et al. "Photoionization cross-sections of the first excited states of sodium and lithium in a magneto-optical trap". *The European Physical Journal D - Atomic, Molecular, Optical and Plasma Physics* **17**(3), (2001). DOI: 10.1007/s100530170002.

[143] Carmichael, H. *Statistical Methods in Quantum Optics 1: Master Equations and Fokker-Planck Equations*. Springer Science & Business Media, 1998.

[144] Townsend, C. G. et al. "Phase-space density in the magneto-optical trap". *Physical Review A* **52**(2), (1995). DOI: 10.1103/PhysRevA.52.1423.

[145] Sansonetti, J. E. "Wavelengths, Transition Probabilities, and Energy Levels for the Spectra of Potassium (KI through KXIX)". *Journal of Physical and Chemical Reference Data* **37**(1), (2008). DOI: 10.1063/1.2789451.

[146] Sansonetti, J. E. "Wavelengths, Transition Probabilities, and Energy Levels for the Spectra of Cesium (CsI–CsLV)". *Journal of Physical and Chemical Reference Data* **38**(4), (2009). DOI: 10.1063/1.3132702.

[147] Hansch, T. W. and Couillaud, B. "Laser frequency stabilization by polarization spectroscopy of a reflecting reference cavity". *Optics Communications* **35**(3), (1980). DOI: 10.1016/0030-4018(80)90069-3.

[148] Wiegand, B. et al. "Linien: A versatile, user-friendly, open-source FPGA-based tool for frequency stabilization and spectroscopy parameter optimization". *Review of Scientific Instruments* **93**(6), (2022). DOI: 10.1063/5.0090384.

[149] Weisheit, J. C. "Excited-state cesium photoionization cross sections". *Journal of Quantitative Spectroscopy and Radiative Transfer* **12**(8), (1972). DOI: 10.1016/0022-4073(72)90063-5.

[150] Zatsarinny, O. and Tayal, S. S. "Photoionization of potassium atoms from the ground and excited states". *Physical Review A* **81**(4), (2010). DOI: 10.1103/PhysRevA.81.043423.

[151] Lowell, J. R. et al. "Measurement of the photoionization cross section of the $5S_{1/2}$ state of rubidium". *Physical Review A* **66**(6), (2002). DOI: 10.1103/PhysRevA.66.062704.

[152] Ciampini, D. et al. "Photoionization of ultracold and Bose-Einstein-condensed Rb atoms". *Physical Review A* **66**(4), (2002). DOI: 10.1103/PhysRevA.66.043409.

[153] Kuk, N. "Phase coherent laser systems for experiments with cold atoms". MSc thesis. University of Warsaw, 2021.

[154] Hairer, E., Nørsett, S. P., and Wanner, G. *Solving Ordinary Differential Equations I: Nonstiff Problems*. Springer Science & Business Media, 2008.

[155] Butcher, J. C. *Numerical methods for ordinary differential equations*. Wiley, 2008.

[156] Dormand, J. R. and Prince, P. J. "A family of embedded Runge-Kutta formulae". *Journal of Computational and Applied Mathematics* **6**(1), (1980). DOI: 10.1016/0771-050X(80)90013-3.

[157] Horowitz, P. and Hill, W. *The Art of Electronics*. Cambridge University Press, 2015.